2017

Behavior of thin colloidal films and fundamental studies of convective deposition

Kedar Joshi
Lehigh University

Recommended Citation

Joshi, Kedar, "Behavior of thin colloidal films and fundamental studies of convective deposition" (2017). *Theses and Dissertations*. 2650.
http://preserve.lehigh.edu/etd/2650

Behavior of thin colloidal films and fundamental studies of convective deposition

By

Kedar Joshi

Presented to the Graduate and Research Committee
of Lehigh University
in Candidacy for the Degree of
Doctor of Philosophy

in
Chemical Engineering

Lehigh University

May 2017

CERTIFICATE OF APPROVAL

Approved and recommended for acceptance as a dissertation in partial fulfillment of the requirements for the degree of Doctor of Philosophy.

Date

James F Gilchrist, *Ph.D.*
Associate Professor of
Chemical Engineering, Lehigh University
Dissertation advisor

Accepted date

Committee Members:

James F Gilchrist, *Ph.D.*
Associate Professor of
Chemical Engineering, Lehigh University
Committee Chair

Mark A. Snyder, *Ph.D.*
Associate Professor of
Chemical Engineering, Lehigh University
Committee member

Manoj K. Chaudhury, *Ph.D.*
Franklin J. Howes Jr., Distinguished Professor of
Chemical Engineering, Lehigh University
Committee member

Ilona Kretzschmar, *Ph.D.*
Department Chair, Professor of
Chemical Engineering, The City College of New York
Committee member

ACKNOWLEDGMENTS

Special thanks to my dissertation advisor, Prof. James F. Gilchrist for his support and invaluable comments and suggestions throughout my Ph.D. work. He always made me think on my own, which helped me to become an independent researcher. Also, his regular feedback and freedom of work helped me to push through Ph.D. while keeping my other hobbies alive. He encourages all students in his lab to own their research so that the final product is not just research but a student too. I would like to thank Prof. Manoj Chaudhury for all brief chats we had of good ideas. His research always motivates me, and his colloids class was simply too good. Also, I would like to thank my other committee members, Prof. Mark Snyder and Prof. Ilona Kretzschmar.

I want to thank all past and present members of the Gilchrist lab. Thanks to Alex, Erg, Tharanga and Midhun for teaching me all small details, which helped me to hit the research pedal. The healthy and helpful environment in the lab has been a constant source of companionship and support throughout the years. Thanks to the department of chemical and biomolecular engineering Lehigh, for providing a great platform. In addition, the graduate student population as a whole has made my time at Lehigh fun and productive. I thank you all.

I want to thank all my Lehigh friends for their support and help, they made this ride very smooth and unique. I made some special friends who made this long grind of school possible and gave me some life time memories, I thank you Meenal, Chandresh, Nimish, Sarvesh, and Nishant. Especially to Aditi, besides being a good friend she has been a great source and a sink for ideas. Thank you for all tireless discussions we had.

I want to thank Lehigh Lewis Tennis Center and Lehigh Valley Chess Club which kept me fit and sharp.

And finally, I want to thank my parents and close family members. Nothing could have been possible without their tireless support and motivation. For aiming any target, you need clear background and stress-free mind, which was given to me by my parents in every possible bit.

Regarding specific projects, I want to thank those who made our success possible.

Chapter 2: Drying and cracking in convective deposition

The study of cracking in nanoparticle assembly was started by an ex-member of our lab, Dr. Alex Weldon. He contributed in most of the experimental work and took several SEM and profilometry measurements. Also, I would like to thank Prof. Alex Routh for giving a lot of insights about this phenomenon. This study is very close to his area of expertise and lucky we had the privilege to meet him in one of the conferences. He is one of the pioneers to study cracking in colloids.

Chapter 3: Role of surface energy gradient

The second part of this chapter, in which we studied the effect of binary solvent, I worked with Dr. Tanyakorn Muangnapoh and an undergraduate student Mike Stever.

Chapter 4: Effect of ionic strength and surface charge on convective deposition

I worked with Dr. Tanyakorn Muangnapoh and an undergraduate student Mike Stever on this project. Dr. Muangnapoh helped in carrying out the experiments and analyzing the microstructure. Mike, on the other hand, helped in few experiments and designing a humidity control box, which was very crucial.

Chapter 5: Spacing of spontaneous and seeded streaks

It was a vision of a high school student, Jane Boettcher. Also, thanks to Dr. Midhun joy who wrote the Matlab code, and tireless debugging of the same. Also, thanks to Dr. Muangnapoh for his contribution in the experimental part.

Chapter 6: Correlation of particle crystallinity in ALB deposition

I worked with a master student working in our lab, Zhiquao Zeng. Also, big thank to Dr. Xue Li, since this project is an extension of her work. Thanks to Dr. Eric Daniel for helping in building ALB apparatus. Also, I'm grateful to 'Versuflex' for providing initial funding for this research.

My research was funded by the NSF grant, CBET: Particle and Multiphase Processes Scalable Nano-manufacturing Program. I'm grateful for this support.

Dedicated to my late grandfathers

Madhukar Joshi

Govind Bhide

TABLE OF CONTENTS

LIST OF FIGURES

ABSTRACT

Colloidal assembly is emerging in different avenues of modern technology like photonics, membrane, quantum dots, and molecular adsorption devices. Fabricating network of colloidal particle is governed by the surface energy and fluid flows. As you go smaller in size, fundamental understanding of the process is crucial. Previous research in our group was focused on the different applications of using the particle networks. Fabricating these structures on a desired substrate, with a choice of particles, and a desirable number of layers is a tedious task. It demands the thorough understanding of process parameters and different interactions in the thin colloidal film.

In the following work, we have separated the convective deposition into two parts. One is governed by thin film stability of solvent, particle interactions with substrate and interface, and interfacial properties, on the other hand, the second part is governed by the solvent flow through a porous structure of particles network. Separating one process into two bits helps in probing for more details.

Previous models of convective deposition capture the essential physics over narrow ranges of parameters, however, there is much room for developing robust models over broader deposition conditions and understanding instabilities in this system. In the convective deposition, the suspension flow is driven by solvent evaporation. The widely used Nagayama equation for the convective deposition defines the evaporation loss as the product of the evaporation rate (J_e) and drying length (ℓ). Here, ℓ is the hydrodynamic length scale, which for many years' have been assumed as a constant. Even though it is safe to assume a constant value for ℓ in a small region of substrate velocity, it fails to predict the coating thickness over wide velocity range. Following the work done by Y. Jung et al. we have derived an analytical expression for

the drying length in the convective deposition for a more general geometry, treating a system as a Darcy flow. This analysis allows the prediction of coating thickness over a wider range of substrate velocities.

In depositing a thicker or smaller particles colloidal crystals, the evaporation driven hydrodynamic stress in the thin film causes crack formation. In such cases, the crack spacing varies with the thickness. This phenomenon is not new and has been observed in all length scales. It has been shown that, in a colloidal crystal, a crack spacing scales up with a hydrodynamic stress. Interestingly, the simultaneous 1D drying and particle deposition in convective deposition results in highly linear uniform cracks. We have shown that the crack spacing can be easily tuned with the deposition speed or the substrate temperature. These fundamental studies enable optimizing deposition conditions to produce various thin film structures for a given particle size, solvent, and stabilizing agent.

As is done in many previous studies of convective deposition and evaporating droplets, an addition of a surfactant can significantly change the mode of deposition to be nearly independent of the evaporation rate and deposition velocity by altering this length scale and thin film flow. At lower surfactant concentrations, the added surfactant had no effects on the assembly. At higher surfactant concentrations above the critical micelle concentration, the marangoni stresses become the main driving force for the flow inside the thin film. This Marangoni flow which can be much stronger than that driven by the evaporation may be tailored to produce the desired particle depositions over a wide range of velocities. The direction of marangoni flow is important. We have studied the mixture of water-ethanol as a choice of solvent, which allows completely reverse results that of the excess surfactant concentration.

We also have studied the particle-particle and particle-substrate interactions, which play a crucial role in the convective deposition. Following results demonstrates the non-trivial effects of varying surface charge and ionic strength of monosized silica microspheres in the water on the quality of the deposited monolayer. The increase in particle surface charge results in a broader range of parameters that result in monolayer deposition which can be explained considering the particle-substrate electrostatic repulsion in solution. Resulting changes in the coating morphology and microstructure at different solution conditions were observed using confocal microscopy enabling correlation of order to disorder transitions with relative particle stability.

The following work discusses the novel way of isolating the inherent streaking instabilities happening in the convective deposition. With hydrophobic treating substrate in periodic areas allows one to separate these instabilities, leaving an ideal coating in between. The final part of this thesis is devoted to a relatively new scale-up technique of continuous particle assembly. We have studied the limitations on microstructure at higher substrate velocities as well as a smaller improvement in microstructure using a bidisperse silica suspension.

CHAPTER 1

Introduction

1.1. Summary

A significant part of this work is done to gain a fundamental understanding of one of the particle assembly methods known as convective deposition. This work includes extending the theoretical background of convective assembly and probing through different parameters. In addition, the following work discusses fabricating nano scale channels using periodic defects in particle assembly and potential scale-up method for obtaining particle assembly over a large area.

Any particle assembly process is governed by flow profile of suspension and particle-substrate interactions. Following projects focus on these two things. Both macroscopic and microscopic properties are observed using different imaging techniques. The analytical hypothesis is justified using confocal and SEM images of microstructure and vice versa. This has been a general strategy for solving the problem.

We have been using the convective deposition in our lab as a tool for different applications, e.g. solar cells, membrane production, cell capture devices, etc. Over several years we have understood the importance of quality and we have been fabricating exceptional quality of crystal structure. However, unawareness of several fundamental problems results in trial and error, which slows down the research. This motivated me to dig deep in some of the fundamental properties of different processes related to the convective deposition and study the effect of the various parameters, which significantly alter the final structure of the colloidal crystal.

1.2. Motivation

Self-assembly is a process of spontaneously forming ordered structures. Self-assembly can be either a static or a dynamic. Self-assembly happens in nature at all the scales, starting with atomic and molecular scale (1A^{o}-10A^{o}) to a macro scale (>1mm) as shown in figure 1.1a, 1.1c. This work interest's scale somewhere in between 10nm -1000nm, this is the typical regime of colloidal particles self-assembly (figure 1.1b).

There are numerous benefits of fabricating uniform assembly of smaller and smaller particles. The size of particles plays a major role in the application you pursue. Consider particles with 100-1000nm diameter, this size is of the order of the wavelength of visible light and also correlates with the size of macromolecules such as proteins, cells, etc. Uniform crystal structures of such particles are very useful in photonics[1–6], LED's[2,7–16], lithography[4,17], ceramics[17], Dye-sensitized solar cell[18–20], cell capture devices[21,22]. As you decrease the diameter of microspheres, the size gets comparable to bacteria, virus and eventually molecules. This process is thus important in fabricating membranes,[16,23–26] biocompatible surfaces[9,27]. Most recent applications of particle assembly include manufacturing Janus particles[28–30], making helix and rings of nanoparticles[31]. Another importance of colloidal particles appears in microrheology of soft matter. Suspensions show shear thinning and thickening behavior under application of stress. Many consumer products need consistency and texture which is delicately balanced by the presence of colloidal particles.

In all these applications the device performance is highly sensitive to the quality of the structure. As you go smaller in size, particle assembly is highly complicated and sensitive to various process parameters. Controlling such complicated process gets tough on a large scale. This is the reason there are many processes utilized for obtaining such structures, and each one has its pros and cons. Some of the particle assembly processes include spin coating[32,33], dip coating[23,34] are fast but less effective, others like gravity settling[35,36] are slow but produce high crystal structure, or some could be more dynamic in nature like an assembly using electric/magnetic forces[4,37–39]. This work digs into evaporative convection, and capillary forces drove particle assembly, known as convective deposition. It requires simple setup, but it is very effective in producing a high order crystal structures in a relatively shorter time. Sometimes it has also been referred as the blade coating technique. It has been introduced almost two decades ago and has been used quite successfully in different applications as mentioned above.

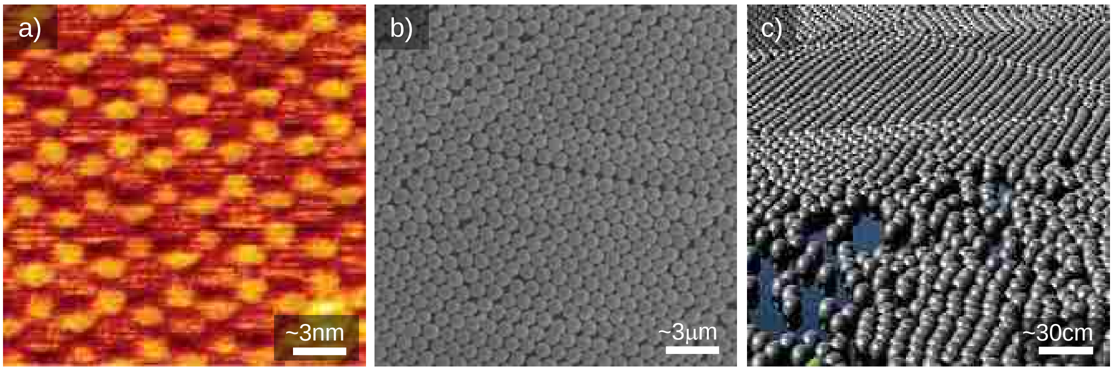

Figure 1.1 a) STM constant current topography of TMA molecules[40], b) close-packed structure of 1μm silica particles obtained using convective deposition, c) rubber balls forming close-packed structures in Ivanhoe Lake.

1.3. Theoretical background

Convective deposition as mentioned above is one of the simplest and intuitive techniques for making colloidal assembly[41,42]. Two common physical processes are simultaneously tuned to each other with a relative motion of the substrate. These processes are the "coffee ring effect" [43,44] and the "Cheerio effect"[45].

Coffee ring effect is a result of (metastable state) pinning of the contact line. When a coffee drop spills, it leaves behind a thick ring of particles as it dries. This happens, because in the presence of coffee particles evaporating contact line pins and more and more liquid flow towards the edge for compensating an evaporation loss. Figure 1.2 gives the time evolution of spilled coffee drop.

On the other hand, particles at liquid interface interacts with each other through deformed interface[46,47]. This phenomenon is known as the "Cheerio effect." Classic examples would be the bubbles moving towards a deformed interface at an edge or cheerios attracting each other in a milk bowl[45].

The immersion capillary attraction force between two colloidal particles at a distance, L, is given by the following equation[47].

$$F \approx \gamma a^2 k_1(qL) \tag{1}$$

'γ' is interfacial tension, 'a' is the particle radius, 'k_1' is a modified Bessel function of the first kind.

Here, 'q' is defined as $\left(q^2 = \frac{\Delta\rho g}{\gamma} - \frac{\Pi'}{\gamma} \right)$. $\Pi' = \left.\frac{\partial \Pi}{\partial h}\right|_{interface}$ Π is disjoining pressure.

For micron size particles this force is dominant over approximately 10μm distance. Since most of the experiments are done using 1μm particles, it is better to have a notion of capillary forces and its range. Figure 1.3 is a schematic representation of deformed interface by immersed particles.

Figure 1.4a shows the general set up for convective deposition, here substrate is moved relative to the blade. The meniscus of suspension is confined between the wedge of a blade and a substrate. Due to their relative motion, the meniscus gets stretched into a thin film and particles align into a close-packed structure as shown in figure 1.4b.

The “Coffee ring” effect is the part where suspension flow is governed by evaporation happening in the thin film. Because of the presence of colloidal particles, the contact line pins, and more and more suspension pushed towards the thin film. The “Cheerio” effect follows and helps making the crystal structure. Particles in thin film deform the interface and to minimize the energy they attract each other. This results in the formation of close-packed structures.

The flow inside a thin film is entirely governed by the evaporation, and thus an average substrate velocity is much lower in the case of convective deposition. For water like solvent, a typical velocity range can be between 0µm/s-250µm/s. If we increase the substrate velocity, we enter into the Landau-Levich type of coating, which is discussed in details in Appendix C.

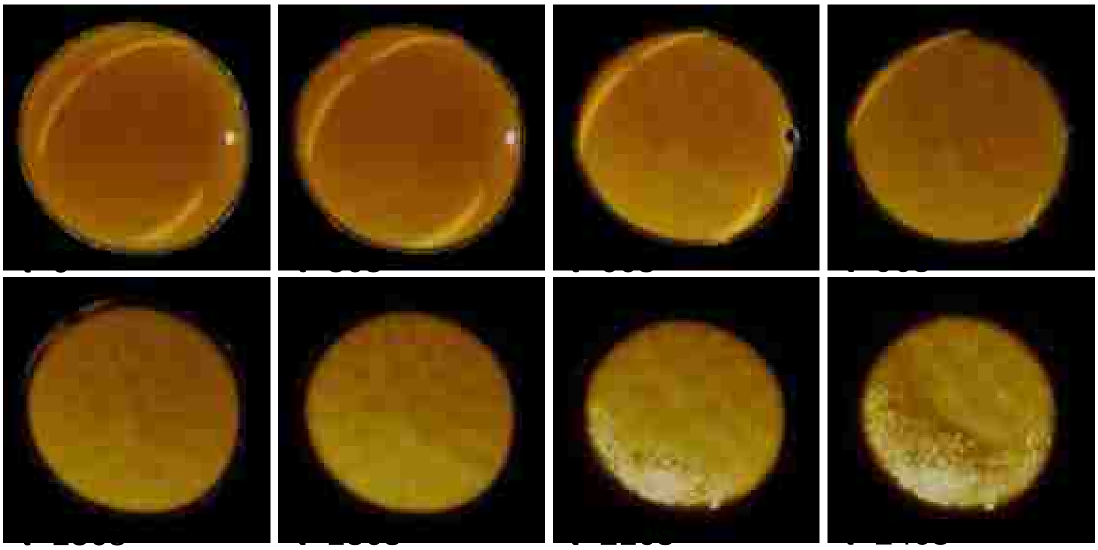

Figure 1.2 time lapse images of evaporating coffee drop, it slowly forms thick ring instead of uniform deposition known as “coffee ring effect.”

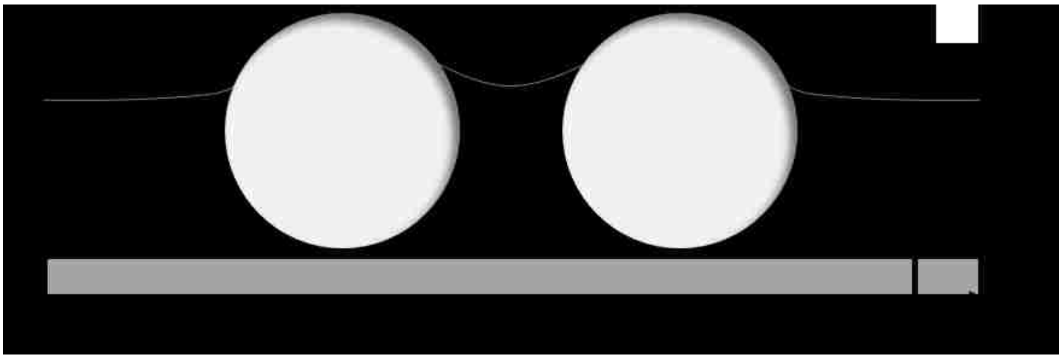

Figure 1.3 Schematic of deformed liquid interface by two immersed colloidal particles.

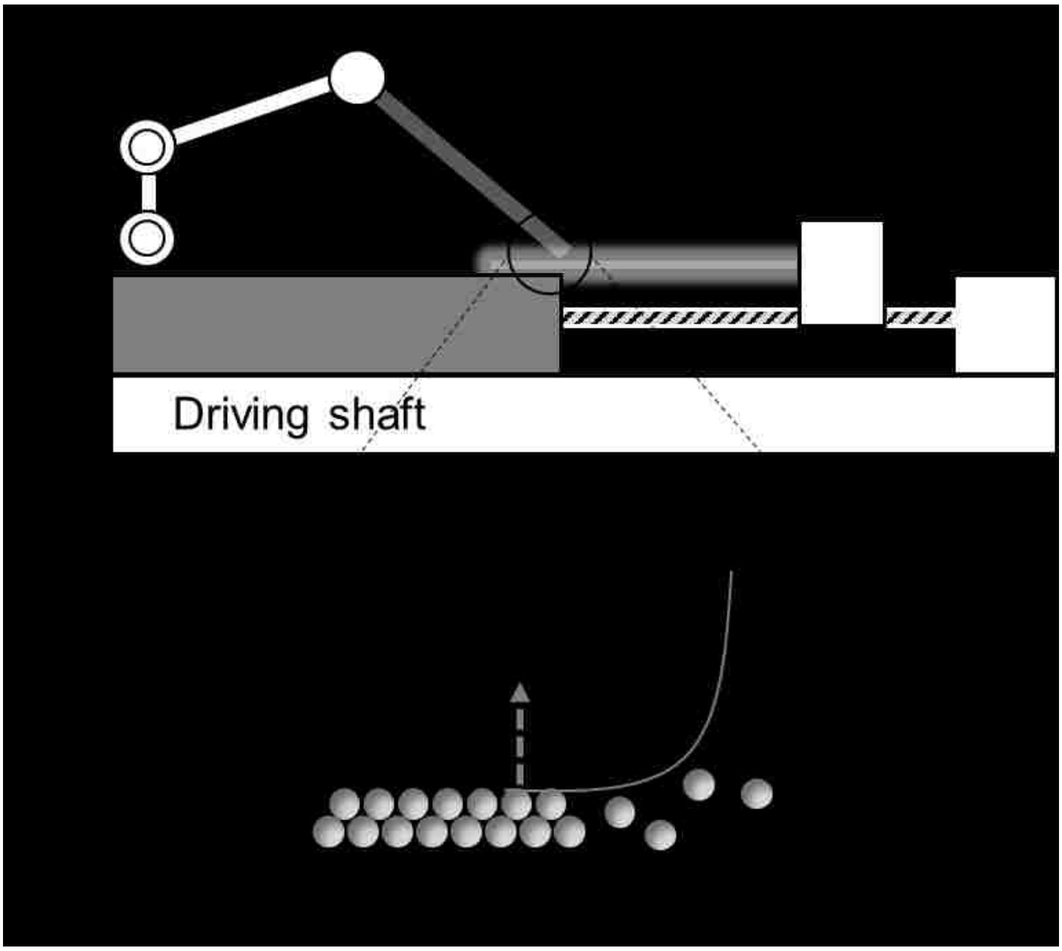

Figure 1.4 a) setup for convective deposition, where linear motor is pushing substrate relative to the blade, b) meniscus is getting stretched into a thin film where particles are forming close-packed structure by capillary attraction. The solvent is evaporating through the particle structure.

1.4. Other fundamental parameters

Besides “Coffee ring” and “Cheerio effect” there are many other things which contribute in physics of the process. Evan though the crude features of the assembly can be explained by these two effects, other parameters such as particle’s nature, solvent properties and substrate interactions with particles as well as solvent play an important role in the quality of colloidal assembly. These parameters govern time for assembly, internal stresses inside thin film, which results in different microstructure[48]. With the correct understanding of every parameter, we can improve microstructure a bit more.

Nagayama in 1995[41,42] through simple mass balance gave an analytical equation to correlate coating thickness to substrate velocity and evaporation rate.

$$u_s = \frac{\beta J_e \ell \phi}{0.603 d N (1-\phi)} \tag{2}$$

Here, u_s is crystallization velocity (m/s), J_e is evaporative rate (m/s), ϕ is volume fraction of particles, d is diameter of particles, and N is number of layers in deposition. The only two parameters which are not very well posed are β and ℓ, where β is interaction parameter, it is more like a fitting parameter which attributes for flux mismatch because of all interactions. On the other hand ℓ is evaporation length, which comes from the hydrodynamics of process. We have studied these parameters in great details (chapter 2, chapter 3, and chapter 4). The goal of each chapter from now on is to reduce this assumption of equation 2 and study the system in more detail.

1.5. Overview of thesis

Most of the work, I have discussed is how we can probe missing content in Eq. (2). Nagayama equation gives a great intuition of this system, but all the complexity is stored in β and ℓ. Unpacking these two things will give great insight about any evaporatively driven particle assembly. In chapter 2, I will be discussing a model which we have developed to analytically express ℓ. This will help in the accurate prediction of a number of layers as a function of substrate velocity. In addition, we will see, in the case of nanoparticle coatings similar physics generates cracks in the final colloidal crystal. This opens another avenue for fabricating MEM's, microchannel devices. The flow in the thin film can be tailored or disturbed using marangoni flow. Marangoni flow is a result of surface tension gradient. Chapter 3, is about manipulating thin film profile using surfactants, binary solvent or temperature. It opens a wide range of assembly patterns since the flow behavior is very sensitive. In chapter 4, I have discussed the effect of interactions on assembly. We have systematically developed the way of representing β for particular set of interactions. In addition, we have correlated the effect of such interactions on the microstructure.

Some of the instabilities can't be avoided in case of convective deposition (chapter 5), but we have developed a novel technique to isolate such instabilities using substrate treatment. The convective assembly can be made continuous, which was previously shown. We have studied the limitations of scale up. In addition, we have shown how the bidisperse suspension could help in improving the final microstructure of assembly.

In appendix C, I will be discussing some future ideas about how the thin film evolves in the case of convective deposition and how unique is it. Why particles form close-packed structures by a high crystallinity, which we wouldn’t have produced by any other method. Also, external energy source can alter the dynamics of particles assembly as in the case of convective deposition.

References

(1) Im, S. H.; Lim, Y. T.; Suh, D. J.; Park, O. O. Three-Dimensional Self-Assembly of Colloids at a Water-Air Interface: A Novel Technique for the Fabrication of Photonic Bandgap Crystals. *Adv. Mater.* **2002**, *14* (19), 1367–1369.

(2) Kumnorkaew, P.; Ee, Y. K.; Tansu, N.; Gilchrist, J. F. Investigation of the Deposition of Microsphere Monolayers for Fabrication of Microlens Arrays. *Langmuir* **2008**, *24* (21), 12150–12157.

(3) Tessier, P. M.; Velev, O. D.; Kalambur, a. T.; Lenhoff, a. M.; Rabolt, J. F.; Kaler, E. W. Structured Metallic Films for Optical and Spectroscopic Applications via Colloidal Crystal Templating. *Adv. Mater.* **2001**, *13* (6), 396–400.

(4) Haes, A. J.; Haynes, C. L.; Van Duyne, R. P. Nanosphere Lithography: Self-Assembled Photonic and Magnetic Materials. *MRS Proc.* **2000**, *636*, 1–6.

(5) Vlasov, Y. a; Bo, X. Z.; Sturm, J. C.; Norris, D. J. On-Chip Natural Assembly of Silicon Photonic Bandgap Crystals. *Nature* **2001**, *414* (6861), 289–293.

(6) Johnson, N. P.; Jin, C.; Li, Z. Y.; McLachlan, M. A.; McComb, D. W.; De La Rue, R. M. Optical Properties of Tetragonal Photonic Crystal Synthesized via Template-Assisted Self-Assembly. *J. Appl. Phys.* **2006**, *99* (11).

(7) Biancaniello, P. L.; Crocker, J. C. Line Optical Tweezers Instrument for Measuring Nanoscale Interactions and Kinetics. *Rev. Sci. Instrum.* **2006**, *77* (11), 1–10.

(8) Hayward, R. C.; Saville, D. a; Aksay, I. a. Electrophoretic Assembly of Colloidal Crystals with Optically Tunable Micropatterns. *Nature* **2000**, *404* (6773), 56–59.

(9) Koyama, K.; Yamaguchi, N.; Miyasaka, T. Antibody-Mediated Bacteriorhodopsin Orientation for Molecular Device Architectures. *Science (New York, N.Y.)*, 1994, *265*, 762–765.

(10) Velev, O. D.; Kaler, E. W. In Situ Assembly of Colloidal Particles into

Miniaturized Biosensors. *Langmuir* **1999**, *15* (11), 3693–3698.

(11) Yi, D. K.; Kim, M. J.; Turner, L.; Breuer, K. S.; Kim, D. Y. Colloid Lithography-Induced Polydimethylsiloxane Microstructures and Their Application to Cell Patterning. *Biotechnol. Lett.* **2006**, *28* (3), 169–173.

(12) Self-assembled, I. L. W.; Microlenses, C.; Ee, Y.; Member, S.; Kumnorkaew, P.; Arif, R. a; Tong, H.; Zhao, H.; Gilchrist, J. F.; Tansu, N. Optimization of Light Extraction Efficiency of. **2009**, *15* (4), 1218–1225.

(13) Li, X. H.; Song, R.; Ee, Y. K.; Kumnorkaew, P.; Gilchrist, J. F.; Tansu, N. Light Extraction Efficiency and Radiation Patterns of III-Nitride Light-Emitting Diodes with Colloidal Microlens Arrays with Various Aspect Ratios. *IEEE Photonics J.* **2011**, *3* (3), 489–499.

(14) Li, X. H.; Zhu, P.; Liu, G.; Zhang, J.; Song, R.; Ee, Y. K.; Kumnorkaew, P.; Gilchrist, J. F.; Tansu, N. Light Extraction Efficiency Enhancement of III-Nitride Light-Emitting Diodes by Using 2-D Close-Packed TiO2 Microsphere Arrays. *IEEE/OSA J. Disp. Technol.* **2013**, *9* (5), 324–332.

(15) Ee, Y.-K.; Arif, R. A.; Tansu, N.; Kumnorkaew, P.; Gilchrist, J. F. Enhancement of Light Extraction Efficiency of InGaN Quantum Wells Light Emitting Diodes Using SiO[sub 2]/polystyrene Microlens Arrays. *Appl. Phys. Lett.* **2007**, *91* (22), 221107.

(16) Weldon, A. L.; Kumnorkaew, P.; Wang, B.; Cheng, X.; Gilchrist, J. F. Fabrication of Macroporous Polymeric Membranes through Binary Convective Deposition. *ACS Appl. Mater. Interfaces* **2012**, *4* (9), 4532–4540.

(17) Harris, D. J.; Hu, H.; Conrad, J. C.; Lewis, J. a. Patterning Colloidal Films via Evaporative Lithography. *Phys. Rev. Lett.* **2007**, *98* (14), 1–4.

(18) Guldin, S.; Hüttner, S.; Kolle, M.; Welland, M. E.; Müller-Buschbaum, P.; Friend, R. H.; Steiner, U.; Tétreault, N. Dye-Sensitized Solar Cell Based on a Three-Dimensional Photonic Crystal. *Nano Lett.* **2010**, *10* (7), 2303–2309.

(19) Atwater, H. A.; Polman, A. Plasmonics for Improved Photovoltaic Devices. *Nat.*

Mater. **2010**, *9* (10), 865–865.

(20) Weldon, A. L. Investigations into Convective Deposition from Fundamental and Application-Driven Perspectives Investigations into Convective Deposition from Fundamental and Application-Driven Perspectives by, Lehigh University.

(21) Wang, B.; L. Weldon, A.; Kumnorkaew, P.; Xu, B.; Gilchrist, J. F.; Cheng, X. Effect of Surface Nanotopography on Immunoaffinity Cell Capture in Microfluidic Devices. *Langmuir* **2011**, *27* (17), 11229–11237.

(22) Han, W.; Allio, B. a.; Foster, D. G.; King, M. R. Nanoparticle Coatings for Enhanced Capture of Flowing Cells in Microtubes. *ACS Nano* **2010**, *4* (1), 174–180.

(23) Boudreau, L. C.; Kuck, J. a.; Tsapatsis, M. Deposition of Oriented Zeolite A Films: In Situ and Secondary Growth. *Journal of Membrane Science*, 1999, *152*, 41–59.

(24) Bohaty, A. K.; Abelow, A. E.; Zharov, I. Nanoporous Silica Colloidal Membranes Suspended in Glass. *J. Porous Mater.* **2010**, *18* (3), 297–304.

(25) Yuan, Z.; Burckel, D. B.; Atanassov, P.; Fan, H. Convective Self-Assembly to Deposit Supported Ultra-Thin Mesoporous Silica Films. *J. Mater. Chem.* **2006**, *16* (48), 4637.

(26) Velev, O. D.; Lenhoff, A. M. Colloidal Crystals as Templates for Porous Materials T T. *Synthesis (Stuttg).* **2000**, *5*, 56–63.

(27) Zhang, Y.; Wang, S.; Eghtedari, M.; Motamedi, M.; Kotov, N. a. Inverted-Colloidal-Crystal Hydrogel Matrices as Three-Dimensional Cell Scaffolds. *Adv. Funct. Mater.* **2005**, *15* (5), 725–731.

(28) Pawar, A. B.; Kretzschmar, I. Patchy Particles by Glancing Angle Deposition. *Langmuir* **2008**, *24* (2), 355–358.

(29) Pawar, A. B.; Kretzschmar, I. Fabrication, Assembly, and Application of Patchy Particles. *Macromol. Rapid Commun.* **2010**, *31* (2), 150–168.

(30) Paunov, V. N.; Cayre, O. J. Supraparticles and“Janus” Particles Fabricated by Replication of Particle Monolayers at Liquid Surfaces Using a Gel Trapping Technique. *Adv. Mater.* **2004**, *16* (910), 788–791.

(31) Kim, H. S.; Lee, C. H.; Sudeep, P. K.; Emrick, T.; Crosby, A. J. Nanoparticle Stripes, Grids, and Ribbons Produced by Flow Coating. *Adv. Mater.* **2010**, *22* (41), 4600–4604.

(32) Toolan, D. T. W.; Fujii, S.; Ebbens, S. J.; Nakamura, Y.; Howse, J. R. On the Mechanisms of Colloidal Self-Assembly during Spin-Coating. *Soft Matter* **2014**, *10* (44), 8804–8812.

(33) Wang, D. Y.; Mohwald, H. Rapid Fabrication of Binary Colloidal Crystals by Stepwise Spin-Coating. *Adv. Mater.* **2004**, *16* (3), 244–247.

(34) Mayer, H. C.; Krechetnikov, R. Landau-Levich Flow Visualization: Revealing the Flow Topology Responsible for the Film Thickening Phenomena. *Phys. Fluids* **2012**, *24* (5), 1–33.

(35) Ye, R.; Ye, Y. H.; Zhou, Z.; Xu, H. Gravity-Assisted Convective Assembly of Centimeter-Sized Uniform Two-Dimensional Colloidal Crystals. *Langmuir* **2013**, *29* (6), 1796–1801.

(36) Gilchrist, J. F.; Chan, A. T.; Weeks, E. R.; Lewis, J. a. Phase Behavior and 3D Structure of Strongly Attractive Microsphere-Nanoparticle Mixtures. *Langmuir* **2005**, *21* (24), 11040–11047.

(37) Velev, O. D.; Bhatt, K. H. On-Chip Micromanipulation and Assembly of Colloidal Particles by Electric Fields. *Soft Matter* **2006**, *2* (9), 738.

(38) Kleinert, J.; Kim, S.; Velev, O. D. Electric-Field-Assisted Convective Assembly of Colloidal Crystal Coatings. *Langmuir* **2010**, *26* (12), 10380–10385.

(39) Qian, F.; Pascall, A. J.; Bora, M.; Han, T. Y. J.; Guo, S.; Ly, S. S.; Worsley, M. A.; Kuntz, J. D.; Olson, T. Y. On-Demand and Location Selective Particle Assembly via Electrophoretic Deposition for Fabricating Structures with Particle-to-Particle Precision. *Langmuir* **2015**, *31* (12), 3563–3568.

(40) Griessl, S. J. H.; Lackinger, M.; Jamitzky, F.; Markert, T.; Hietschold, M.; Heckl, W. M. Room-Temperature Scanning Tunneling Microscopy Manipulation of Single C 60 Molecules at the Liquid−Solid Interface: Playing Nanosoccer. *J. Phys. Chem. B* **2004**, *108* (31), 11556–11560.

(41) Dimitrov, A. S.; Nagayama, K. Steady-State Unidirectional Convective Assembling of Fine Particles into Two-Dimensional Arrays. *Chem. Phys. Lett.* **1995**, *243* (5–6), 462–468.

(42) Dimitrov, A. S.; Nagayama, K. Continuous Convective Assembling of Fine Particles into Two-Dimensional Arrays on Solid Surfaces. *Langmuir* **1996**, *12* (5), 1303–1311.

(43) Deegan, R. D.; Bakajin, O.; Dupont, T. F.; Huber, G.; Nagel, S. R.; Witten, T. a. Capillary Flow as the Cause of Ring Stains from Dried Liquid Drops. *Nature* **1997**, *389* (6653), 827–829.

(44) Deegan, R. D.; Bakajin, O.; Dupont, T. F.; Huber, G.; Nagel, S. R.; Witten, T. a. Contact Line Deposits in an Evaporating Drop. *Phys. Rev. E - Stat. Physics, Plasmas, Fluids, Relat. Interdiscip. Top.* **2000**, *62* (1 B), 756–765.

(45) Vella, D.; Mahadevan, L. The “Cheerios Effect.” *Am. J. Phys.* **2005**, *72* (817).

(46) Kralchevsky, P. .; Paunov, V. .; Ivanov, I. .; Nagayama, K. Capillary Meniscus Interaction between Colloidal Particles Attached to a Liquid—fluid Interface. *J. Colloid Interface Sci.* **1992**, *151* (1), 79–94.

(47) Kralchevsky, P. a; Nagayama, K. Capillary Forces between Colloidal Particles. *Langmuir* **1994**, *10* (1), 23–36.

(48) Joy, M.; Muangnapoh, T.; Snyder, M. a; Gilchrist, J. F. Flow-Induced Alignment of (100) Fcc Thin Film Colloidal Crystals. *Soft Matter* **2015**, *11* (36), 7092–7100.

CHAPTER 2

Drying and cracking in convective deposition

2.1. Introduction

The convective deposition has proven to be a reliable technique for getting high quality ordered assemblies of colloidal particles[1–5]. The motion of the substrate causes particles within a suspension to be drawn towards thin film by evaporation driven convection similar to the well-known coffee ring effect[6,7]. (Fig. 2.1a). Particles assemble into close-packed structures as a balance of long range capillary forces and/or flow focusing[1,8,9]. The process is scalable, and the resulting colloidal assemblies can be useful in many areas such as coatings for photonics[10–15], lithography[13,16,17], ceramics[16], sensors[18–22], solar cells[23], membranes[24–28], and cell capture devices[29].

The relation between the number of layers and substrate withdrawal velocity is given by a flux balance[3],

$$h = Nd = \frac{\beta J_e \ell \phi}{u_s \phi_m (1-\phi)} \tag{1}$$

Eq. (1) Assumes pseudo-steady state conditions. The evaporation losses lead to convective flux in a thin film as shown in Fig 1a. Here, h is coating thickness (m), d is diameter of particles (m), N corresponds to number of layers in deposition, u_s is substrate velocity (m/s), J_e is evaporative rate (m/s), ϕ is volume fraction of particles in suspension, ϕ_m is volume fraction of particles in deposited film, β is interaction parameter and ℓ is evaporation length (m). This equation assumes the flux is solely governed by the evaporation rate. The contact line remains pinned during the process which generates flux inside meniscus, for the compensation of evaporation losses. This is similar to coffee ring effect, where because of consolidation coffee particles, water is pulled towards the drying edge[6,7]. Although this equation is simplistic, all complexity of the process is stored inside two parameters which are not well posed, specifically β and ℓ. In the original formulation, β is a simple fitting parameter which has been shown to account for different interactions between particle-substrate and particle-interface that can be altered by changing surface charge and ionic strength of suspension[30]. The detail interpretation of β is given in the following chapters. The drying length, ℓ, has also been treated as a fitting parameter generally assumed to be a constant. Although assuming a constant drying length helps in predicting coating thickness over a small range of substrate velocity, it is physically unrealistic and fails to explain the overall trend of coating thickness over larger substrate velocity range. In this work, we have adopted a Darcy flow model to explain the hydrodynamics and analytically evaluate ℓ. Assuming Darcy flow within the deposited particle layer is highly robust and has been successfully used by many researchers for describing flows within particle bed and coatings[31–34].

Using convective deposition one can get different coating morphologies as a function of substrate velocity. Multilayer morphologies are obtained at lower substrate velocities, monolayer deposition at a particular substrate velocity, which in practice is a narrow range, and finally submonolayer coatings at higher substrate velocities. Submonolayer coatings, where only a fraction of a substrate is covered with particles are critical in understanding the relationship between the coating dynamics and resulting microstructure. Additionally, such fractional coatings have applications in making a randomly biased substrate or percolated networks of particles that could be used in transparent conductive films. The Nagayama equation (Eq. 1) is insufficient to calculate the relationship between velocity and deposited morphology for submonolayer coatings because of the ambiguity in, or lack of, a description of the packing fraction of submonolayer coatings where $0 < N < 1$.

In this work, we explain a model by which we estimate a drying length as a function of substrate velocity. The result is a non-trivial extension of the Nagayama Equation, where we show both theoretically and experimentally the deviation from a fixed drying length, ℓ and a simple inverse relationship between the velocity and effective coating thickness. This will extend the predictive capabilities of this mass balance.

2.2. Model development

Fig. 2.1a illustrates the general setup for convective deposition, where a meniscus of suspension is trapped between a blade and a substrate. Substrate moves linearly dragging the meniscus into a thin film. Fig. 2.1b illustrates, how the thin film evolves in the convective deposition is different from the Landau-Levich type viscous entrainment[35]. Fig. 2.1a shows the formation of a crystal front and a drying front, which is very typical in the evaporatively driven assembly of particles. In the convective deposition, phase separation occurs at the crystal front, where particles start assembling and form ordered structures. Prior to the formation of ordered structure, suspension behaves similarly to a single phase solvent as shown in Fig. 2.1b and Fig. 2.1c. The transition at crystal front occurs over few microns[31], where, for monolayer deposition, the capillary forces dominate and pull particles towards the particle bed. I have discussed in depth about this phase transition in next chapters. In multilayer deposition, the convective steering guides particles into the growing crystal front[36]. As particles become part of a close-packed particle bed, they move with the substrate velocity u_s. On the other hand, a solvent flows through this porous particle bed and has completely evaporated at the drying front as shown in Fig. 2.1b. This length between the crystal and drying fronts is defined as the drying length, ℓ. In a pseudo-equilibrium state, the crystal and the drying fronts stay fixed, and one gets dried 2D-film growing continuously with substrate velocity. This length is generally assumed to be a constant. While taking up a fixed value for ℓ gives a fair estimation of the coating thickness in the small range of substrate velocities, it fails to capture the overall trend extending from submonolayer to multilayer coated morphologies.

In Fig. 2.1b we have defined the average suspension inlet velocity by u_0. This is suspension velocity entering the region of deposited particles. It should be noted that, since the flux is governed by the evaporation rate, u_0 is much larger than u_s, ($u_0 >> u_x$). Subsequent to phase separation at the crystal front, the deposited particles move with substrate velocity, u_s, and the solvent flows inside the porous structure. The solvent velocity inside the porous structure is defined by u_x which is a function of x. By doing a simple flux balance, we can get an estimate of coating thickness.

Determining the particle mass balance is straightforward. Since the 2D structure of the close-packed particle bed is continuously growing with substrate velocity, u_s. The rate of particles accumulation is given by ($u_s h \phi_m$). Where ϕ_m is the particle volume fraction in the close pack structure. For hcp packing ϕ_m~0.74. The rate of particle accumulation can be equated to particle inlet flux, which is given by ($u_0 h \phi_m$). This provides a relationship between suspension withdrawal velocity u_0 and substrate velocity u_s, as given below Eq. (2).

$$u_0 = \frac{u_s \phi_m}{\phi_0} \tag{2}$$

The solvent mass balance is governed by the evaporation rate because of the pinning of the contact line in the presence of colloidal particles. This is similar to the coffee ring effect[7]. The flux due to substrate velocity is negligible as compared to evaporation driven flux. Thus the solvent input can be directly related to the evaporation loss. Here we assume evaporation rate remains uniform over the drying length. Thus we can write,

$$u_0 h (1 - \phi_0) = J_e \ell \tag{3}$$

Substituting u_0 from Eq. (2) in Eq. (3), results in principle balance of the Nagayama equation for convective assembly Eq. (4),

$$h = \frac{J_e \ell \phi_0}{u_s \phi_m (1 - \phi_0)} \tag{4}$$

This equation is similar to Eq. (1) with parameter β missing. For practical purposes, β is included to account for any unequal distribution of suspension that results from the flow or particle-substrate interactions that do not emerge from the flux balance. For simple systems with no significant substrate particle interactions, β can be assumed to be equal to unity[3]. The role of β in charge-stabilized systems has been considered in later discussion[30].

While this equation is used broadly, it is insufficient to deduce the coating thickness over a wide range of conditions away from monolayer coatings. The evaporation rate over ℓ determines the flux, but ℓ must depend on the deposited layer itself. In an extreme condition, if the particle layer had no porosity, e.g. assembled cubic particles, it would be impossible to transport fluid through the particles. In the following derivation, we have made an attempt to deduce this length scale from simple flow profile.

We know that the solvent is flowing through the porous structure over drying length. Such liquid flows through porous structures are successfully studied using Darcy flow law[31,32], which relates pressure gradient as a function of the permeability of porous structure as given below Eq. (5).

$$\frac{\partial p}{\partial x} = -\frac{\mu}{k}(u_x - u_s) \tag{5}$$

Where $\partial p/\partial x$ is the pressure gradient, μ is the liquid viscosity, k is the permeability of porous structure and $(u_x\text{-}u_s)$ is the superficial velocity. Since the substrate itself is moving, we are accounting for superficial velocity instead of liquid velocity.

The porous structure itself is a close-packed arrangement of spheres. Thus we can replace *k* by using Carman Kozeny equation[32] as a function of particle diameter and packing fraction ϕ_m as given below Eq. (6).

$$\frac{\partial p}{\partial x} = -\frac{75\mu\phi_m^{\ 2}}{2a^2(1-\phi_m)^2}(u_x - u_s) \tag{6}$$

We can take advantage of the fact that at x=0 phase separation occurs and at $x=\ell$ the liquid velocity is zero for the boundary conditions for u_x. The velocity at packing front x=0 is given by $u_x(0)$, and it can be related to u_s by simple mass balance,

$$u_x(0)\, h(1-\phi_m) = u_0\, h(1-\phi_0). \tag{7}$$

and boundary conditions,

$$u_x(0) = u_s\left\{\frac{(1-\phi_0)\phi_m}{(1-\phi_m)\phi_0}\right\} \tag{8}$$

$$u_x(\ell) = 0\ . \tag{9}$$

This assumes a sharp transition of the phase separation. In reality, the particle phase flux begins to deviate from the fluid phase roughly when the thin film is less than a few particle diameters thick.

From the continuity equation, at any 'x', the change in liquid velocity is proportional to evaporation rate. Thus, $\partial u_x/\partial x = J_e/h$. Solving this equation with above boundary conditions gives

$$u_x = u_s\left\{\frac{(1-\phi_0)\phi_m}{(1-\phi_m)\phi_0}\right\}\left(1 - {x}/{\ell}\right) \tag{10}$$

We can replace u_x from Eq. (10) in Eq. (6) and integrate. The maximum pressure drop in a close-packed structure[32] is typically estimated as $10\gamma/a$. Where "a" is the radius of particles, which are being deposited and "γ" is the interfacial tension. For the maximum capillary pressure drop, the theoretical limit is $12.9\gamma/a$ considering the smallest possible circle inside the close-packed region. Many researchers round up this value to $10\gamma/a$ instead, although experimentally this value is always shown to be less[37]. Integrating Eq. (6) from 0 to some arbitrary $\overline{\ell}$ where the pressure drop goes to zero

$$\int \partial p = \int_0^{\bar{\ell}} \frac{75\mu\phi_m^{\;2}}{2a^2(1-\phi_m)^2}(u_x - u_s) = \frac{10\gamma}{a} \qquad (11)$$

Solving Eq. (8) we get value of $\bar{\ell}$

$$\bar{\ell} = a\bar{\theta}_1 \, {}^{\gamma}\!\big/_{\mu u_s} \qquad (12)$$

Where

$$\bar{\theta}_1 = {}^{20}\!\big/_{75}\left\{(1-\phi_m)^3\phi_0 / \phi_m^{\;2}\left((\phi_m-\phi_0)+0.5\phi_m(\phi_0-1)\right)\right\} \qquad (13)$$

Here, $\bar{\ell}$ is the length scale where, $\nabla p = 0$ and u_x =u_s. From Eq. (7) we can obtain a relation between ℓ and $\bar{\ell}$ as follows,

$$\ell / \bar{\ell} = (1-\phi_0)\phi_m / ((1-\phi_0)\phi_m - (1-\phi_m)\phi_0) \qquad (14)$$

This ratio is approximately equal to unity for the lower volume fraction of suspension. This ratio diverges as $\phi_0 \rightarrow \phi_m$. By substituting this, we get the drying length.

$$\frac{\ell}{a} = \theta_1 \frac{\gamma}{\mu u_s} = \theta_1 Ca^{-1} \qquad (15)$$

This equation rescales the drying length over particle diameter by the capillary number, Ca = $\mu u_s/\gamma$. This relationship between drying length and substrate velocity makes a prediction of the film thickness over wider velocity range impossible. We can substitute ℓ in Eq. (3) and we get modified Nagayama equation.

$$\frac{h}{a} = \theta_1 \frac{\gamma}{\mu u_s^{\;2}} \frac{J_e\phi_0}{(1-\phi_0)\phi_m} \qquad (16)$$

Or in dimensionless terms, we can write it as

$$\left(\frac{h}{a}\right)\frac{\gamma}{\mu J_e} = \left(\theta_1 \frac{\phi_0}{(1-\phi_0)\phi_m}\right)\frac{\gamma^2}{\mu^2 u_s^{\;2}} \text{ Or, } \left(\frac{h}{a}\right)\tilde{C}a^{-1} = \left(\theta_1 \frac{\phi_0}{(1-\phi_0)\phi_m}\right)Ca^{-2} \qquad (17)$$

Here, $\left(\frac{\gamma}{\mu J_e} = \tilde{C}a^{-1}\right)$ is the inverse of an evaporative-based capillary number.

$$\theta_1 = 20/75\left\{\frac{(1-\phi_m)^3(1-\phi_0)\phi_m\phi_0}{\phi_m{}^2\left((\phi_m-\phi_0)+0.5\phi_m(\phi_0-1)\right)\left((1-\phi_0)\phi_m-(1-\phi_m)\phi_0\right)}\right\} \qquad \text{(I)}$$

Eq. (15) works well in the predicting drying length and thus the coating thickness. The advantage of this is the prediction of coating thickness can be made for a wider range of substrate velocity. At lower substrate velocities we get multilayer coatings, and as we increase the substrate velocity, we get monolayer in small velocity domain. Until monolayer formation, the coating thickness varies with a number of layers ($h=N*d$).

Above the monolayer velocity, we get discontinuous domains of close pack structure not covering the entire substrate area. Such patchy/discontinuous coating is a submonolayer domain. Eq. (16) will not work in the submonolayer domain, since the film thickness *(h)* no longer describes the effective porosity, and the packing fraction (ϕ_m) is somewhat ambiguous. Following derivation gives an idea to determine the drying length as well as the packing fraction as a function of substrate velocity in the submonolayer domain. In submonolayer, ϕ_m is variable as discussed above and not the coating thickness h. from simple mass balance we can modify Eq. (4), but now assuming constant film thickness $h=2a$,

$$\ell = C_1 u_s \phi_m \qquad (18)$$

Where $C_1 = \dfrac{2a(1-\phi_0)}{J_e\phi_0}$.

As we enter into the submonolayer regime, the capillary pressure difference drops with increasing porosity. We know that cube of curvature radius (r) which is $a/10$ in above case can be correlated to void inside packed bed of particles. Thus $r^3 \approx (1-\phi_m)$.

This allows us to write maximum capillary drop equal to $\Delta p \approx \frac{10\gamma}{a}\left(\frac{1-\phi_m}{1-\phi_{m0}}\right)^{-1/3}$, now as a function of ϕ_m. The modified Eq. (9) can be written as

$$\ell = \frac{C_2 f(\phi_m)}{u_s} \tag{19}$$

where $C_2 = {}^{20a\gamma}\!/_{75\mu}$

and $f(\phi_m) = \left\{\left(\frac{(1-\phi_m)^3(1-\phi_0)\phi_m\phi_0}{{\phi_m}^2\left((\phi_m-\phi_0)+0.5\phi_m(\phi_0-1)\right)\left((1-\phi_0)\phi_m-(1-\phi_m)\phi_0\right)}\right)(1-\phi_m)^{-1/3}\right\}$.

This is a complicated function of ϕ_m, but can be fitted with power function $f(\phi_m) \sim 0.002\ {\phi_m}^{-n}$ with much accuracy $(R^2>0.99)$. Where $n \in (11, 12)$

$$\ell \approx \frac{C_2 {\phi_m}^{-n}}{u_s}. \tag{20}$$

From Eq. (11) and Eq. (13) we deduce that in the submonolayer domain the drying length should increase with substrate velocity as

$$\ell \approx {u_s}^{0.8}. \tag{21}$$

This also allows one to calculate the fraction of substrate coverage as a function of substrate velocity. We can write the relationship between ϕ_m and u_s as follows.

$$\phi_m \approx {u_s}^{-0.2} \tag{22}$$

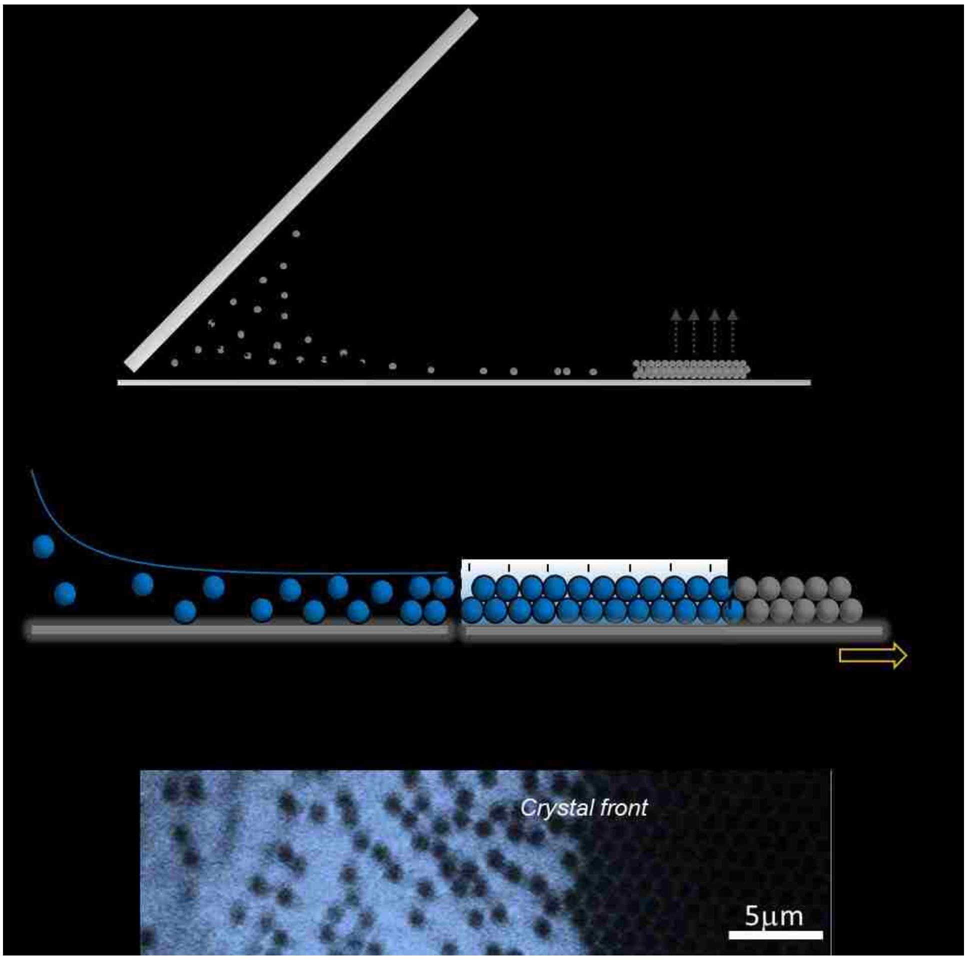

Figure 2.1 (a) illustrates an experimental setup part where a meniscus is pulled relative to the substrate to induce deposition and the local ordering of particles, (b) thin film region where particles are assembling at one end followed by dry particle film, (c) confocal image of crystal front taken while particles assembly.

2.3. Experimental results

2.3.1. Measurement Of Drying Length

To validate these predictions in Eq. (15) and Eq. (21), we experimentally measured the drying length as a function of substrate velocity and compared the results to the model. Fig. 2.2 shows dimensionless length scale (ℓ / a) plotted as a function of capillary number (*Ca*). Results for various blade angles, shown previously to have a small effect on the monolayer speed and length of the thin film region where assembly occurs[11]. From Eq. (15) it is seen that the drying length, ℓ is independent of upstream pressure and therefore meniscus shape. This was demonstrated by varying the blade angle from 18° to 70°, where 90° corresponds to a blade oriented orthogonal to the substrate. The data follows the predicted drying length by Eq. (15) at lower deposition speed, u_s, until monolayer substrate velocity. The magnitude of ℓ predicted is slightly larger than that measured from experiments. This deviation can be accounted by overestimation of the capillary pressure drop. The larger error bars in the multilayer regime are the result of varying thickness across the sample width. On the other hand, the drying length is very uniform across sample width in monolayer and submonolayer domain, resulting in smaller error bars.

Contrary to multi and monolayer, in submonolayer, the drying length gradually increases. These experimental results agree with the prediction of Eq. (21). A linear regression of the power law formula for measured drying length as a function of deposition velocity is $\ell \approx u_s^{0.75}$, which closely matches with Eq. (21). It should be noted, higher substrate velocities resulting in submonolayer deposition is a result of evaporative driven particle assembly. Where internal liquid flux is governed by evaporation rate.

Much higher substrate velocities (on the order of mm/s) would fall under Landau-Levich type coating. Where a film thickness would be determined by viscous entrainment as predicted by the Landau and Levich, a transition demonstrated by Maël Le Berre et al.[35]. This transition occurs approximately at u_s = 500 μm/s, above which, the drying and coating are decoupled. Although, the maximum substrate velocity examined here is 300 μm/s.

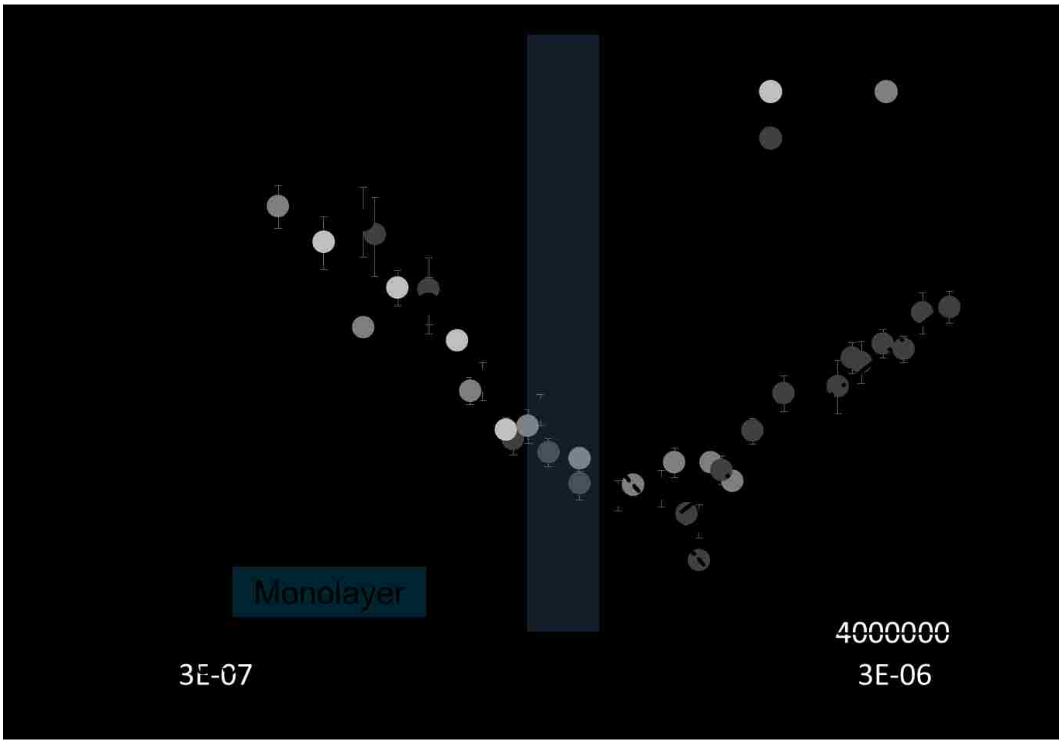

Figure 2.2 Drying length over particle diameter as a function of the capillary number, logarithmic scale. Experiments were performed at different blade angles (25% grayscale) 18°, (50% grayscale) 30°, (75% grayscale) 45°, (100% grayscale) 70°. The dotted black line is from equation (15). The drying length goes through minimum around coating transitions to submonolayer deposition. The double dotted line shows the best fit where ℓ / a scales as $Ca^{0.75}$ similar to equation (21). The shaded region illustrates monolayer deposition[30].[a]

---

[a] Reprinted with permission from [Joshi K. and Gilchrist J. F. "Estimation of drying length during particle assembly by convective deposition" *JCIS*, **2017** 496 222-227] copyright © 2017 Elsevier.

2.3.2. Measurement Of Mean Thickness

Thickness prediction by Eq. (16) was validated with experiments with varying substrate velocities and experimental conditions like relative humidity and temperature. Evaporation rate is scaled with vapor pressure from the Antoine equation for water, $\log(P_V) = A - B/_{C+T}$. The thickness over particle radius and evaporation limited capillary number as a dimensionless number is plotted as a function of the capillary number, predicted by Eq. 16 as $h\gamma/_{a\mu J_e} \approx 1/_{{u_s}^2}\left(\frac{\gamma}{\mu}\right)^2$, or equivalently $h/_a \tilde{C}a^{-1} \approx Ca^{-2}$ (Fig. 2.3). The rough collapse of this data is further validation of Eq. 16. Introducing effects of velocity on drying length allowed the prediction of thickens over the entire range of velocity explored. The n = -1 slope triangle in the graph represents the prediction given by the Nagayama equation where drying length is considered as a constant. A gradient of n = -1 could only fit deposition data over a small range of deposition speeds, inconsistent with the experimental results.

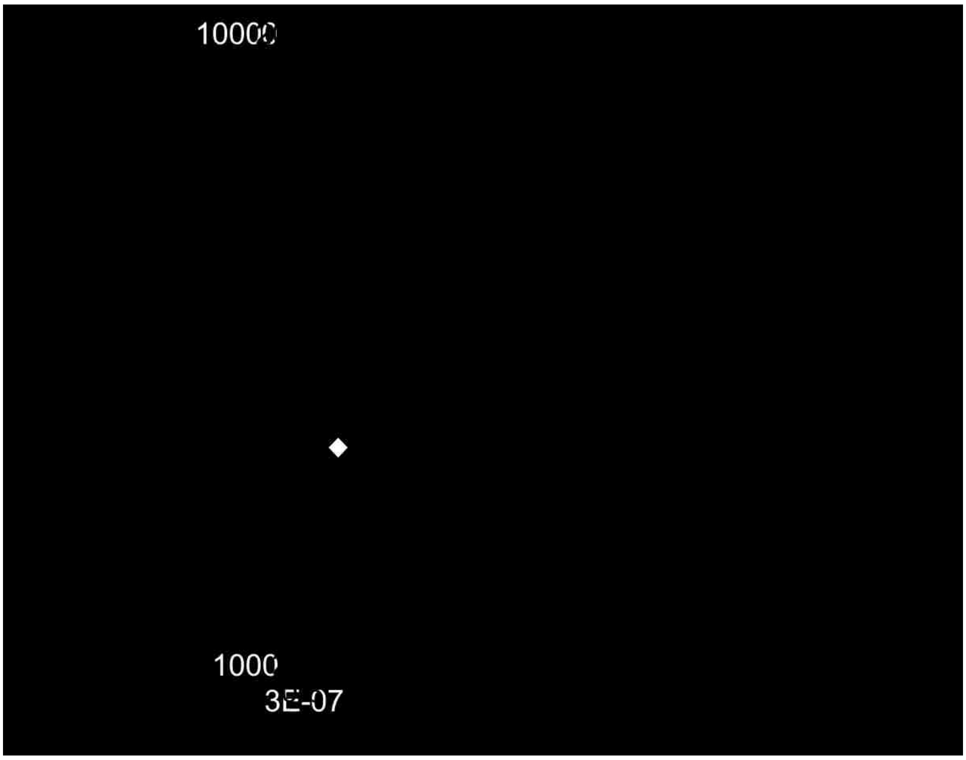

Figure 2.3 Average thickness normalized by particle radius over evaporation-based capillary number as a function of capillary number. Triangles represent RH = 20, and temperature 22°C, diamonds represent RH = 30 and temperature 22°C, plus symbols represent RH = 45 and temperature 22°C, and cross symbols represent suspension at RH = 45 and temperature 40°C. The dotted line represents the predicted *h* from Eq. (16), the slope n = -1 emphasizes the lack of fit to the Nagayama equation when assuming a constant drying length. [b]

---

[b] Reprinted with permission from [Joshi K. and Gilchrist J. F. "Estimation of drying length during particle assembly by convective deposition" *JCIS*, **2017** 496 222-227] copyright © 2017 Elsevier

2.4. Materials and methods

2.4.1. Suspension Preparation

The suspension is made from dispersing silica microspheres in DI water. The silica microspheres (Fuso Chemical Co, Japan) have density 2.2 g/ml and average diameter 1.01±0.02 μm. The suspension is dispersed using a sonic dismembrator (model 550, Fisher Scientific, Pittsburgh, PA) for 10 min and stirred for 30 min (Fisher Sci., model 550).

2.4.2. Substrate Preparation

Plain glass micro slides (76x25x1 mm^3, Fisher PA) are used as the deposition blade, and glass coverslips (40x24x0.25 mm^3, Fisher PA) are used as the substrate for all samples. All glassware is cleaned by immersing in a piranha solution, 80:20 v/v sulfuric acid/hydrogen peroxide, for 30 min. The glassware is then rinsed with DI water until no residual acid remains, and the cleaned glassware is immersed in DI water before use. The back and bottom edges of the glass deposition blade are treated to be hydrophobic by adding a thin coating of parafilm (Fisher PA).

2.4.3. Experimental Conditions

All the experiments were performed in humidity chamber keeping constant relative humidity as specified in experimental conditions. The temperature of substrate kept constant as mentioned in experimental conditions. The experimental setup is shown in Fig. 2.1. The deposition blade was fixed at 45^o or as stated in results and discussion for specific experiments, approximately 50-100μm above the blade. The colloid suspension was injected into the wedge between the substrate and deposition plate, 10 μl volume of suspension was used to draw meniscus in each experiment

2.4.4. Measurement of Drying Length

After images obtained as described in above setup (Fig. 2.4). Characterization was done using ImageJ software. The scale bar was fixed near the substrate which serves as calibration for measurement. The drying length was measured at different points over sample width for multiple samples. At lower substrate velocity a sample is thicker and not uniform across the substrate width, thus having higher variation in drying length. At higher substrate velocity there is uniformness in coating thickness as well as the drying length across the substrate. The length is measured from tip of the meniscus to shining dried coating, since the thin film length before crystal front is very short of the order of tens of micron as confirmed by observing under a confocal microscope, it unlikely adds an error to a measurement.

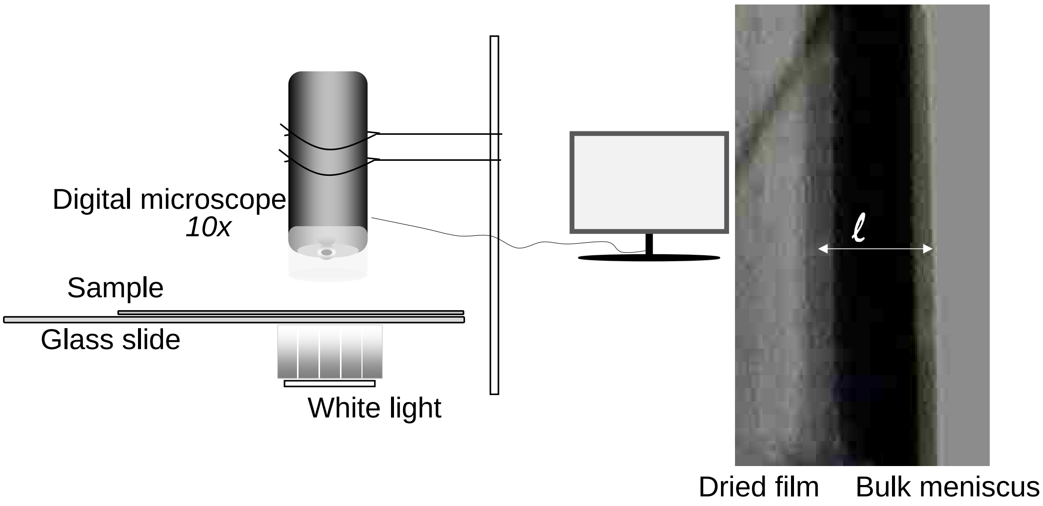

Figure 2.4 White light is shined on a sample while coating which is observed directly by a digital microscope with *10x* magnification. The scale bar was placed near each sample for calibration purpose. Images were obtained by software at different time intervals. Under the white light, bulk meniscus and dried film shine leaving the dark wet film in between.

2.4.5. Measurement of Coating Thickness

Microstructure analysis

Coating morphology such as a multilayer, monolayer, and submonolayer was analyzed using a confocal microscope.

Macrostructure analysis

The overall sample structure is analyzed using the high-resolution scanner. Samples are scanned in dark room with very high resolution, then cropped in interested area. The topology is studied using ImageJ software. The intensities are correlated to thickness using Beer's Law. Intensity power spectra are calibrated to an actual number of layers using confocal microscope and profilometer.

2.4.6. Simplification Of $f(\phi_m)$

$$f(\phi_m) = \left\{ \left(\frac{(1-\phi_m)^3 (1-\phi_0)\phi_m \phi_0}{\phi_m{}^2 \left((\phi_m - \phi_0) + 0.5\phi_m(\phi_0 - 1)\right)\left((1-\phi_0)\phi_m - (1-\phi_m)\phi_0\right)} \right) (1-\phi_m)^{1/3} \right\} \tag{II}$$

This is a complex function of ϕ_m and as discussed earlier we were interested in figuring out how ϕ_m it is related to a substrate velocity. Instead of differentiating this complex function we scale up $f(\phi_m)$ with ϕ_m, by plotting $f(\phi_m)$ with different values of ϕ_m. For both smaller interval and wide intervals of ϕ_m, the power functions fit the data very accurately as shown in the Fig. 2.5 and usually scales as $f(\phi_m) = \phi_m{}^n$ where $n \in (-11,-13)$. This gives the prediction for $\ell \approx u^{{n+1}/{n-1}}$ and $\phi_m \approx u^{{2}/{n-1}}$ using Eq. (12) and Eq. (13). For above values of n; $(n+1)/(n-1)$ ~0.8 and $2/(n-1)$ ~0.2, refer Eq. (14) and Eq. (15). Suspension volume fraction ϕ_0 is taken 0.2 which was used in all experiments.

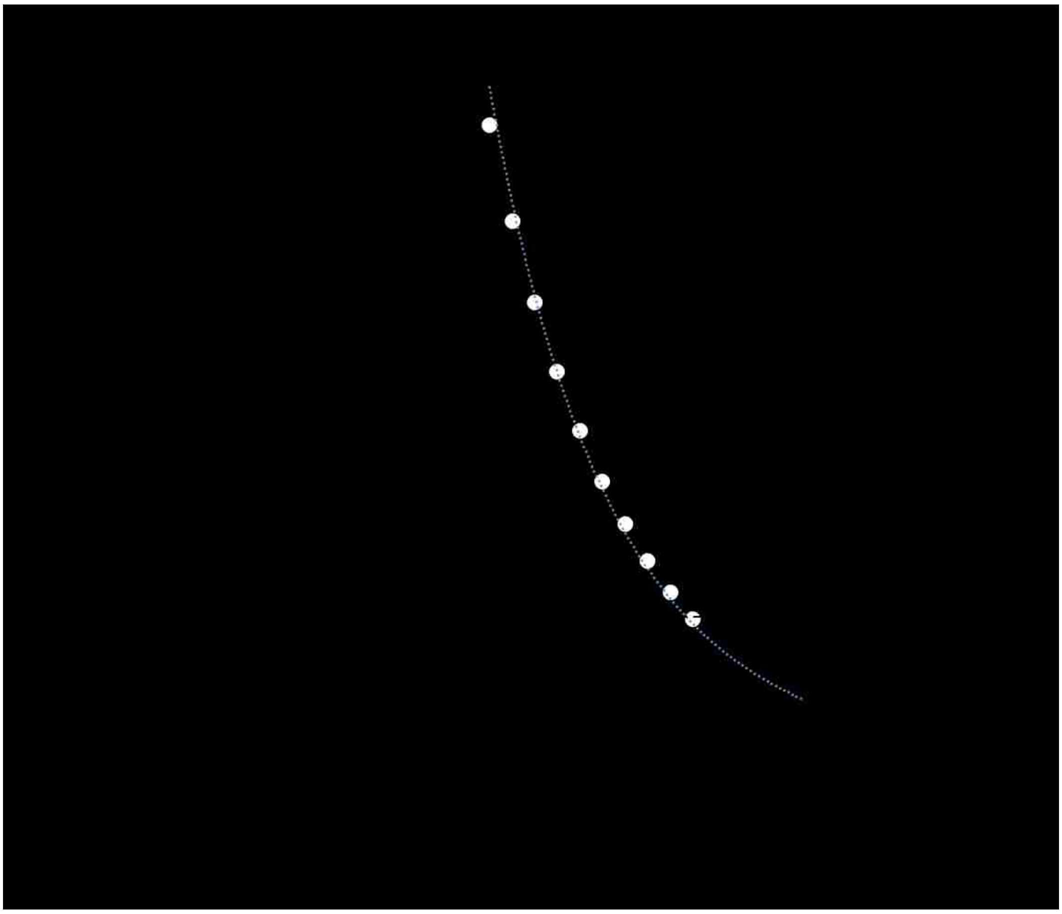

Figure 2.5 $f(\phi_m)$ as a function of ϕ_m. The hollow dots represent values of $f(\phi_m)$ with a larger interval of ϕ_m and the filled dots represent values of $f(\phi_m)$ with a smaller interval of ϕ_m. Both sets of values fit power series as shown in equations with great accuracy.

2.5. Conclusions

We have developed an analytical model which interprets flow through porous particle assembly in a convective deposition. Evaporation rate and pressure drop cease water penetration into porous media. This correlation between flow and drying length helps in predicting coating thickness. This is a very significant improvement than simply assuming a constant drying length as in previous studies. Previous work was geometry specific and insufficient to explain drying length in submonolayer domain[31]. Submonolayer coatings are very useful in understanding the microstructures as well as in making biased region within substrates with many potential applications. The concluded model for submonolayer predicts drying length and degree of submonolayer with high accuracy. Additionally, we have experimentally validated the effective thickness as a function of substrate velocity by using modified Nagayama equation. With the inclusion of certain drying length, one can predict the coating thickness over wider velocity range. This broader view of how deposition is driven by the drying length may prove useful when driving this coating process toward deposition of the minimum amount of material prior to that dominated by viscous entrainment, where the drying conditions determine the microstructure independent of the coating process.

In future work, this analysis can be extrapolated to deposition of nanoparticles (100nm-300nm). With existing knowledge, one can’t explain incapability of the convective deposition to achieve monolayer from such small size particles. Additionally, apart from substrate velocity, solvent physical properties like surface tension and viscosity affect the solvent penetration, which needs experimental validation.

2.6. Introduction to cracking

As we discussed earlier, evaporation is the main driving force for the particle assembly via convective deposition. The predicted drying length equation works well for all size particles and coating thicknesses. Although, as one tries to decrease the particle diameter or consecutively increase the coating thickens, the evaporative stresses start to build up, which after critical point results in a cracking of assembly. This cracking phenomenon is not new, and we see this everywhere in nature. In fact, such cracks are observed at all length scales, e.g. cracks in river deltas, old paints or mountain lines (Fig. 2.6).

Similar cracks have been observed in thick colloidal film[32,38–40]. The physics behind cracking is similar to which we used in drying length derivation. The principal difference is, in drying length, solvent flows and releases its pressure. Though in cracking, due to the high resistance of thickness or smaller particle size, solvent exerts a force on assembly. Crack formation releases stress.

Routh et al., provide extensive modeling and theory to describe crack formation in the drying of nanoparticle suspensions.[32] Solvent evaporation near the drying front leads to a consolidation of particles and increased volume fraction. This will generate a pressure drop and increased fluid flow through the higher-density system. The solvent pressure in the system can be calculated through Darcy's Law and Karman Kozeny equation as shown in Eq. (6).

An expression for velocity which could be expressed in terms of the evaporation rate, J_e, and length to height ratio, L/h, of the dried film[41]. Is given by Eq. (23).

$$u = \left(\gamma \big/ 3\eta J_e \right)^{1/4} J_e \tag{23}$$

Substituting Eq. (23) in Eq. (6) and equating it to the pressure drop allows the derivation of an expression for the relaxation length scale X for flow away from a crack face.

$$X \approx \frac{20a(1-\phi_m)^2}{75\mu\phi_m{}^2}\left(\frac{3\eta\gamma^3}{J_e{}^3}\right)^{1/4} \tag{24}$$

Replacing this length scale with a capillary length will yield a characteristic pressure, which, scaled by capillary pressure drop, yields a dimensionless pressure term which can characterize fluid flow through the higher volume fraction consolidated particle array.

$$p_{cap} = \frac{20a(1-\phi_m)^2}{75\mu\phi_m{}^2 h}\left(\frac{3\gamma\eta}{J_e}\right)^{1/2} \tag{25}$$

Under moderate capillary pressures, the fluid can flow as needed through the thin film of compacted particle. However, as the capillary pressure reaches its maximum, replacement fluid can no longer flow to compensate for that lost due to evaporation. It is this hydrodynamic length scale, the capillary pressure-driven distance the fluid must flow to compensate for that lost to evaporation that controls the onset and evolution of cracking. In particular, capillary forces put the particle thin film under tension. As these stresses grow with increasing evaporation, the system seeks to minimize its capillary forces and its energy. Upon the formation of "cracks," fluid recedes into the particle thin film, and the system energy relaxes.

The supposition that cracks spacing scales with thin film thickness, and resulting increased drying stresses, has been validated experimentally. Routh et al., (**2004)** use Vernier calipers to measure the macroscale crack spacing and film thickness in latex and silica systems.[32] Crack spacing in these systems spans 0.1 to 10 mm, and film thickness spans 10 to 1000 µm. Cracks form with a highly monodisperse spacing as a result of the characteristic hydrodynamic distance that fluid must flow upon the onset of cracks. These data suggest a scaling of crack spacing with film thickness over a pair of particle chemistries and a range of particle sizes. Routh et al. scale crack spacing, y, by X,[32] and find that they scale with $p_{cap}^{-0.8}$. They expect the trend to be linear and attribute an imperfect fit to an overestimate of the maximum capillary pressure.

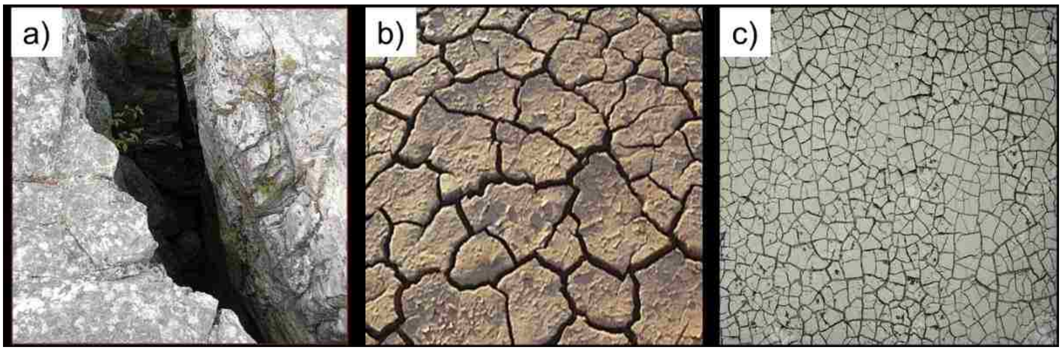

Figure 2.6 evaporation driven cracks found in nature[1*] a) mountain-lines (crack spacing ~10-100m), b) river deltas (crack spacing ~1-10m), and c) old paints (crack spacing ~0.01-0.1m).

2.7. Results and discussion

2.7.1. Thickness vs crack spacing

We have reproduced similar phenomenon in much smaller length scale. In a convective deposition, the assembly progress is linked with evaporation. This allows linear and uniform crack formation at micron length scale. Fig. 2.7 shows the relationship between coating thickness and crack spacing obtained using convective deposition and compared it with old data. Previous data do not address small scale cracking and thinner particle coatings as a result of experimental limitations.[34] Interference profilometry, in correlation with high-resolution optical microscopy, is used to expand established film thickness to crack spacing relations over small length scales. These techniques provide micron to submicron-level detail. The coating thickness was measured by using bare glass slide as a reference point in interference profilometry. Samples were scratched by the fine blade to remove particles near particular measurement area to access the reference height. The film thickness is varied by changing substrate velocity between 32 μm/s to 64 μm/s.

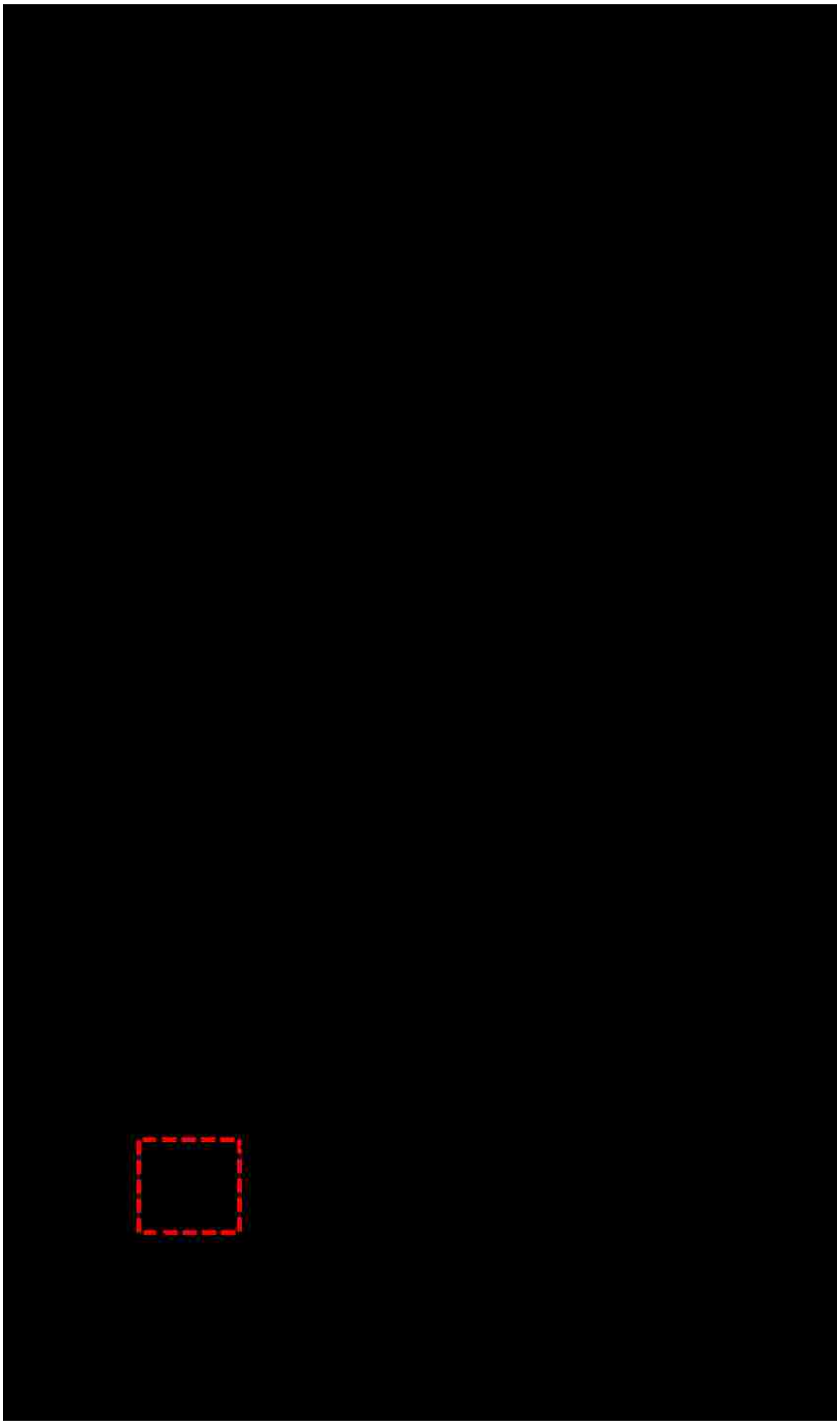

Figure 2.7 a) Crack spacing vs. film thickness obtained at much smaller film thickness, b) comparing the data at lower coating thickness(dark circles) with A. Routh existing data at a much larger thickness (open triangles). The red dotted square in 2b is representing the same data from 2a.[c]

---

[c] Reprinted with permission from [Weldon A., Joshi K., Routh A., and Gilchrist J. F. “Uniform spaced nanoscale cracks in nanoparticle films deposited by convective deposition” *JCIS*, **2017** 487 80-87] copyright © 2017 Elsevier.

Also, note that a minimum crack spacing of ~2 µm is presented in Fig. 2.7. That is the minimum observed spacing where cracks show significant length and monodisperse spacing. Below that length scale, the analysis becomes increasingly complex as samples are characterized by small-scale sub cranks. It is important to note that these thinnest films, and the disappearance of cracking, are on the order of 15-25 particle layers thick. On these length scales, particle-particle interactions and capillary forces become increasingly significant versus large scale thin film evaporative hydrodynamics.

2.7.2. Hydrodynamic scaling of crack spacing

Paralleling the work of Routh et al., 2004, the correlation of crack spacing with thickness can be further examined with the addition of hydrodynamic scaling.[34] Crack spacing, y, normalized by the horizontal hydrodynamic scaling, X, Eq. (24), is plotted with P_{cap} Eq. (25).

Routh et al., 2004 found their data collapsed along the trend:

$$\frac{y}{X} = 0.07 p_{cap}{}^{-0.8} \tag{26}$$

Fig. 2.8 presents the trend of Routh et al., 2004 alongside the hydrodynamically scaled data in this study. The data do not quite match with $0.07.P_{cap}{}^{-0.8}$, this can be attributed to different characteristic velocity in a convective deposition. Since the substrate is moving with as the porous media with u_s, the characteristic fluid velocity depends not only on evaporation rate J_e but also u_s.

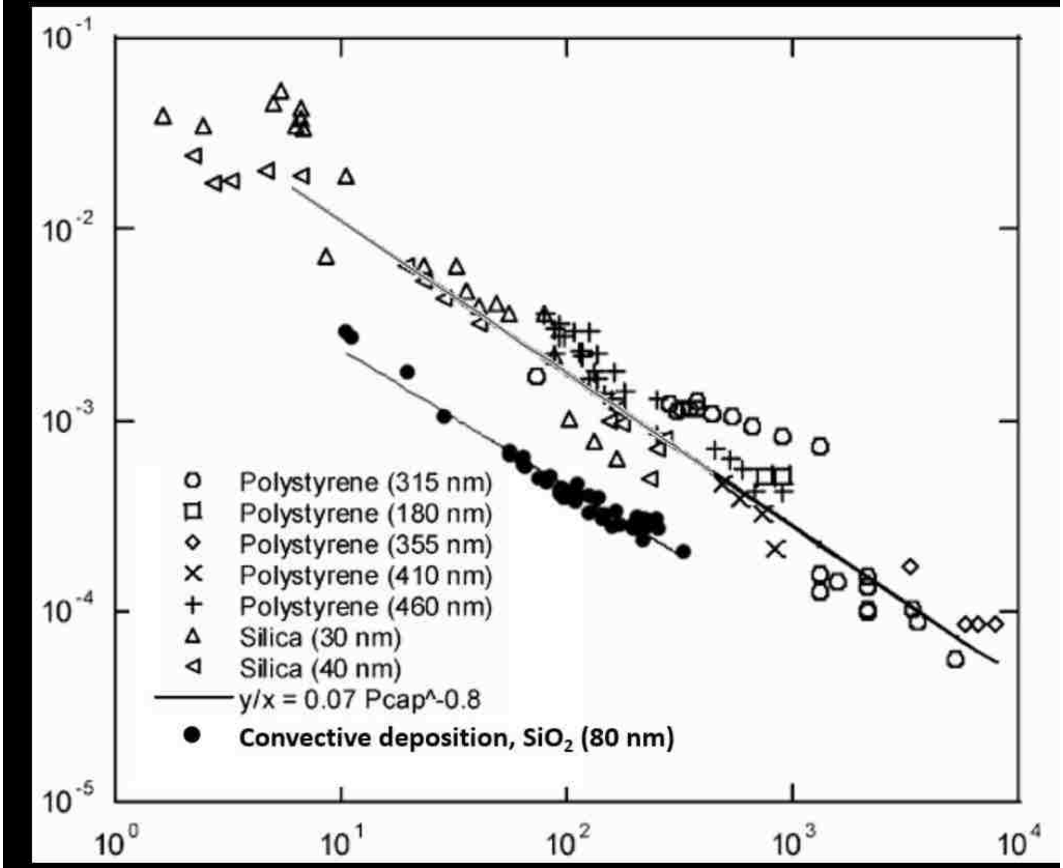

Figure 2.8 Crack spacing, *y*, hydrodynamically scaled by *X*, versus capillary pressure. Routh et al., 2004 data is shown in top trend, as $y/X = 0.07P_{cap}^{-0.8}$. Lower data and trend show this study's data, under smaller scale, cracked thin films the data best fit to $y/X = 0.008P_{cap}^{-0.72}$.[d]

---

[d] Reprinted with permission from [Weldon A., Joshi K., Routh A., and Gilchrist J. F. "Uniform spaced nanoscale cracks in nanoparticle films deposited by convective deposition" *JCIS*, **2017** 487 80-87] copyright © 2017 Elsevier.

Fig. 2.7 and Fig. 2.8 give two important observations. First one is, for uniform cracking to happen, we need a film thickness over a critical value. This thickness corresponds to the critical number of layers. Below that number of layers the water can rise to the surface and no permanent cracks could produce. For 80nm SiO_2 particles, this critical later ~3.

And second is, y/X deviates enough from predicted P_{cap} inverse relationship to catch attention. This might be due to over estimation of capillary pressure. Also in a case of nanoparticles the Darcy flow needs to be modified to account for the Debye length interactions between particles.

2.7.3. Patterning on PDMS

These cracks can serve as a template for fabricating the microchannels. The cracks are stable and allow flow of viscous material through. Also, the adhesion with PDMS can be controlled by selecting the proper surface group on particle. We have performed some preliminary experiments for encouraging the engineering side of this work. The PDMS is allowed to cure inside cracks at 80^o for 2 hours, then peeled off. The structure is completely reprinted on a PDMS stamp. The stiffness of PDMS can be controlled by the weight percentage of cross linking polymer. This is crucial for obtaining the desired aspect ratio of features. The PDMS was obtained from Dow chemical Co. Sylgard® 184 elastomer kit. Fig. 2.9 shows the general procedure (Fig. 2.9a) and scattering pattern (Fig. 2.9b) obtained from PDMS stamp (Fig. 2.9c).

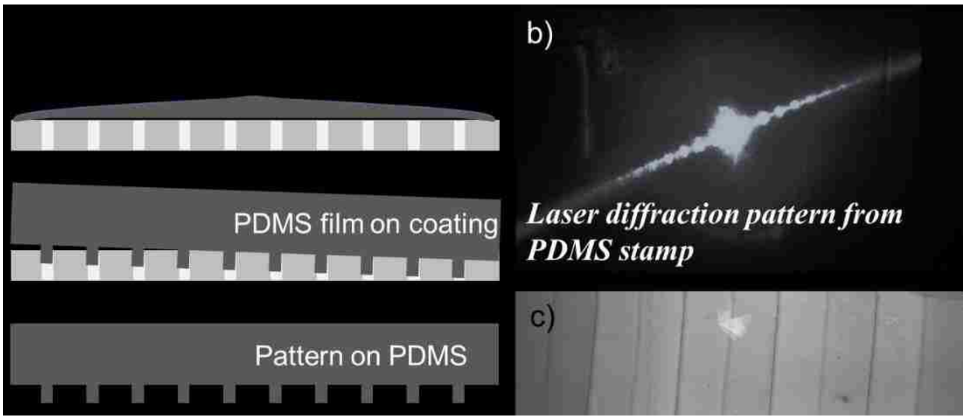

Figure 2.9 a) The PDMS pattern obtained by curing the PDMS elastomer on a cracking sample at 80^{o} for 2hours and then slowly peeling the cured elastic PDMS. b) Scattering pattern obtained by shining (630-680nm) a laser onto the PDMS stamp. The laser spot area is ~ 15mm2, which corresponds to 0.2 billion particle. This shows the consistency of microstructure. c) The actual confocal image of PDMS stamp. The stamp is rewetted using the rhodamine B dye in 8mM DMSO solution for a better imaging.

2.8. Materials and methods

2.8.1. Suspension Preparation

The primary colloid suspension used in this work is prepared by dispersing SiO_2 and Polystyrene (PS) nanoparticles, of comparable size, in deionized (DI) water with a volume fraction ϕ_{nano}. The suspension is dispersed using a sonic dismembrator (model 550, Fisher Scientific, Pittsburgh, PA) for 10 min and then vortexed prior to coating. (Fisher Scientific, model 550). 80 nm SiO_2 nanoparticles are prepared through Stöber synthesis, paralleling the experimental techniques previously described.[24] 75 nm PS nanoparticles are prepared by emulsion polymerization and supplied by the Emulsion Polymers Institute.

2.8.2. Substrate Preparation

Same as section 2.4. (2)

2.8.3. Convective Deposition of Particle Suspensions

Under convective deposition, particles flow to the leading edge of the meniscus via evaporative forces and are drawn to the three-phase contact line near the thin film region. As particles flow into this thin film region, they are deposited and can form highly-crystalline structures through capillary interactions. Convective deposition experiments are carried out as shown previously[42]. A suspension meniscus is pinned atop a glass substrate, by a hydrophobically-coated deposition blade. A linear motor is used to translate the substrate and draw out a thin film. The volume of colloid suspension for each experiment is 10 µL. As an enhancement, some experiments are performed atop a Fisher Scientific isotemp stirring hot plate. Note that surface temperatures noted are hot plate set points. This increases film thickness by increasing evaporation flux.

2.8.4. Microstructural Analysis

Deposited monolayers are observed directly using scanning electron microscopy (SEM) and confocal laser scanning microscopy. A Hitachi 4300 field emission SEM is used to observe particle array microstructure. Prior to SEM imaging, the sample is coated with iridium by vapor deposition. Optical and confocal microscopy is performed using an Olympus IX71 optical microscope paired with a Visitech VTEye confocal system, in conjunction with a 100x objective. Confocal laser scanning microscopy (VTeye, Visitech International) is used to observe the microstructure after rewetting the layer with an aqueous solution of 8 mM Rhodamine B for imaging; this rewetting does not alter the microstructure. Profilometry is carried out using a Zygo Zemetrics ZeGAGE Interference Profilometer, with a 10x objective. Image analysis of optical and electron microscope imagery, as well as interference profilometer, data were carried out using ImageJ.

As shown in Fig. 2.1, convective deposition is used to induce the formation of cracks with highly monodisperse spacing. Cracks spacing is tuned by changing the coating thickness. The suspension from bulk meniscus is dragged towards the drying thin film (figure1a). Particles then assemble themselves at the packing front and liquid flows through this porous media to compensate for the evaporative loss. Compressive stresses developed due to capillary forces result in the formation of cracks. Note how uniform cracks spacing can be obtained over large scales compared with irregular drying in a Petri dish.

A trio of methodologies is used to control nanoparticle thin film thickness, with increased thickness yielding larger crack spacing. Coating thickness is first tuned via suspension volume fraction, with higher volume fractions generating thicker films. Likewise, the evaporative flux can be increased by heating the substrate, increasing coating thickness. Finally, deposition speed, the speed at which the suspension is dragged across the substrate, will tune sample thickness. In these batch experiments, a single volume fraction and thermal gradient are applied to each sample. Thus thin films of homogeneous thickness are deposited. Contrastingly, deposition speed can be varied throughout a batch coating to systematically vary thin film thickness. Increasing nanoparticle thin film thickness, via slower deposition speeds, applied thermal gradients, or increased volume fraction will limit sample transparency. There is a small variation in cracks spacing. Thus the measurement is done by averaging over ten cracks. The standard deviation is small but must be taken into account while fabricating devices.

2.9. Conclusions and future directions

This work concerns deposited nanoparticle thin films and the ability to tune the formation of longitudinal cracking with highly uniform spacing that could be used in microfluidics or MEMS. Increased coating thickness correlates with the onset and increased spacing between micro- to macroscale cracks. The advantage of convective deposition is crack spacing can be easily tuned by changing the substrate velocity or evaporation rate[e]. Next steps include complementary in-situ experiments to quantify crack formation mechanisms and timescales. This will complement the work of Routh et al.[33,39], who by changing the timescales of evaporation and re-wetting latex films, cyclically control the formation and suppression of individual and aggregate cracks. They demonstrate enormous plasticity in crack formation and evolution. Parallel experiments could be performed via in-situ confocal and optical microscopy, as well as interference profilometry.

---

[e] We also have performed experiments by changing substrate temperature to vary the crack spacing. The crack spacing (y) shows quite a linear trend as a function of evaporation rate (J_e). Experiments have been performed with the different size and type of particles. The changes in evaporation rate changes the slope of y vs h graph[43], which implies the hydrodynamic scaling. Rather than a universal slope, which happens as a result of elastocapillary phenomenon[44].

References

(1) Cong, H.; Cao, W. Colloidal Crystallization Induced by Capillary Force. *Langmuir* **2003**, *19* (20), 8177–8181.

(2) Denkov, N.; Velev, O.; Kralchevski, P.; Ivanov, I.; Yoshimura, H.; Nagayama, K. Mechanism of Formation of Two-Dimensional Crystals from Latex Particles on Substrates. *Langmuir* **1992**, *8* (12), 3183–3190.

(3) Dimitrov, A. S.; Nagayama, K. Steady-State Unidirectional Convective Assembling of Fine Particles into Two-Dimensional Arrays. *Chem. Phys. Lett.* **1995**, *243* (5–6), 462–468.

(4) Dimitrov, A. S.; Nagayama, K. Continuous Convective Assembling of Fine Particles into Two-Dimensional Arrays on Solid Surfaces. *Langmuir* **1996**, *12* (5), 1303–1311.

(5) Nagayama, K. Two-Dimensional Self-Assembly of Colloids in Thin Liquid Films. *Colloids Surfaces A Physicochem. Eng. Asp.* **1996**, *109*, 363–374.

(6) Deegan, R. D.; Bakajin, O.; Dupont, T. F.; Huber, G.; Nagel, S. R.; Witten, T. a. Capillary Flow as the Cause of Ring Stains from Dried Liquid Drops. *Nature* **1997**, *389* (6653), 827–829.

(7) Deegan, R. D.; Bakajin, O.; Dupont, T. F.; Huber, G.; Nagel, S. R.; Witten, T. a. Contact Line Deposits in an Evaporating Drop. *Phys. Rev. E - Stat. Physics, Plasmas, Fluids, Relat. Interdiscip. Top.* **2000**, *62* (1 B), 756–765.

(8) Vella, D.; Mahadevan, L. The “Cheerios Effect.” *Am. J. Phys.* **2005**, *72* (817).

(9) Kralchevsky, P. a; Nagayama, K. Capillary Forces between Colloidal Particles. *Langmuir* **1994**, *10* (1), 23–36.

(10) Im, S. H.; Lim, Y. T.; Suh, D. J.; Park, O. O. Three-Dimensional Self-Assembly of Colloids at a Water-Air Interface: A Novel Technique for the Fabrication of Photonic Bandgap Crystals. *Adv. Mater.* **2002**, *14* (19), 1367–1369.

(11) Kumnorkaew, P.; Ee, Y. K.; Tansu, N.; Gilchrist, J. F. Investigation of the

Deposition of Microsphere Monolayers for Fabrication of Microlens Arrays. *Langmuir* **2008**, *24* (21), 12150–12157.

(12) Tessier, P. M.; Velev, O. D.; Kalambur, a. T.; Lenhoff, a. M.; Rabolt, J. F.; Kaler, E. W. Structured Metallic Films for Optical and Spectroscopic Applications via Colloidal Crystal Templating. *Adv. Mater.* **2001**, *13* (6), 396–400.

(13) Haes, A. J.; Haynes, C. L.; Van Duyne, R. P. Nanosphere Lithography: Self-Assembled Photonic and Magnetic Materials. *MRS Proc.* **2000**, *636*, 1–6.

(14) Vlasov, Y. a; Bo, X. Z.; Sturm, J. C.; Norris, D. J. On-Chip Natural Assembly of Silicon Photonic Bandgap Crystals. *Nature* **2001**, *414* (6861), 289–293.

(15) Johnson, N. P.; Jin, C.; Li, Z. Y.; McLachlan, M. A.; McComb, D. W.; De La Rue, R. M. Optical Properties of Tetragonal Photonic Crystal Synthesized via Template-Assisted Self-Assembly. *J. Appl. Phys.* **2006**, *99* (11).

(16) Harris, D. J.; Hu, H.; Conrad, J. C.; Lewis, J. a. Patterning Colloidal Films via Evaporative Lithography. *Phys. Rev. Lett.* **2007**, *98* (14), 1–4.

(17) Haynes, C. L.; McFarland, A. D.; Zhao, L.; Van Duyne, R. P.; Schatz, G. C.; Gunnarsson, L.; Prikulis, J.; Kasemo, B.; Käll, M. Nanoparticle Optics: The Importance of Radiative Dipole Coupling in Two-Dimensional Nanoparticle Arrays [†]. *J. Phys. Chem. B* **2003**, *107* (30), 7337–7342.

(18) Biancaniello, P. L.; Crocker, J. C. Line Optical Tweezers Instrument for Measuring Nanoscale Interactions and Kinetics. *Rev. Sci. Instrum.* **2006**, *77* (11), 1–10.

(19) Hayward, R. C.; Saville, D. a; Aksay, I. a. Electrophoretic Assembly of Colloidal Crystals with Optically Tunable Micropatterns. *Nature* **2000**, *404* (6773), 56–59.

(20) Koyama, K.; Yamaguchi, N.; Miyasaka, T. Antibody-Mediated Bacteriorhodopsin Orientation for Molecular Device Architectures. *Science (New York, N.Y.)*, 1994, *265*, 762–765.

(21) Velev, O. D.; Kaler, E. W. In Situ Assembly of Colloidal Particles into Miniaturized Biosensors. *Langmuir* **1999**, *15* (11), 3693–3698.

(22) Yi, D. K.; Kim, M. J.; Turner, L.; Breuer, K. S.; Kim, D. Y. Colloid Lithography-Induced Polydimethylsiloxane Microstructures and Their Application to Cell Patterning. *Biotechnol. Lett.* **2006**, *28* (3), 169–173.

(23) Guldin, S.; Hüttner, S.; Kolle, M.; Welland, M. E.; Müller-Buschbaum, P.; Friend, R. H.; Steiner, U.; Tétreault, N. Dye-Sensitized Solar Cell Based on a Three-Dimensional Photonic Crystal. *Nano Lett.* **2010**, *10* (7), 2303–2309.

(24) Weldon, A. L.; Kumnorkaew, P.; Wang, B.; Cheng, X.; Gilchrist, J. F. Fabrication of Macroporous Polymeric Membranes through Binary Convective Deposition. *ACS Appl. Mater. Interfaces* **2012**, *4* (9), 4532–4540.

(25) Boudreau, L. C.; Kuck, J. a.; Tsapatsis, M. Deposition of Oriented Zeolite A Films: In Situ and Secondary Growth. *Journal of Membrane Science*, 1999, *152*, 41–59.

(26) Bohaty, A. K.; Abelow, A. E.; Zharov, I. Nanoporous Silica Colloidal Membranes Suspended in Glass. *J. Porous Mater.* **2010**, *18* (3), 297–304.

(27) Yuan, Z.; Burckel, D. B.; Atanassov, P.; Fan, H. Convective Self-Assembly to Deposit Supported Ultra-Thin Mesoporous Silica Films. *J. Mater. Chem.* **2006**, *16* (48), 4637.

(28) Velev, O. D.; Lenhoff, A. M. Colloidal Crystals as Templates for Porous Materials T T. *Synthesis (Stuttg).* **2000**, *5*, 56–63.

(29) Wang, B.; L. Weldon, A.; Kumnorkaew, P.; Xu, B.; Gilchrist, J. F.; Cheng, X. Effect of Surface Nanotopography on Immunoaffinity Cell Capture in Microfluidic Devices. *Langmuir* **2011**, *27* (17), 11229–11237.

(30) Joshi, K.; Muangnapoh, T.; Stever, M. D.; Gilchrist, J. F. Effect of Ionic Strength and Surface Charge on Convective Deposition. *Langmuir* **2015**, *31* (45), 12348–12353.

(31) Jung, Y. D.; Ahn, K. H. Prediction of Coating Thickness in the Convective Assembly Process. *Langmuir* **2013**, *29* (51), 15762–15769.

(32) Lee, W. P.; Routh, A. F. Why Do Drying Films Crack? *Langmuir* **2004**, *20* (23), 9885–9888.

(33) Lee, W. P.; Routh, A. F. Time Evolution of Transition Points in Drying Latex Films. *J. Coatings Technol. Res.* **2006**, *3* (4), 301–306.

(34) Lee, W. P.; Routh, A. F. Temperature Dependence of Crack Spacing in Drying Latex Films. *Ind. Eng. Chem. Res.* **2006**, *45*, 6996–7001.

(35) Le Berre, M.; Chen, Y.; Baigl, D. From Convective Assembly to Landau - Levich Deposition of Multilayered Phospholipid Films of Controlled Thickness. *Langmuir* **2009**, *25* (5), 2554–2557.

(36) Brewer, D. D.; Allen, J.; Miller, M. R.; Santos, J. M. De; Kumar, S.; Norris, D. J.; Tsapatsis, M.; Scriven, L. E. Mechanistic Principles of Colloidal Crystal Growth by Evaporation-Induced Convective Steering. *Langmuir* **2008**, *24* (23), 13683–13693.

(37) Steward, P. A.; Hearn, J.; Wilkinson, M. C. An Overview of Polymer Latex Film Formation and Properties. *Adv. Colloid Interface Sci.* **2000**, *86*, 195–267.

(38) Singh, K. B.; Tirumkudulu, M. S. Cracking in Drying Colloidal Films. *Phys. Rev. Lett.* **2007**, *98* (21), 218302.

(39) Yow, H. N.; Goikoetxea, M.; Goehring, L.; Routh, A. F. Effect of Film Thickness and Particle Size on Cracking Stresses in Drying Latex Films. *Journal of colloid and interface science*, 2010, *352*, 542–548.

(40) Petersen, C.; Heldmann, C.; Johannsmann, D. Internal Stresses during Film Formation of Polymer Latices. *Langmuir* **1999**, No. 11, 7745–7751.

(41) Routh, F.; Russel, W. B. Horizontal Drying Fronts during Solvent Evaporation from Latex Films. *Aiche J.* **1998**, *44* (9), 2088–2098.

(42) Hughes, A. D.; King, M. R. Use of Naturally Occurring Halloysite Nanotubes

for Enhanced Capture of Flowing Cells. *Langmuir* **2010**, *26* (14), 12155–12164.

(43) Weldon, A. L.; Joshi, K.; Routh, A. F.; Gilchrist, J. F. Uniformly Spaced Nanoscale Cracks in Nanoparticle Films Deposited by Convective Assembly. *J. Colloid Interface Sci.* **2017**, *487*, 80–87.

(44) Chaudhury, M. K.; Chakrabarti, A.; Ghatak, A. Adhesion-Induced Instabilities and Pattern Formation in Thin Films of Elastomers and Gels. *Eur. Phys. J. E* **2015**, *38* (7).

CHAPTER 3

Role of surface energy gradient

3.1. Introduction

We have learned so far that the convective deposition is entirely governed by the evaporation rate. The flow inside a meniscus is dictated by the evaporation flux due to a slower substrate velocities. However, as briefly discussed in chapter 2, a presence of surface energy gradient can alter the flow behavior. In the following chapter, we will discuss a typical case (surfactant concentration, binary solvent, temperature variation, etc.) of surface energy gradient, as shown in Fig. 3.1. The motive behind this study is, we encounter these cases in one, and another way, e.g. many colloidal particles are stabilized using a surfactant. Typically a suspension has an excess surfactant present. If a particles' size is small or density matching with the solvent density, a centrifuge washing of an excess surfactant becomes a tedious task. In such a case knowledge of the effect of surfactant will aid an experimentalist to make the appropriate adjustments. Also, heating the substrate or evaporation from the interface creates the temperature gradient. This could possibly lead to instability. On the other hand, a mixture of the binary solvent has a potential to speed up the process.

For surfactant studies, since silica microspheres acquire negative charge in an aqueous medium, it would be appropriate to use anionic surfactant over cationic surfactant. Cationic surfactant might destabilize the suspension. Sodium docile sulfate (SDS) is commonly available and well-studied surfactant, which is preliminary used in all the following experiments. The SDS doesn't have any direct interaction with particles surface,[1] so we can isolate the effect of surfactant. Unlike in the case of polystyrene (PS) particles, SDS has strong affinity at hydrophobic PS surface[1].

A lot of work has been done on how surfactants affect the stability of a colloidal drop[2,3] and how does a surfactant gradient induce a marangoni flow[4]. Research has been done on a classical approach to reversing coffee ring effect by marangoni flow[5–7], Tim Still et al. showed how SDS-induced marangoni flow suppresses coffee ring effect[8] in the sessile drop. Additionally, Zhen Yuan et al. showed how to use surfactant effectively to produce ultrathin films via convective assembly[9]. On the other hand, research also has been done on temperature or surface conductivity induced surface energy gradient[10–12]. Also, M. Majumder et al. showed how to overcome coffee ring effect by compositional marangoni flow[5].

Bond number, $B_o = \rho g R h_o / \gamma$, controls the shape of the drop, where ρ is the density of the liquid, g is acceleration due to gravity, R is a radius of a drop, h_0 is a height of a drop, and γ is a surface tension. Capillary number (Ca) $Ca = \mu U / \gamma$ governs the internal flow inside the meniscus. Here U is average velocity and μ is the viscosity of liquid. However, either in the presence of surface tension gradient, induced by a surfactant or compositional gradient, a liquid surface experiences stress τ, $\tau = d\gamma/dx$ (N/m^2). This stress could lead to marangoni flows inside meniscus [8] as shown in Fig. 3.1.

Marangoni flow is referred to a flow associated with surface energy gradient. Since liquid moves from a lower surface energy to a higher surface energy, the presence of surface energy gradient leads to interfacial flow. This was first observed in so-called “Tears of wine” effect[11].

Fig. 3.1b shows the evaporation driven surfactant gradient across the thin film. The concentration of a surfactant is higher at the 3-phase contact line compared to the bulk suspension, which leads to marangoni flow ($\partial\gamma/\partial x$) in the opposite direction of substrate velocity. Fig. 3.1c shows a composition driven marangoni flow in a case of binary solvent (water + ethanol). Since ethanol is a more volatile of two, ethanol concertation decreases in the thin film compare to the bulk suspension, which leads to marangoni flow ($\partial\gamma/\partial x$) in the same direction of substrate velocity. Fig. 3.1d demonstrates an idea of surface energy gradient created in the heated substrate and evaporating interface.

In the following work, we have attempted to extrapolate the drying droplet theory to the much-complicated pseudo steady process of particle assembly during convective deposition. So far we know that the relation between the number of layers and substrate withdrawal velocity is given by Nagayama equation[13], which assumes pseudo steady state flux balance. This equation assumes convection is entirely associated with evaporation flux as in the coffee ring effect. The water penetrates through the porous media and eventually evaporates. The drying length ℓ is a complicated function of the capillary number as shown in the previous chapter. This assumption is not valid in the presence of surface energy gradient. The flux is governed by both evaporation and marangoni flow.

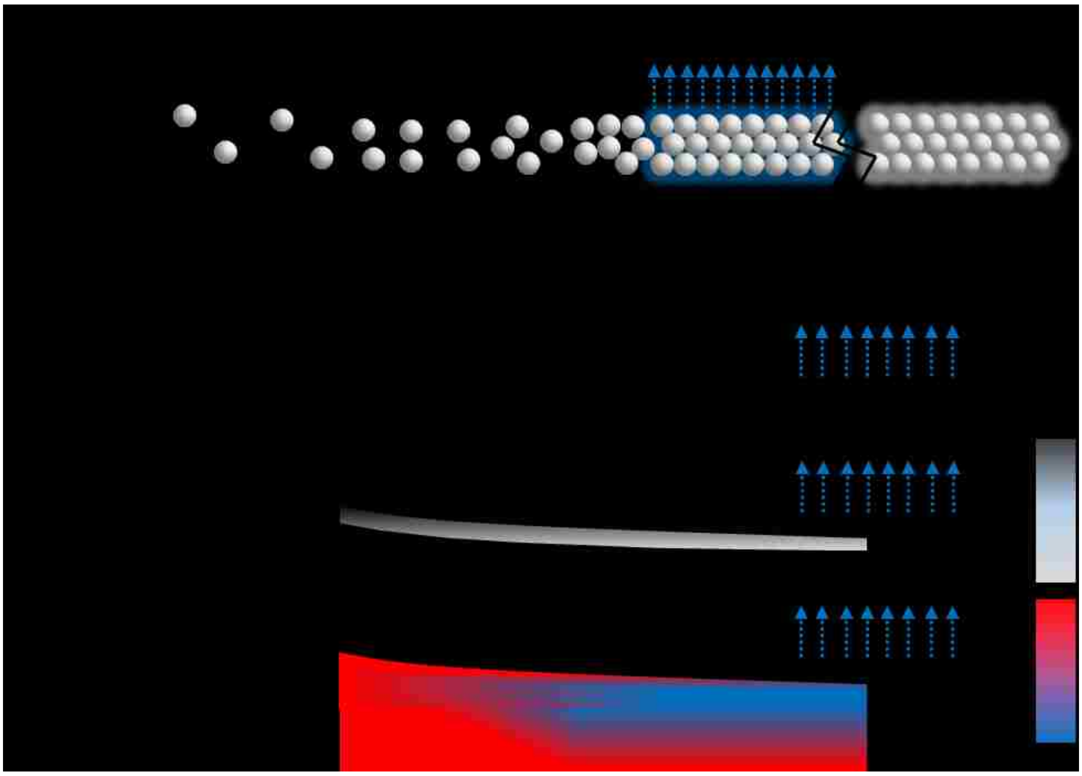

Figure 3.1 It illustrates the different scenarios of surface energy gradient a) Thin film development in the convective deposition with surface energy gradient. b) surfactant concentration is higher in thin film due to evaporation which leads to negative surface energy gradient (in opposite direction of substrate velocity), c) ethanol concentration is lower near the 3-phase contact line due to higher evaporation, which leads to positive surface energy gradient, d) The externally heated substrate or the interfacial evaporation will result in temperature-induced surface energy gradient.

.

3.2. Materials and methods

Preparation of substrate and suspension is done as described in chapter 2. Ultrapure SDS is obtained from United States Biochemical (USB). And 200 proof ethanol is obtained from Fisher Scientific.

3.2.1. Experimental conditions

All the experiments were performed keeping relative humidity (20 ± 1) % and temperature around 24^{o}C. The experimental setup is shown in Figure 1. The deposition blade was fixed at 45^o angle approximately 10μm above the blade. The colloid suspension was injected into the wedge between the substrate and deposition plate, 10 μl volume of suspension was used to draw meniscus in each experiment

3.2.2. Microstructure analysis

Deposited monolayers are observed directly using confocal laser scanning microscopy after rewetting the layer with an aqueous solution of 8 mM Rhodamine B. The relative microsphere substrate coverage, ρ, and the local bond order, Ψ_6, were evaluated.

3.2.3. Macrostructure analysis

The overall sample structure is analyzed using the high-resolution scanner. Samples are scanned in dark room with very high resolution, then cropped in interested area. The topology is studied using ImageJ software. The intensities observed are calibrated to an actual number of layers using confocal microscope and profilometer. Figure 3a shows the scanned sample 3b shows the intensity graph and 3c show the calibration curve. The samples are not uniform at lower speeds and consist of different grains with different thickness. With this method, we can determine overall average thickness by Beer’s law. Also, we can learn streak formation as well from this approach.

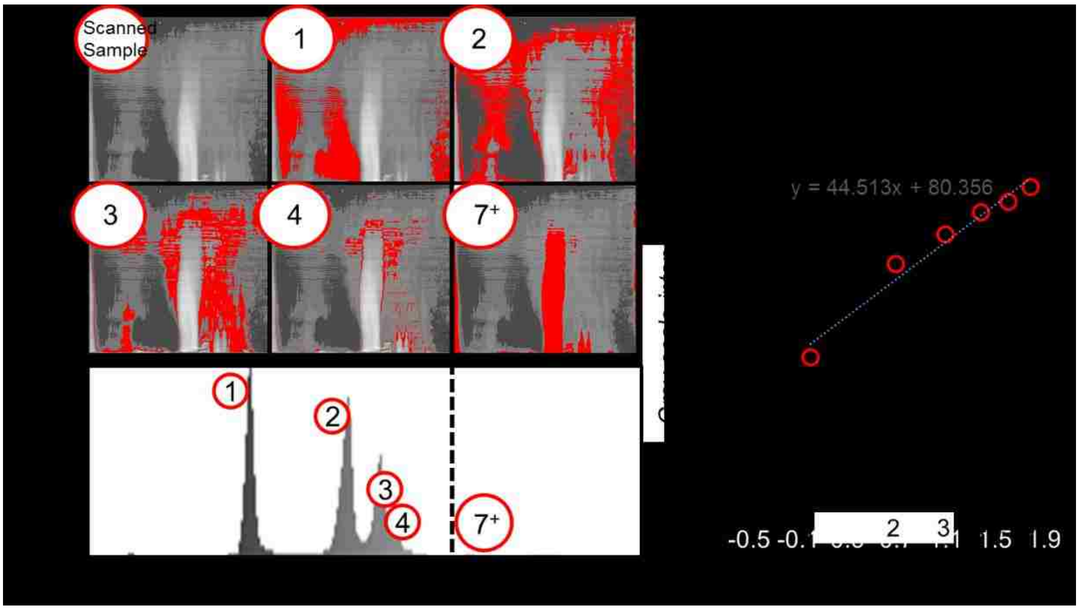

Figure 3.2 a) high resolution scanned sample with different thickness regions b) the intensity corresponds to a particular number of layer. The picks get broad with thickness and c) intensity varies logarithmically with coating thickness. (**Note**: the graph is calibrated for 1µm SiO_2 particles)[a]

---

[a] This gives excellent validation of number of layers, but tells nothing about the microstructure, i.e. Ψ_6 value. The resolution is of an order of 10µm^2 area, which corresponds to approximately 100 particles.

3.3. Results and discussions

3.3.1. Effect of surfactant

Previous studies show below certain SDS concentration w/w% (ξ), recirculation is negligible[8,14]. We have observed similar results with different concentration regimes. Strong ramifications of recirculation have only seen at high ξ (above CMC ≡ 0.23w/w %) values. The reason for the significance of marangoni flow only above CMC is not very well understood, but the possible explanation might be strong repulsion between SDS molecules due of head group interactions[8].

Fig. 3.3 shows monolayer velocities for different SDS concentration. Monolayer velocity window is commonly narrow in the case of convective deposition. Coatings are very sensitive to substrate velocity and outside conditions. This makes the process less flexible since small changes can compromise the quality of crystal. Previous studies focus on increasing this monolayer window by changing particle-solvent-substrate interactions[15] or by the aid of mechanical vibration[16]. Fig. 3.3 shows the monolayer window remains more or less unchanged for ξ< CMC[b], but the significant widening of monolayer region is observed at ξ=1.

---

[b] There is nothing special about the value of CMC. Similar effect could be observed at much lower concentration for some other surfactant.

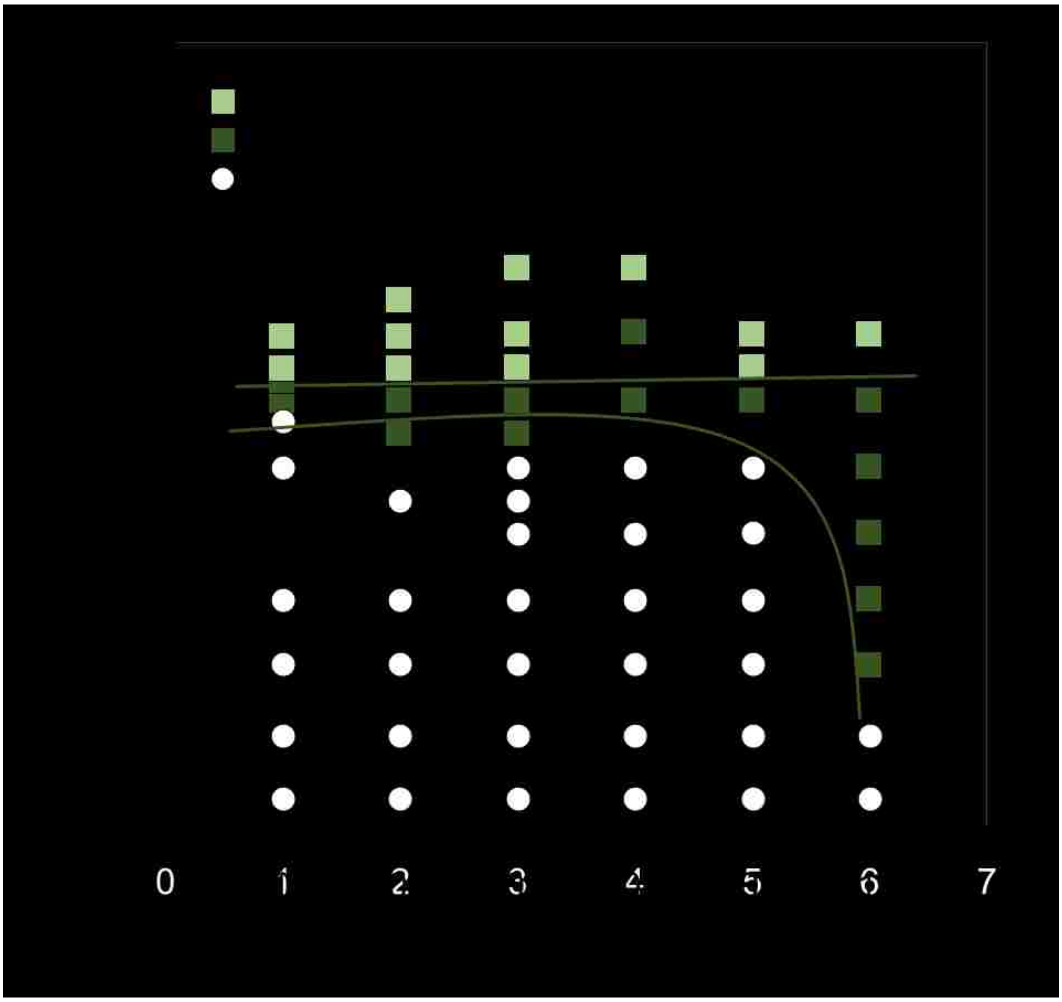

Figure 3.3 monolayer velocity (u_s) as a function of SDS concentration (ξ). The noticeable widening in the monolayer is observed for ξ=1. Dark brown squares represent monolayer. Circles represent multilayer, and light pink squares represent submonolayer. Dark brown lines illustrate the monolayer range widening.

Observation of monolayer velocity range around CMC revealed remarkable details of marangoni dominant regime transition (Fig. 3.4a). In order to quantify this marangoni recirculation, we experimentally measured the drying length (ℓ) around CMC. Drying length implies the extent of liquid penetration into a porous structure. As previous work shows for completely evaporation dominated system ℓ varies as an inverse function of u_s[17]. This length scale depends on initial liquid penetration velocity into particle bed. Because of the marangoni recirculation, this liquid penetration velocity drops. Fig. 3.4b explains the systematic decrease of drying length with increasing ξ. For ξ=0, the flow is completely dominated by evaporation rate. Drying length scales inversely with substrate velocity, ℓ gradually ebbs with increasing ξ and also deviates from the inverse pattern. For ξ =1, drying length is entirely independent of substrate velocity i.e. flow is completely dominated by marangoni recirculation.

Additionally, for ξ =1, drying length is much shorter because of continuous depinning of the contact line. The assembly happens in small parts rather than continuous. This marangoni recirculation acts as flow control feedback system to supply just enough suspension from bulk meniscus to the obtained monolayer. This feedback loop broadens monolayer velocity domain. Significance widening of monolayer velocity range increases the flexibility of process by a great extent.

The quality of monolayer is slightly lower (slight lower particle coverage 'ρ') because of SDS deposition, but locally the structure is very crystalline (high bond order Ψ_6) Fig.3.5a and 3.5b. The monolayer region remains similar to control silica suspension at lower ξ, ξ << CMC. Fig. 3.6 shows the absence of substrate velocity on the morphology of coating at ξ=1. The sample is prepared by changing substrate velocity in a periodic manner. The one samples spans six different substrate velocities

(83.3μm/s, 66.7μm/s, 50μm/s, 41.6μm/s, 33.3μm/s, 25μm/s), yet produces similar coating. The shining rainbow patterns show the quality of crystal. This shows the flexibility of obtaining the monolayer coating. The transition between a substrate velocity is done by pausing the linear motor for 10s in each step. The faint line represents the transition, which has caused by the quick accumulation of particles.

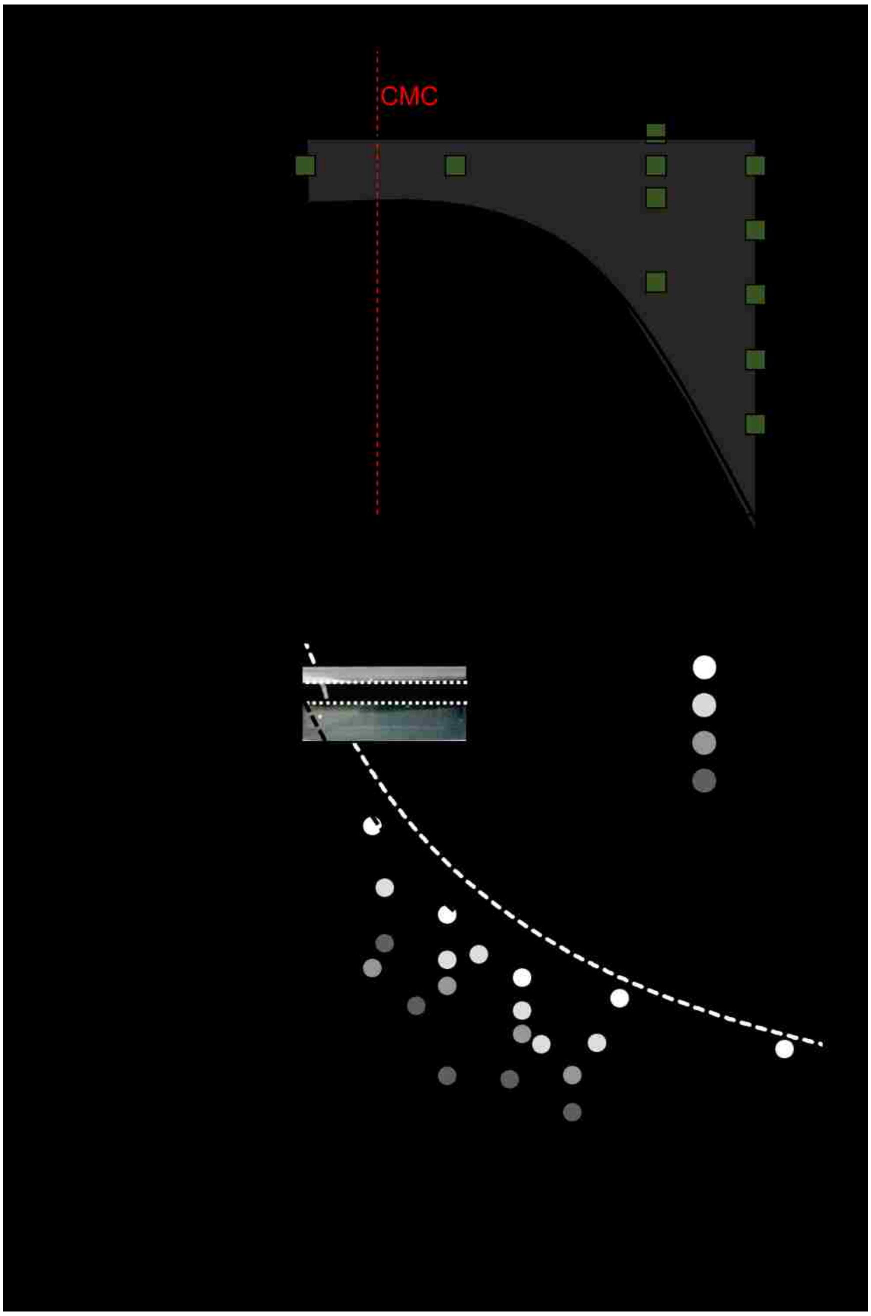

Figure 3.4 a) transition of monolayer region about CMC, monolayer region widens at 1% w/w SDS, b) circles represent drying length at different ξ as a function of substrate velocity (u_s), for a control silica suspension the drying length shows inverse trend with the substrate velocity, which deviates more and more with increasing ξ. For ξ =1, the drying length is completely independent of substrate velocity i.e. marangoni recirculation is dominant flow. ○: ξ=0 control, ○: ξ=0.1, ●: ξ=0.4, ●: ξ=0.8, ●: ξ=1.

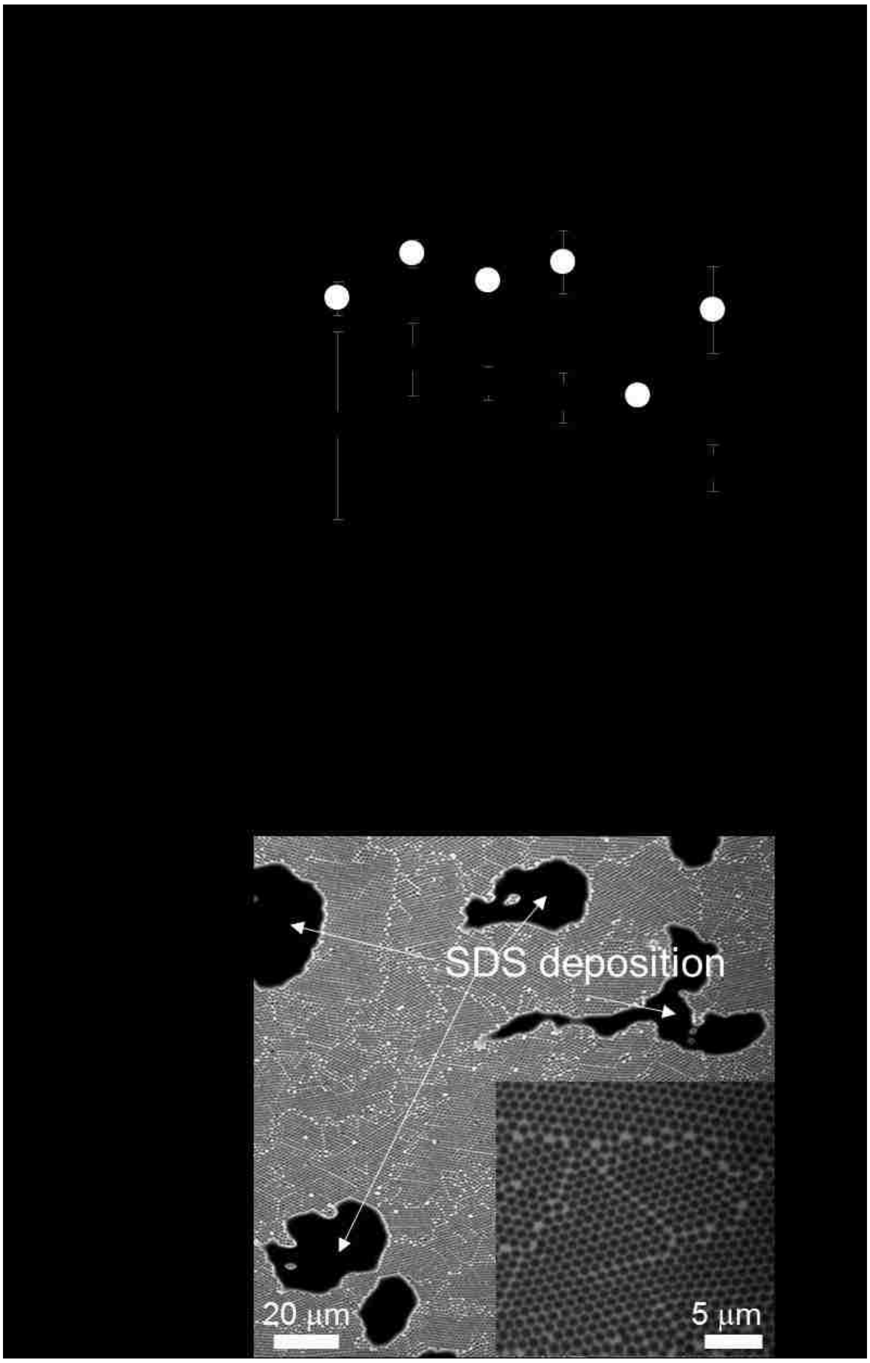

Figure 3.5 a) empty circles corresponds particle coverage ρ and filled circles corresponds to $<\Psi_6>^2$ values of monolayers, b) confocal image of monolayer showing deposited surfactant ξ =1, causes a little decrease in particle coverage, but the structure is very crystalline (Ψ_6^2). The dark color is the result of the failure of dye penetration in SDS deposits.

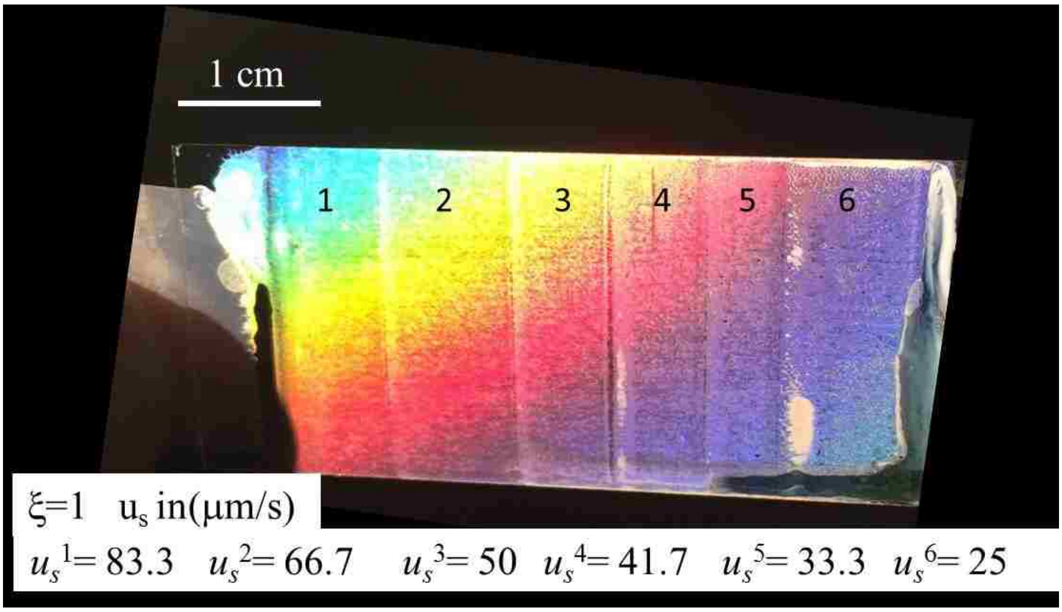

Figure 3.6 Sample produced at $\xi=1$ by changing the substrate velocity periodically. The coating morphology remained same for all six different substrate velocities (83.3μm/s, 66.7μm/s, 50μm/s, 41.7μm/s, 33.3μm/s, 25μm/s). The transition between a substrate velocity is done by pausing the linear motor for 10s in each step. The faint line represents the transition, which has caused by the quick accumulation of particles.

3.3.2. Effect of binary solvent

The effect of binary solvent in a case of the water-ethanol mixture is a completely opposite as that of surfactant[11,18]. Since ethanol evaporates faster and has lower surface tension, the concentration of ethanol (C), decreases near 3-phase contact line (Fig. 3.1c). Since the marangoni flow in the case of the water-ethanol mixture is in the direction of substrate velocity, this effect agitates the system more. The marangoni stress strength can be controlled by maintaining ethanol vapor pressure in surroundings. Saturated ethanol vapor is the extreme case, in which water evaporation is higher than that of ethanol. This phenomenon was studied previously for reversing coffee ring effect[5]. Depending on the concertation of ethanol we see different morphologies. Ethanol concentration is mentioned in solvent volume fraction.

I. Low ethanol concentration (<20%)

The motivation behind ethanol addition is to increase the coating velocity by increasing the evaporation rate. Using a pure ethanol leads to the significant streak formation. Thus a binary mixture of solvents could possibly be a better alternative. Streaks are well explained in chapter 5. The marangoni flow in a case of ethanol agitates the flow in the thin film. Marangoni flow will help in increasing the coating velocity and might avoid any streaking instability.

The marangoni flow is less dominant in a case of low ethanol concentration, but it helps in suppressing the natural streaks formation at lower substrate velocities. The usual coating starts with a thick deposition of particles, which is followed by a fingerprint type structure (Fig. 3.7a). Since the ethanol is much less, it evaporates rather quickly. This result in the formation of two drying fronts. First ethanol and followed by water drying (Fig. 3.7b). The fingerprint type structure might have caused by a periodic marangoni flow, but we are not very certain. The wavelength of fingerprints has shown no particular dependence on the substrate velocity. Since much of the ethanol evaporates quickly resulting in a thick coating at the start, which is quite trivial observation.

II. Medium ethanol concentration (30%-50%)

The marangoni flow is dominant in this concentration range of ethanol. Faster coatings are possible in this range. Since a bulk meniscus contains sufficient ethanol to sustain with the marangoni flow, we don't observe any fingerprint structures. Marangoni flow governs the thin film formation, similar to that for very high surfactant concentrations. This allows performing experiments at much higher substrate velocities. Marangoni flow provides an enough particle flux for the formation of a monolayer. Of course, the quality of such faster coatings is much lower than a control convective deposition. The monolayer regions are identified using the calibrated intensity profiles. The monolayer structure is rather similar to that of obtained by the Landau-Levich technique. We performed experiments by varying the substrate velocity in a range of (400-700 μm/s). This is approximately 10 times faster than a usual monolayer velocity range. Figure 4.8 demonstrates that in 30-50% ethanol, the monolayer percentage is very high.

III. High ethanol concentration (>60%)

The suspension behaves like a single solvent suspension. Due to very high evaporation rates, streaking instabilities occur. This range of concentrations not only exhibits streaks, but also thin film instabilities (Fig. 3.9). A similar study performed by Hosoi et al., which showed similar longitudinal rolls formation on an inclined plane due to surface deformation[11]. We have observed quite similar structures for 50-100 mm/s substrate velocities. On the other hand, for very high substrate velocities (400-700 μm/s), no similar monolayer regions are obtained compared with 30-50% ethanol concentration. Marangoni flow cannot cope up at faster substrate velocity.

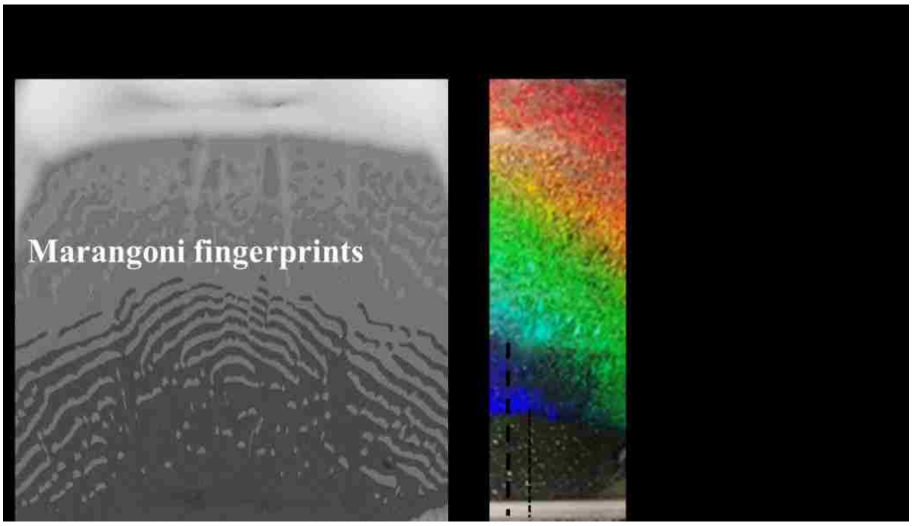

Figure 3.7 a) Marangoni fingerprints observed at lower ethanol concentration, b) lower ethanol concentration leads to two separate drying fronts. Water drying follows ethanol drying.

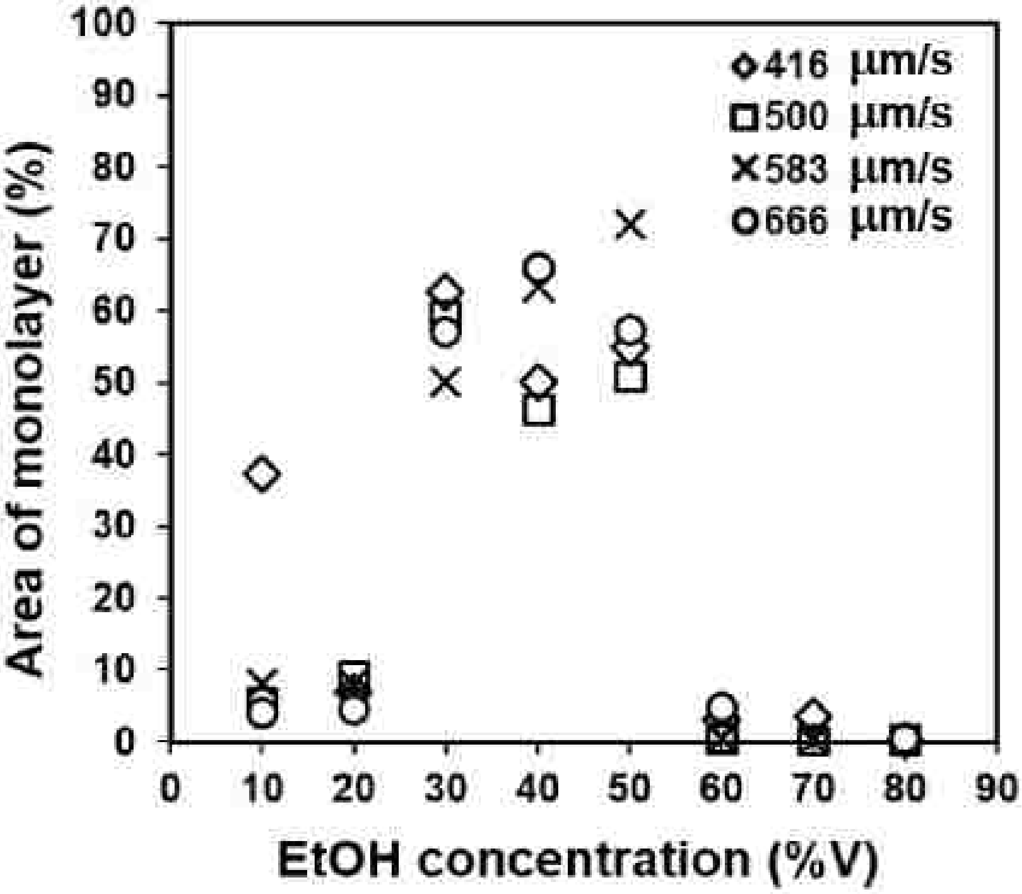

Figure 3.8 Percentage area of monolayer obtained at different ethanol concentrations, for much higher substrate velocities. (Ethanol concentrations are plotted as volume percentage of solvent).

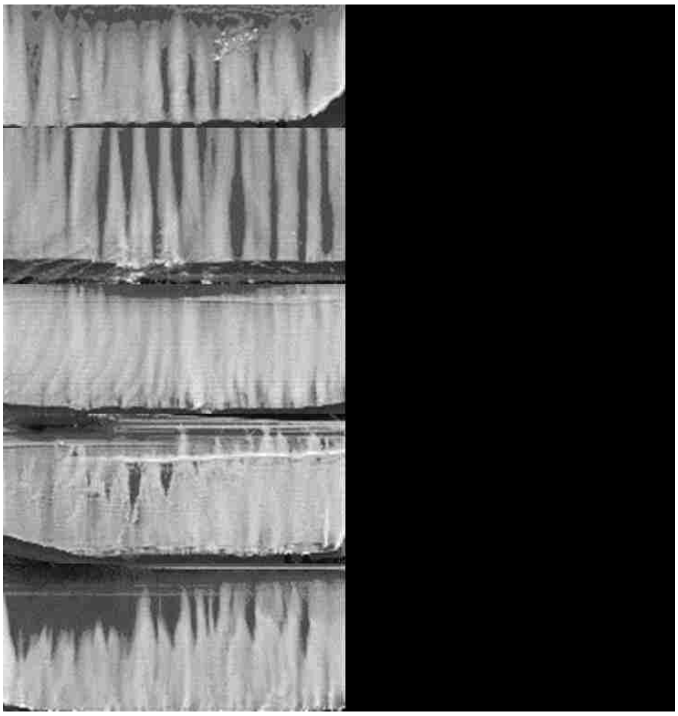

Figure 3.9 Instabilities caused at higher EtOH concentrations.

3.4. Conclusion

In the first part, we performed a separate study of surfactant effect on the convective deposition without changing surface properties of particles. Reverse marangoni flow is caused due to surfactant concentration gradient on the interface. This marangoni flow eloquently participates only above CMC. This counter flow provokes a depinning of the contact line, which has been effectively used in broadening of monolayer range. Marangoni flow acts as a flow control switch of the thin film, providing just enough suspension to obtain monolayer. Additionally, the crystal quality is retained at this high surfactant concentration. In the later part, we studied the effect of the ethanol-water mixture on the convective assembly. This shows that a final morphology is very sensitive to the concentration of ethanol. The final results are not very conclusive, but they give the overall picture of different coating region as a function of ethanol concentration.

References

(1) Brown, W.; Zhao, J. Adsorption of Sodium Dodecyl Sulfate on Polystyrene Latex Particles Using Dynamic Light Scattering and Zeta Potential Measurements. *Macromolecules* **1993**, *26*, 2711–2715.

(2) Danov, K. D.; Danov, K. D. Effect of Surfactants on Drop Stability and Thin Film Drainage. *Fluid Mech. Surfactant Polym. Solut.* **2004**, No. 463, 1–38.

(3) Danov, K. D.; Ivanov, I. B.; Ananthapadmanabhan, K. P.; Lips, A. Disjoining Pressure of Thin Films Stabilized by Nonionic Surfactants. *Adv. Colloid Interface Sci.* **2006**, *128–130* (2006), 185–215.

(4) Mayer, H. C.; Krechetnikov, R. Landau-Levich Flow Visualization: Revealing the Flow Topology Responsible for the Film Thickening Phenomena. *Phys. Fluids* **2012**, *24* (5), 1–33.

(5) Majumder, M.; Rendall, C. S.; Eukel, J. A.; Wang, J. Y. L.; Behabtu, N.; Pint, C. L.; Liu, T. Y.; Orbaek, A. W.; Mirri, F.; Nam, J.; et al. Overcoming The "coffee-Stain" effect by Compositional Marangoni-Flow-Assisted Drop-Drying. *J. Phys. Chem. B* **2012**, *116* (22), 6536–6542.

(6) Yiantsios, S. G.; Higgins, B. G. Marangoni Flows during Drying of Colloidal Films. *Phys. Fluids* **2006**, *18* (8).

(7) Hu, H.; Larson, R. G. Marangoni Effect Reverses Coffee-Ring Depositions. *J. Phys. Chem. B* **2006**, *110* (14), 7090–7094.

(8) Still, T.; Yunker, P. J.; Yodh, A. G. Surfactant-Induced Marangoni Eddies Alter the Coffee-Rings of Evaporating Colloidal Drops. *Langmuir* **2012**, *28* (11), 4984–4988.

(9) Yuan, Z.; Burckel, D. B.; Atanassov, P.; Fan, H. Convective Self-Assembly to Deposit Supported Ultra-Thin Mesoporous Silica Films. *J. Mater. Chem.* **2006**, *16* (48), 4637.

(10) Gugliotti, M.; Baptista, M. Surface Tension Gradients Induced by Temperature :

The Thermal Marangoni Effect. *J. Chem. Educ.* **2004**, *81* (6), 824–826.

(11) Hosoi, a. E.; Bush, J. W. M. Evaporative Instabilities in Climbing Films. *J. Fluid Mech.* **2001**, *442*, 217–239.

(12) Ristenpart, W. D.; Kim, P. G.; Domingues, C.; Wan, J.; Stone, H. a. Influence of Substrate Conductivity on Circulation Reversal in Evaporating Drops. *Phys. Rev. Lett.* **2007**, *99* (23), 1–4.

(13) Dimitrov, A. S.; Nagayama, K. Steady-State Unidirectional Convective Assembling of Fine Particles into Two-Dimensional Arrays. *Chem. Phys. Lett.* **1995**, *243* (5–6), 462–468.

(14) Le Berre, M.; Chen, Y.; Baigl, D. From Convective Assembly to Landau - Levich Deposition of Multilayered Phospholipid Films of Controlled Thickness. *Langmuir* **2009**, *25* (5), 2554–2557.

(15) Joshi, K.; Muangnapoh, T.; Stever, M. D.; Gilchrist, J. F. Effect of Ionic Strength and Surface Charge on Convective Deposition. *Langmuir* **2015**, *31* (45), 12348–12353.

(16) Muangnapoh, T.; Weldon, A. L.; Gilchrist, J. F. Enhanced Colloidal Monolayer Assembly via Vibration-Assisted Convective Deposition. *Appl. Phys. Lett.* **2013**, *103* (18).

(17) Kedar Joshi, J. G. Estimation of Drying Length during Particle Assembly by Convective Deposition. *J. Colloid Interface Sci.* **2017**, *1*.

(18) Hu, H.; Larson, R. G. Analysis of the Effects of Marangoni Stresses on the Microflow in an Evaporating Sessile Droplet. *Langmuir* **2005**, *21* (9), 3972–3980.

CHAPTER 4

Effect of surface charge and ionic strength

4.1. Introduction

The thin film profile is dependent on deposition velocity u_s and solvent physical properties such as surface tension γ, viscosity η, and density ρ. This much knowledge is enough in the case of fast Landau Levich[1–3] coatings. Although, in the case of capillary force driven assembly of particles as in convective deposition, particle interactions with other particles and substrate even with interface become crucial. Stability of suspension, particles interactions in the thin film play a great deal of role in final assembly structure.

$$u_s = \frac{\beta J e \ell \phi}{\varepsilon d n (1-\phi)} \tag{1}$$

In the Nagayama equation[4], we know that all the interactions are left out in a single parameter β. From the process designing point of view, it is vital to correlate β. It is associated with the mismatch of flux between solvent and particles happened due to different interactions of particles. Over the thin film solvent velocity is not uniform (usually parabolic) in a z-direction. Since particles concentration varies in height due to different interactions, particles flux no longer agrees with solvent flux. Different particles interact defiantly with the substrate as well as the interface. The basic tool for particle interactions is a surface charge σ, and surface properties and the medium for interactions is free charges present in solvent i.e. ionic strength I and ions properties. In the following study, we have demonstrated the effect of surface charge and different ionic strength suspensions over the final assembly.

There are numerous studies of the effects of added electrolytes on self-assembly of particles[5–9] and the effects of different surface active groups to change particle-substrate interactions[10–12]. The addition of salt decreases Debye length, thereby further screening the effects of electrostatic repulsion. Rödner et al. have shown the effects of electrolytes on structural changes of monolayer silica particle films[5]. Similar to evaporation-driven deposition, drop drying is affected by DLVO interactions resulting in varying the shape of dried droplets[7]. In a convective deposition, using binary suspensions of large and small microspheres has led to higher order with less streaking instabilities, although the mechanism is poorly understood[13,14]. Similarly, added lateral vibration during deposition has been shown to increase the degree of order in deposited monolayers as well as increasing the range of velocities in which monolayers can be obtained from essentially a single ideal velocity, as suggested in Eq. 1, to a wide range of velocities[15]. This added lateral vibration is highly complex, adding motion of the free interface and local shear within the thin film. It is thought that this added motion of the particles gives a bit extra stability to particles through lubrication between the particles and substrate, allowing for further annealing of the nearly deposited particles. However, it is unclear how this stability allows for a range of monolayer velocities. In this study, the particle-surface electrostatic interaction can be tuned independent of the imparted flow, resulting in a broadened range of velocities that result in monolayer coatings and giving additional insight into the mechanism of broadening the monolayer deposition range.

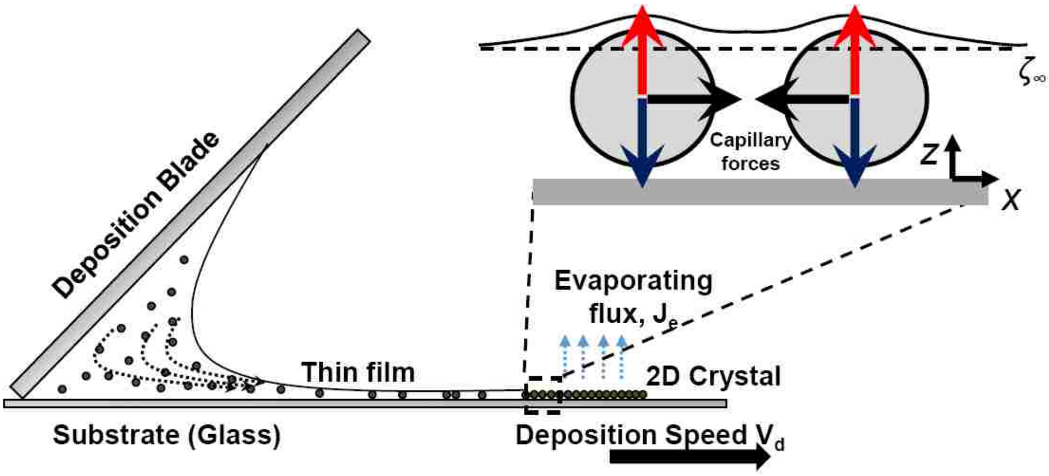

Figure 4.1 Experimental setup showing equipment where a meniscus is pulled relative to the substrate to induce deposition and the local ordering of particles due to capillary forces.[a]

---

[a] Reprinted with permission from [Joshi K., Muangnapoh T., Stever M.D., and Gilchrist J.F. “Effect of ionic strength and surface charge on convective deposition” *Langmuir* **2015** 31(45) 12348-12353]. Copyright © American Chemical Society.

4.2. Theoretical background

Here I have discussed a basic principles of Van der Waal, electrostatic forces, and DLVO theory. This will be brief, but it will be useful in appreciating results. In the bulk suspension, particles interact with each other by Van der Waal and Electrostatic forces. The combination of two theories known as DLVO. Although, when a thin film is drawn out of suspension, a thin film of colloids interacts with the substrate and interface as well. When the film becomes considerably thin, air interface and substrate get very close, and solvent interactions become crucial in determining the stability of the thin film. This is known as disjoining pressure.

4.2.1. Van der Waal forces

They also are known as Long-range forces or London dispersion forces. They exist because of permanent or induced dipole interactions[16]. They can be either attractive or repulsive depending on two materials and medium separating those materials. Since these forces exist at the atomic/molecular level, they are important in almost every system[16]. In a convective deposition, we are particularly interested in Van der Waal interactions between particle and substrate separated by a solvent as well as particle and air separated by the solvent.

Van der Waal forces between a sphere and a plane are given by following equation[17].

$$U_V(D) = {-A_{132}r}\big/{6D} \tag{2}$$

Here D is the distance between 2 bodies A_{132} is effective (interactions between phase 1 and phase 2 separated by phase 3) Hamaker constant. A_{132} is given by the following equation.

$$(A_{132}) = (A_{11}^{1/2} - A_{33}^{1/2})\,(A_{22}^{1/2} - A_{33}^{1/2}) \tag{3}$$

A_{ii} is Hamaker constant for phase *i* separated from phase *i* in a vacuum. From Eq. (3) we can deduce that A_{132} can be either positive or negative. A_{ii} can be determined by different methods. For common materials, A_{ii} can be found in the literature. For following experiments in which SiO_2 particles are deposited on a glass slide and water as a solvent, phase 1 is SiO_2 phase 2 is air/SiO_2, and phase 3 is water as shown in Fig. 4.2.

4.2.2. Electrostatic repulsive forces

As the particle size increases, only Brownian forces are not enough to stabilize the suspension. Particles can stabilize themselves for a longer duration by surface charge. Surface charge introduces repulsive forces which avoid agglomeration and thus reduces sedimentation velocity. There are a couple of ways particles can acquire surface charge in an aqueous medium. One of the common mechanism is adsorption of charge, and the other way could be dissociation of surface group[16].

With a surface charge, σ, there is an associated surface potential Ψ_0. This potential diffuses in bulk suspension by creating a concentration gradient. Here osmotic pressure is balanced by electrostatic forces[18].

From Poisson equation, we can write,

$$\nabla^2\Psi = -(\rho / \varepsilon) \tag{4}$$

Where Ψ is potential and ρ is charge density ($|n^+ - n^-|$). From Boltzmann distribution, we can get charges distribution,

$$n_i \big/ n_\infty = \exp\left(\frac{-Ze\Psi}{K_B T}\right) \tag{5}$$

Assuming Ψ is smaller and Taylor expansion we arrive at simple equation

$$\left(\nabla^2\Psi\right) = \kappa^2\Psi \tag{6}$$

Where $\kappa^2 = \left[\left(e^2 / \varepsilon K_B T \right) \sum_i z_i^2 n_{i\infty} \right]$ and κ^{-1} is called Debye length. Eq. (6) can be solved for specific geometry using proper boundary conditions. For particle and substrate interactions field equation is given as follows[17].

$$U_E(D) = 64 r \pi \varepsilon \varepsilon_0 \left(\frac{K_B T}{ze} \right)^2 \tanh^2 \left(\frac{ze\Psi_0}{4K_B T} \right) e^{-\kappa D} \tag{7}$$

The apparent charge of silica particles[19] in water is modulated by the dissociation of silanol groups (SiOH) present at the surface. This equilibrium is sensitive to the presence of OH^- ions in bulk suspension. In this study, the surface charge is modified by controlling an amount of OH^- ions by adding NaOH[20],

$$SiOH + OH^- \leftrightarrow SiO^- + H_2O \tag{8}$$

4.2.3. *Hydration forces*

These forces originate from interactions between particles and nearby solvent molecules[21]. These are particularly important from earlier experiments[22] when the wetting angle is less than 15° or more than 64°. These forces exponentially decay over small distances.

$$U_H(D) = W_0 \exp(-D/\lambda_0) \tag{9}$$

W_0 and λ_0 are constants.

4.2.4. *Disjoining pressure*

Disjoining pressure is important in thin film stability. As the liquid film gets thinner, this causes stronger interactions between the air-liquid interface and the substrate and depending on their properties energy increases or decreases as a function of thickness. The total free energy can be expressed as the sum of apolar (LW) and polar interactions (P)[23–25].

$$\Delta G_{132} = \Delta G_{132}^{LW} + \Delta G_{132}^{P} \tag{10}$$

$$\Delta G_{132}^{LW} = S^{LW}\left({d_0}^2 \big/ h^2 \right) \tag{11}$$

$$\Delta G_{132}^{P} = S^{P}\left(\exp\left(\frac{(d_0 - h)}{l} \right) \right) \tag{12}$$

S^{LW} and S^{P} are LW spreading coefficient and polar spreading coefficient respectively. d_0 is bond repulsion length. l is correlated to hydration length. For water like solvent d_0 can be taken as 1.58A^0 and l can vary 2-12A^0 depending on ion's concentration[26,27].

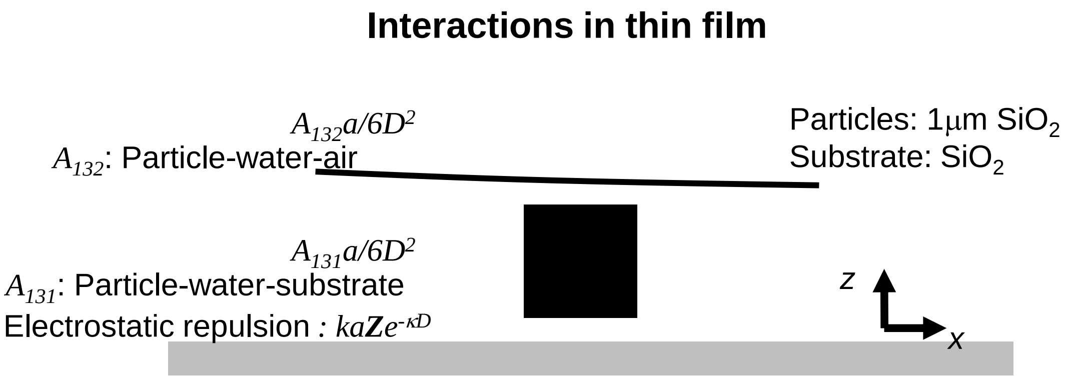

Figure 4.2 Different particle interactions in a thin film. Particle-substrate as well as particle-interface interactions.

4.3. Experimental section

4.3.1. Suspension Preparation

The suspension is made from dispersing silica microspheres in DI water with the volume fraction 0.2. The silica microspheres (Fuso Chemical Co, Japan) have density 2.2 g/ml and average diameter 1.01±0.02 μm. NaCl and NaOH ranged from 10^{-7} to 10^{-3} mol/dm^3 were added to the suspension to observe effects of ionic strength and electrostatic charge. The suspension is dispersed using a sonic dismembrator (model 550, Fisher Scientific, Pittsburgh, PA) for 10 min and stirred for 30 min (Fisher Sci., model 550).

4.3.2. Substrate Preparation

Plain glass micro slides (76x25x1 mm^3, Fisher PA) are used as the deposition blade, and glass coverslips (60x24x0.25 mm^3, Fisher PA) are used as the substrate for all samples. All glassware is cleaned by immersing in a piranha solution, 80:20 v/v sulfuric acid/hydrogen peroxide, for 30 min. The glassware is then rinsed with DI water until no residual acid remains, and the cleaned glassware is immersed in DI water before use. The back and bottom edges of the glass deposition blade are treated to be hydrophobic by adding a thin coating of parafilm (Fisher PA). The contact angle on bare glass and on the hydrophobic surface is kept 45^o respectively, a meniscus of 10 μL suspension is created between the wedge of a substrate and a blade.

4.3.3. Experimental setup

All the experiments were performed keeping relative humidity (20 ± 1) % and temperature around 72^{o}F. The experimental setup is shown in Fig. 4.1. The deposition blade was fixed at 45^o angle approximately 10 μm above the blade. The colloid suspension was injected into a wedge between the substrate and the deposition plate, 10 μl volume of suspension was used to draw meniscus in each experiment. The substrate was then pulled at a certain deposition speed (30 µm/s to 110 µm/s) using a linear motor (Harvard Instruments Co. Ltd.)

4.3.4. Microstructure analysis

Deposited monolayers are observed directly using confocal laser scanning microscopy after rewetting the layer with an aqueous solution of 8 mM Rhodamine B. The sample is scanned at 3 fps while translating the sample across the microscope objective at 100 µm/s using a motorized stage. Optical imaging of the sample was automated along the deposition length sampling ~1,000,000 microspheres. The relative microsphere substrate coverage, ρ, and the local bond order, Ψ_6, were evaluated. The maximum theoretical value of surface coverage for monosized microspheres deposited as a two-dimensional hexagonally close-packed (HCP) crystal is $\rho = \frac{\pi}{(12)^2} = 0.907$.

The long-range microsphere substrate coverage is qualitatively reported. Ψ_6 is a parameter describing the relative crystallinity of particles. It is calculated using angles θ between each particle of interest i and their nearest neighbors j. Vectors r_{ij} are determined for all nearest neighbors N and Ψ_6 is defined as

$$\Psi_6\left(r_{ij}\right) = \frac{1}{N}\sum_{j=1}^{N}\exp\left[6i\theta\left(r_{ij}\right)\right] \tag{13}$$

Where $\Psi_6 = 1$ describes particles oriented in a perfect hexagonally close-packed crystal.

4.4. Results and Discussions

4.4.1. Surface charge measurements

Zeta potential experiments were done to analyze the variations in surface charge. It was observed that the zeta potential decreases with an addition of NaOH while it remains relatively constant with an addition of NaCl (Fig. 4.3). These measurements suggest that the addition of NaOH alters both ionic strength and surface charge, zeta potential keeps decreasing in given range of concentration. On the other hand, the addition of NaCl alters only in ionic strength[9]. Zeta potential remains almost constant.

4.4.2. Sedimentation experiments

For hydrophilic particles with 1 μm size as SiO_2 DLVO theory works well. To decide experiment range we use DLVO mathematical simulation aid. The results confirmed by sedimentation experiments also by literature[5]. This allows us to use DLVO theory with confident for this particular system.

DLVO takes both Van der Waal and electrostatic interactions in the account. With the addition of two potentials, we can deduce the free energy as a function of distance. Hamaker constant (A) for glass water glass system is positive with value 1.6-3.2[28]. With both calculations and experiments, we found out the critical aggregation concentration for both NaOH and NaCl. Aggregation starts first in NaCl since it doesn't increase the surface charge. Fig. 4.4a shows how the potential barrier for aggregation drops as ion concentration decreases and at particular concentration it vanishes. Van der Waal forces dominate over that concentration causing sudden aggregation and sedimentation Fig. 4.4b

4.4.3. Effects on assembly

A series of experiments were performed to elucidate the role of particle-surface interactions during particle assembly (Fig. 4.5). Three primitive conditions were examined. First, convective deposition was carried out at constant pH while varying ionic strength, [NaCl]. Second, experiments investigating the effect of surface charge through varying pH and ionic strength through the addition of NaOH, $[OH^-]$. Third, the effect of surface charge is investigated by varying the ratio of $[OH^-]$ and [NaCl] to keep overall ionic strength constant. For each solution, convective deposition was performed to determine the range of velocities that produces submonolayer, monolayer, and multilayer morphologies. Finally, the microstructure of submonolayer samples is analyzed to give further evidence to the role of ionic strength and surface charge in the capillary-driven assembly during deposition.

I. Surface charge effects

Similar to previous results utilizing mechanical vibration to aid deposition of particles[15], increasing the surface charge through increasing $[OH^-]$, thereby increasing the particle-substrate repulsion while decreasing the κ^{-1}, alters the breadth of the range of velocities that result in monolayer deposition (Fig. 4.5c). The region between two dashed lines is defining viable monolayer velocity for 20% volume fraction silica suspension at 20% relative humidity. We observed the broadening of the monolayer region to $60 < V_c < 85$ mm/s for $10^{-6} < [OH^-] < 10^{-5}$ mol/dm^3 as compared to particles in deionized water indicated as $[OH^-] = 10^{-7}$. At higher $[OH^-]$, this broadening of the crystallization velocity is less evident. Since the addition of OH^- changes both surface charge and ionic strength, the effect of ionic strength has been studied separately in section 4.2. The monolayer hexagonal order parameter, Ψ_6, is relatively high in all the conditions having added NaOH. This suggests the addition of surface charge has no particular effect on the final microstructure.

II. Ionic strength effects

Particle-particle and particle-substrate interactions depend on the screening length. Here, the ionic strength was varied ranging $10^{-7} \leq [\mathrm{NaCl}] \leq 10^{-3}$ mol/dm^3 (Fig. 4.5a). At each ionic strength, there is essentially a single point, a narrow range of velocities, where the particles are deposited as a monolayer, as predicted by Eq. (1). Submonolayer and multilayer morphologies are deposited at faster and slower deposition speeds, respectively. The velocity that results in monolayer deposition is essentially unaffected for $[\mathrm{NaCl}] < 10^{-4}$. For $[\mathrm{NaCl}] \geq 10^{-4}$ there is a monotonic decrease in the velocity that yields a monolayer coating of particles. Because these experiments were performed at constant conditions other than different ionic strength, the only two possible parameters in Eq. (1) could justify the broadening the range of velocities that result in monolayer deposition are $\beta\, and\ \ell$. While ℓ is a complex balance between the Laplace pressure of deposited particles. At one end where the meniscus jumps on the order of the particle size and Darcy flow exists between this point and the point where particles self-assemble, the addition of salt should result in a modest change in contact angle, surface energy, and evaporation rate. The addition of salt changes Debye length thus changing the particle-particle and particle-substrate interactions. Because we are using very high volume fraction suspension Debye length depends on bulk concentration[29] as

$$\kappa^{-1}(\phi) = \kappa_0{}^{-1}\sqrt{\frac{1-\phi}{1+3\sigma\phi/(eqd)}} \tag{14}$$

$$\kappa^{-1}{}_0 = \left(\frac{(\varepsilon\varepsilon_0)K_B T}{\sum_i q_i e^2 z_i 2}\right)^{1/2} \tag{15}$$

Where κ^{-1} is the Debye length and κ_0^{-1} is the Debye length at the infinite diluted suspension, σ is the surface charge density on silica particle, q is the ionic density (C/m^3) and e is the primary charge on a single electron. Particle-particle screening dominates at a lower salt concentration up until [NaCl] ≥ 10^{-4} mol/dm^3 upon which the ionic strength decreases the Debye length significantly. This trend is shown on, Fig. 4.3a suggesting the trend of monolayer deposition velocity is related to the effective degree of screening. The particle-substrate interaction decreases as κ^{-1} decreases, thus reducing V_c.

Apart from the decrease in monolayer velocity, we observed a significant reduction in local bond order for $10^{-4} \leq$ [NaCl] $\leq 10^{-3}$. If the particles are attracted by capillary interactions at the crystal front, the crystallinity of monolayer is good irrespective of other interactions. As κ^{-1} decreases, the mobility of particles near the substrate also decreases. Likewise, capillary forces are weaker when the particles reside lower in the film relative to the equilibrium thin film height as shown in Fig. 4.1. In order to investigate more, we calculate electrostatic barrier as a function of particle-substrate separation and the resulting effective separation distance without applied capillary interactions[30,31].Eq. (2) and Eq. (7) determines the Van der Waal and electrostatic interactions between particles and substrate[17].

The total energy is given by $U(d) = U_E(d) + U_V(d)$ and $F(d) = -{}^{\partial U(d)}\!/_{\partial x}$

As shown in Fig. 4.6a, the electrostatic repulsions are unaffected for [NaCl] < 10^{-5} mol/dm^3 because of the particles volume fraction screening. The effective repulsion decreases with the further addition of NaCl. At [NaCl] ~ 0.1 mol/dm^3 the suspension becomes unstable and particles aggregate, confirmed using sedimentation experiment and previous work[5]. Minimum separation distance given by DLVO theory is shown in Fig. 4.6b, decreasing from 89 nm for [NaCl] = 10^{-4} mol/dm^3 to 37 nm for [NaCl] = 10^{-3} mol/dm^3. As the electrostatic repulsion dominates and particles come very close the surface, disjoining pressure acts more strongly over electrostatic repulsion. If disjoining pressure is strong enough the water film will become unstable[23–25] and particles are deposited on the substrate before they reach crystal front, disrupting the crystalline order. Apolar (S^W) and polar spreading coefficient (S^P) for the glass-water-glass system can be calculated using interfacial surface tension values[23,25,26].

Additionally, the only difference between particle in bulk suspension and the thin film is liquid-air interface is much closer to the particle. Particle-substrate interactions as shown above modify because of these interface interactions. We can write interface interactions using equation (10-12) S^{LW} and S^P can be calculated as shown above. The total energy is given by DLVO and interface interactions Eq. (16). Fig. 4.8a gives a schematic representation of particles between two interfaces. The polar interactions of liquid-air interface exponentially drop over a small distance (Eq. 12). As l increases with salt concentration, two potential starts overlapping and DLVO repulsion which keep particle separated from a substrate is effectively reduces (Fig. 4.8b). Our calculations suggest that thin water film above silica particles will rupture between 10^{-4}-10^{-3} salt concentration Fig. 4.7 shows the hydration calculation graph which shows the dropping of potential between 10^{-4}-10^{-3} salt concentration. Previous experimental studies by Frederik J. Lech et al. also shows rupture at similar salt concentrations[32,33]. Both experiments and our calculations were done assuming water film forming on the flat glass surface, but in the actual process, the film is separating 1μm particle from the air. So, there present an intrinsic curvature which exerts Laplace pressure that can shift the rupture criteria even at lower salt concentration.

Above calculations suggest that the system will not be stable after critical water thickness. Which will result in particles forming small aggregates before they reach crystal front, this may reduce Ψ_6. This hypothesis explains both observations since particles are forming premature crystals, the quality goes down. Additionally, particles moving close to a substrate which decreases monolayer velocity. In order to investigate this further, we investigate submonolayer depositions to study the local microstructure of every NaCl concentration in Fig. 4.9, discussed below.

Even though extensive analysis of particle-substrate interactions gives a fair description of results, other interactions exist in this system which should be considered. For example, out of plane electrostatic interactions can be significant [34,35] and highly complex as we alter the surface charge and Debye length. Likewise, disjoining pressure can alter the liquid-air interface[34], and whether particles breach the interface and interact using capillary forces while pinned at the interface [36] or simply trapped within the liquid layer will alter these interactions. This can cause premature breaching of particles which can result in random deposition. These particle-particle interactions near the interface are sensitive to salt and surfactant addition[37] where increasing salt concentration leads to weaker interactions. More focused particle-level experiments need to be done before making any conclusions in our dynamic system where particles flow and are subjected to these various interactions in the thin film. Future studies altering particle size may enhance these various interactions where their contribution can be isolated.

III. Variation in surface charge with constant ionic strength [I] $=10^{-3}$

Above two sets of experiments show that the surface charge increases monolayer window with keeping same monolayer quality, the addition of ions compromises the quality. Although to isolate the effect of just surface charge, following experiments are done at constant bulk ion concentration at [I] $=10^{-3}$. Keeping the ions concentration same we changed the ratio of [NaOH: Bulk ions] from 0-1. There was a clear shift in monolayer window as we increased OH^- ions concentration. From left to right the graph (Fig. 4.5b) smoothly transfer from Fig. 4a to Fig. 4c. Again the similar submonolayer analysis reveals the microstructure changes (Fig. 4.9).

Addition of salt affects the vapor pressure; Raoult's Law[38]. Salt concentration changes the evaporation rate in porous media[39]. Salts interactions changes the transport properties in porous bed. However, this effect is significant and has been studied at much higher salt concentration[39]. This effect is not considered in this research, but could be done in future studies.

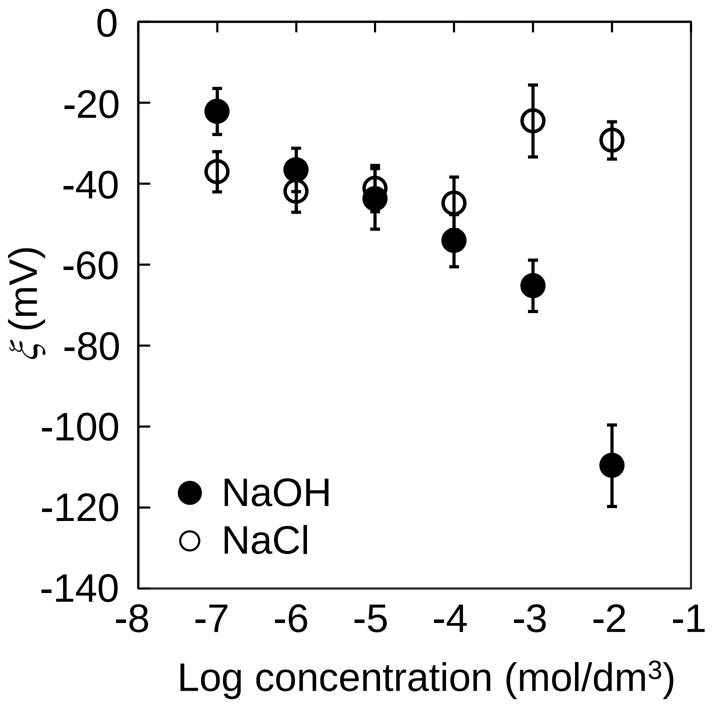

Figure 4.3. Zeta potential (ξ) as function of concentration of both NaCl and NaOH (mol/dm^3).[b]

---

[b] Reprinted with permission from [Joshi K., Muangnapoh T., Stever M.D., and Gilchrist J.F. "Effect of ionic strength and surface charge on convective deposition" *Langmuir* **2015** 31(45) 12348-12353]. Copyright © American Chemical Society.

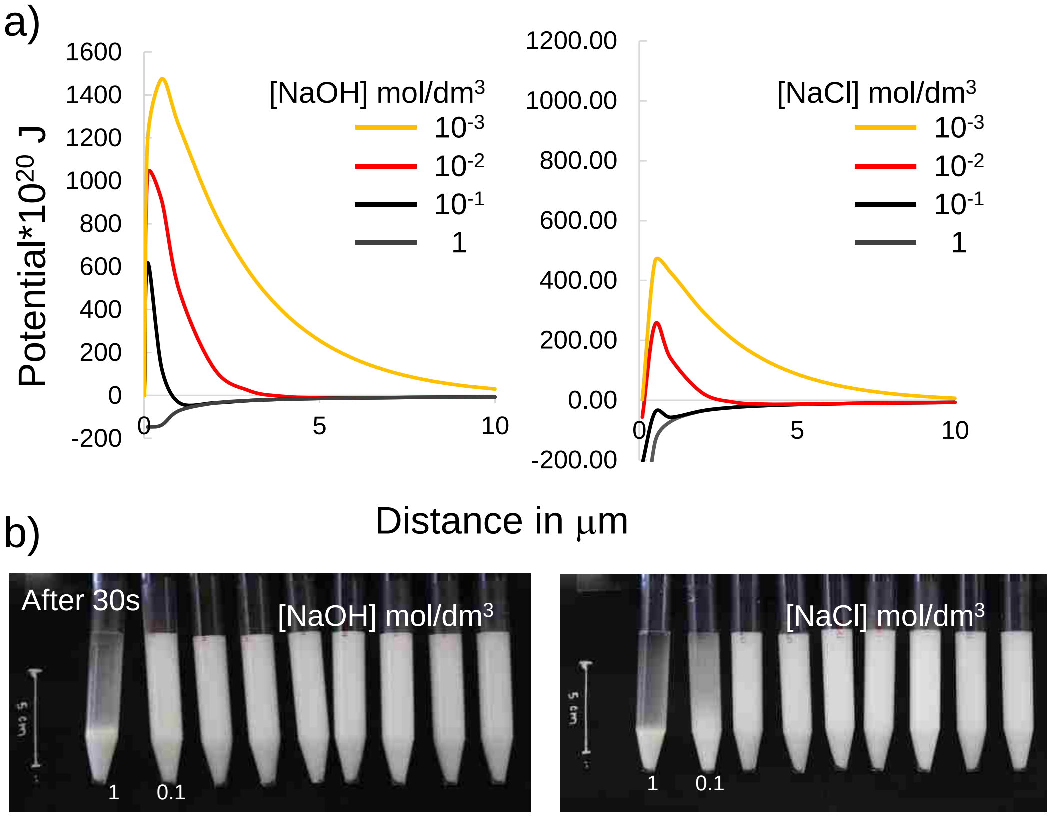

Figure 4.4 a) DLVO potential barrier for dilute suspension as a separation distance for different NaOH and NaCl concentrations, in mol/dm^3 — 10^{-3}, — 10^{-2} — 10^{-1} — 1, b) sedimentation of 1% v/v suspension at different NaOH and NaCl concentration matching DLVO predictions.

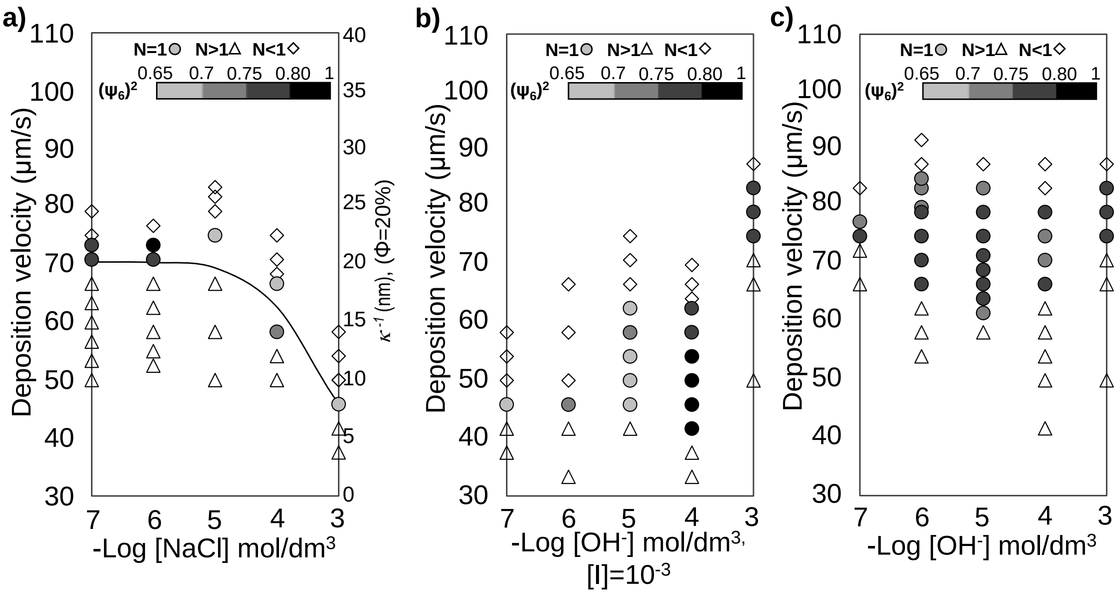

Figure 4.5 Deposition morphology as a function of deposition velocity for changes in solution a) ionic strength, b) surface charge at constant ionic strength, and c) surface charge for added pH. Particle coatings include multilayer (Δ), submonolayer (◊), and monolayer (o) morphologies. The monolayer symbols are shaded according to their degree of order, indicated by Ψ_6^2. The monolayer velocity as a function of ionic strength (a), by varying [NaCl], is compared to the calculated screening length in solution, κ^{-1} b) depositions performed at constant ionic strength, [I]=10^{-3} while varying [OH$^-$], c) monolayer as function of [OH$^-$].[c]

---

[c] Reprinted with permission from [Joshi K., Muangnapoh T., Stever M.D., and Gilchrist J.F. "Effect of ionic strength and surface charge on convective deposition" *Langmuir* **2015** 31(45) 12348-12353]. Copyright © American Chemical Society.

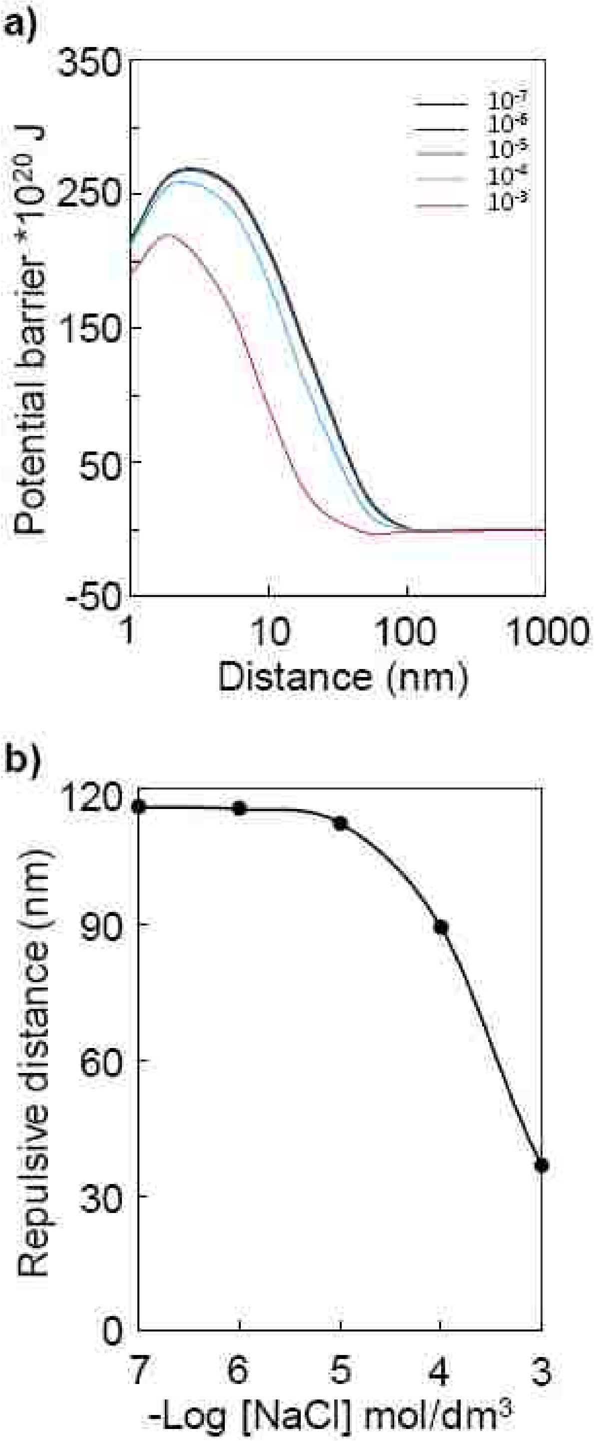

Figure 4.6 a) effective potential barrier as a result of a combination of Van der Waal attraction and repulsive electrostatic forces between particle-substrate, as a function of distance their distance (nm), b) Minimum separation distance (nm) from DLVO as a function of NaCl concentration (mol/dm^3).[d]

---

[d] Reprinted with permission from [Joshi K., Muangnapoh T., Stever M.D., and Gilchrist J.F. “Effect of ionic strength and surface charge on convective deposition” *Langmuir* **2015** 31(45) 12348-12353]. Copyright © American Chemical Society.

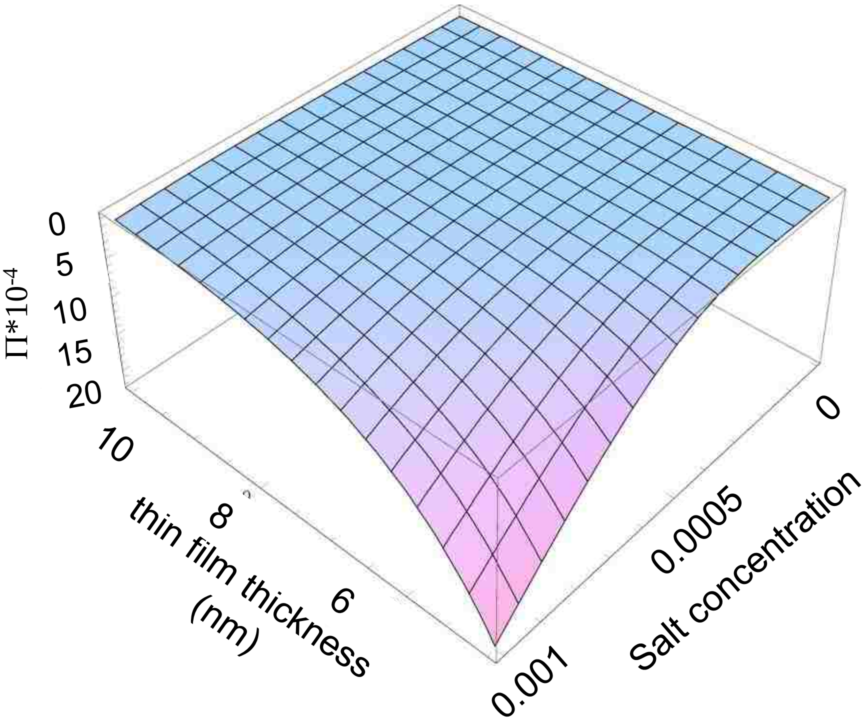

Figure 4.7 disjoining pressure of water film separating silica particle from the air as a function of salt concentration (mol/dm^3) and film thickness. Destabilization occurs between 10^{-4} and 10^{-3} mol/dm^3.

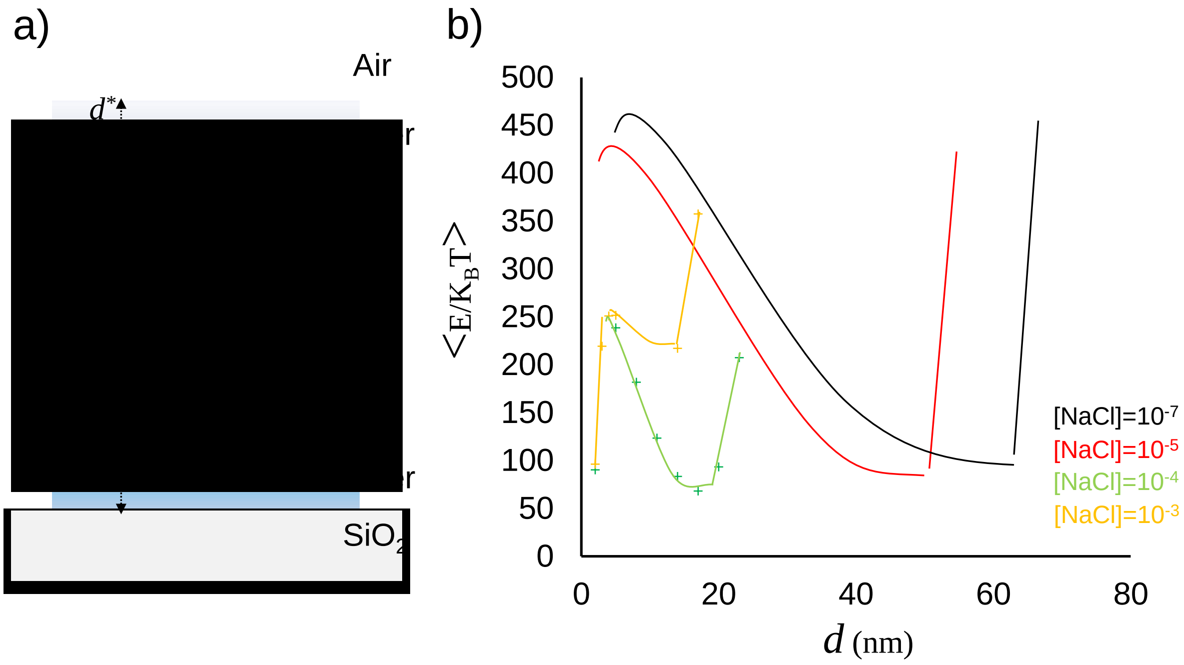

Figure 4.8 a) silica particle trapped between water-substrate and water-air interface, b) potential energy normalized by K_BT as function of distance *d* from substrate for different salt concentrations [NaCl] in (mol/dm^3), black line represents: 10^{-7}, red line represents:10^{-6}, green line represents:10^{-4}, orange line represents:10^{-3} . Potential barrier vanishes as salt concentration goes up. Polar interactions take over DLVO repulsion.

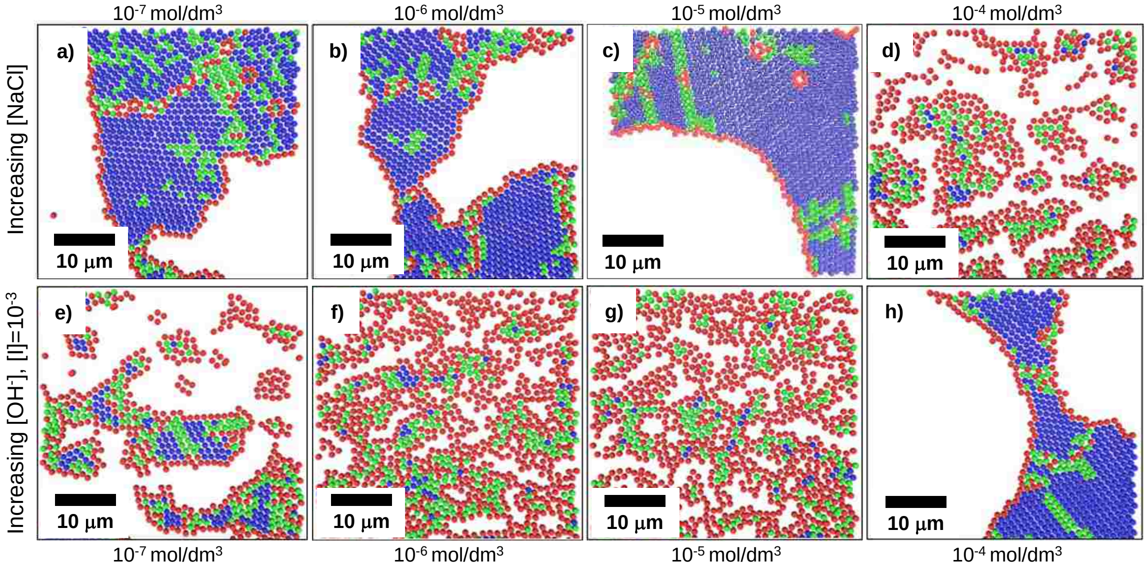

Figure 4.9 Rendered sub-monolayer microstructures from confocal scans. Blue particles represent particles with six nearest neighbor and local bond order $\Psi_6 > 0.8$, green particles represent particles with six nearest neighbor with local bond order $\Psi_6 < 0.8$, and red particles represent less than six nearest neighbors. a-d) Varying [I] with concentrations a) [NaCl] $=10^{-7}$ mol/dm^3, b) [NaCl] $=10^{-6}$ mol/dm^3, c) [NaCl] $=10^{-5}$ mol/dm^3, d) and [NaCl] $=10^{-4}$ mol/dm^3. E-f) [I] = 10^{-3} mol/dm^3 through balanced addition of NaCl and varying surface charge at concentrations a) [OH$^-$] $=10^{-7}$ mol/dm^3, b) [OH$^-$] $=10^{-6}$ mol/dm^3, c) [OH$^-$] $=10^{-5}$ mol/dm^3, d) [OH$^-$] $=10^{-4}$ mol/dm^3.[e]

---

[e] Reprinted with permission from [Joshi K., Muangnapoh T., Stever M.D., and Gilchrist J.F. "Effect of ionic strength and surface charge on convective deposition" *Langmuir* **2015** 31(45) 12348-12353]. Copyright © American Chemical Society.

4.5. Conclusions

Derived from a simple mass balance, the Nakayama equation is accurate in predicting a single monolayer velocity under ideal conditions. However, the variability of particle substrate and particle−particle interactions that occur due to capillary and electrostatic interactions, summarized in one parameter β, inaccurately gives the notion that only one ideal set of conditions can result in monolayer deposition. The ability to have a range of monolayer velocities, first seen in a vibration-assisted convective deposition, is reproduced here varying surface charge and ionic strength. Higher ionic strength leads to lower monolayer deposition velocity due to particles residing closer to the substrate and the eventual destabilization of particles at high ionic strength. Added surface charge reverses this trend, adding stability to particles and allowing them to assemble into higher order structures. The advantage of tuning these interactions is knowing under what conditions to expect variability in the deposition conditions to yield the desired structure and the ability to have a wider range of deposition velocities that can result in essentially the same structure. This second point is particularly important when considering industrial-scale processes that may utilize thin film flows for ordering particles through capillary and electrostatic interactions. Robustness in operating parameters may translate to lower requirements for control and more flexibility in process design.

References

(1) Mayer, H. C.; Krechetnikov, R. Landau-Levich Flow Visualization: Revealing the Flow Topology Responsible for the Film Thickening Phenomena. *Phys. Fluids* **2012**, *24* (5), 1–33.

(2) Le Berre, M.; Chen, Y.; Baigl, D. From Convective Assembly to Landau - Levich Deposition of Multilayered Phospholipid Films of Controlled Thickness. *Langmuir* **2009**, *25* (5), 2554–2557.

(3) Juan Schneider. Method and Apparatus for Thin Film/layer Fabrication and Deposition, 2010.

(4) Dimitrov, A. S.; Nagayama, K. Continuous Convective Assembling of Fine Particles into Two-Dimensional Arrays on Solid Surfaces. *Langmuir* **1996**, *12* (5), 1303–1311.

(5) Rödner, S. C.; Wedin, P.; Bergström, L. Effect of Electrolyte and Evaporation Rate on the Structural Features of Dried Silica Monolayer Films. *Langmuir* **2002**, *18* (24), 9327–9333.

(6) Aveyard, R.; Binks, B. P.; Clint, J. H.; Fletcher, P. D. I.; Horozov, T. S.; Neumann, B.; Paunov, V. N.; Annesley, J.; Botchway, S. W.; Nees, D.; et al. Measurement of Long-Range Repulsive Forces between Charged Particles at an Oil-Water Interface. *Phys. Rev. Lett.* **2002**, *88* (24), 246102.

(7) Bhardwaj, R.; Fang, X.; Somasundaran, P.; Attinger, D. Self-Assembly of Colloidal Particles from Evaporating Droplets: Role of DLVO Interactions and Proposition of a Phase Diagram. *Langmuir* **2010**, *26* (11), 7833–7842.

(8) Beresford-Smith, B.; Chan, D. Y. .; Mitchell, D. J. The Electrostatic Interaction in Colloidal Systems with Low Added Electrolyte. *J. Colloid Interface Sci.* **1985**, *105* (1), 216–234.

(9) Kershner, R. J.; Bullard, J. W.; Cima, M. J. The Role of Electrochemical Reactions during Electrophoretic Particle Deposition. *J. Colloid Interface Sci.* **2004**, *278* (1), 146–154.

(10) Graf, C.; Vossen, D. L. J.; Imhof, A.; Van Blaaderen, A. A General Method to

Coat Colloidal Particles with Silica. *Langmuir* **2003**, *19* (17), 6693–6700.

(11) Islam, M. F.; Rojas, E.; Bergey, D. M.; Johnson, a. T.; Yodh, a. G. High Weight Fraction Surfactant Solubilization of Single-Wall Carbon Nanotubes in Water. *Nano Lett.* **2003**, *3* (2), 269–273.

(12) Sefcik, J.; Verduyn, M.; Storti, G.; Morbidelli, M. Charging of Latex Particles Stabilized by Sulfate Surfactant. *Langmuir* **2003**, *19* (11), 4778–4783.

(13) Kumnorkaew, P.; Weldon, A. L.; Gilchrist, J. F. Matching Constituent Fluxes for Convective Deposition of Binary Suspensions. *Langmuir* **2010**, *26* (4), 2401–2405.

(14) Kumnorkaew, P.; Gilchrist, J. F. Effect of Nanoparticle Concentration on the Convective Deposition of Binary Suspensions. *Langmuir* **2009**, *25* (11), 6070–6075.

(15) Muangnapoh, T.; Weldon, A. L.; Gilchrist, J. F. Enhanced Colloidal Monolayer Assembly via Vibration-Assisted Convective Deposition. *Appl. Phys. Lett.* **2013**, *103* (18).

(16) Rajagopalan, R.; Hiemenz, P. C. *Principles of Colloid and Surface Chemistry*; 1997; Vol. 70.

(17) Faghihnejad Ali, H. Z. Fundamentals of Surface Adhesion, Friction, and Lubrication. *Polym. Adhes. Frict. Lubr.* **2013**, 1–57.

(18) Adamson, A. W.; Gast, A. P. *Physical Chemistry of Surfaces - 6th Edition*; 1997.

(19) Ralph K. Iler. *The Chemistry of Silica: Solubility, Polymerization, Colloid and Surface Properties and Biochemistry of Silica*; 1979.

(20) E. Papirer. *Adsorption on Silica Surfaces*; 2000.

(21) Benard Binks, T. H. *Colloidal Paticles at Liquid Interfaces .pdf*; 2006.

(22) Israelachvili, J. N.; Pashley, R. . Measurement of the Hydrophobic Interaction between Two Hydrophobic Surfaces in Aqueous Electrolyte Solutions. *J. Colloid Interface Sci.* **1984**, *98* (2), 500–514.

(23) Sharma, A. Stability and Breakup of Thin Evaporating Water Films: Role of

Hydrophobic Interaction. *J. Colloid Interface Sci.* **1998**, *199* (2), 212–214.

(24) Sharma, A. Equilibrium and Dynamics of Evaporating or Condensing Thin Fluid Domains: Thin Film Stability and Heterogeneous Nucleation. *Langmuir* **1998**, *7463* (25), 4915–4928.

(25) Sharma, A. Relationship of Thin Film Stability and Morphology to Macroscopic Parameters of Wetting in the Apolar and Polar Systems. *Langmuir* **1993**, *28* (23), 861–869.

(26) Oss, C. J. V. a N.; Good, R. J.; Van Oss, C. J.; Chaudhury, M. K. Interfacial Lifshitz-van Der Waals and Polar Interactions in Macroscopic Systems. *Chem. Rev.* **1988**, *88* (6), 927–941.

(27) Van Oss, C.; Good, R.; Chaudhury, M.; Oss, C. Additive and Nonadditive Surface Tension Components and the Interpretation of Contact Angles. *Langmuir* **1988**, *4* (4), 884–891.

(28) Ackler, H. D. D.; French, R. H. H.; Chiang, Y. M. M. Comparisons of Hamaker Constants for Ceramic Systems with Intervening Vacuum or Water: From Force Laws and Physical Properties. *J. Colloid Interface Sci.* **1996**, *179*, 460–469.

(29) Jung, B.; Theato, P. Chemical Strategies for the Synthesis of Protein – Polymer Conjugates. *Adv. Polym. Sci.* **2012**, No. May 2012, 1–34.

(30) Elimelech, M. Predicting Collision Efficiencies of Colloidal Particles in Porous Media. *Water Res.* **1992**, *26* (1), 1–8.

(31) Derjaguin B, L. L. Theory of the Stability of Strongly Charged Lyophobic Sols and of the Adhesion of Strongly Charged Particles in Solution of Electrolytes. *Acta Phisicochim* **1941**, *14* (633).

(32) Radoev, B.; Stöckelhuber, K. W.; Tsekov, R.; Letocart, P. Wetting Film Dynamics and Stability. *Colloid Stab. Appl. Pharm.* **2011**, *3*, 151–172.

(33) Lech, F. J.; Wierenga, P. A.; Gruppen, H.; Meinders, M. B. J. Stability Properties of Surfactant-Free Thin Films at Different Ionic Strengths: Measurements and Modeling. *Langmuir* **2015**, *31* (9), 2777–2782.

(34) Park, B. J.; Lee, M.; Lee, B.; Furst, E. M. Lateral Capillary Interactions between

Colloids beneath an Oil–water Interface That Are Driven by out-of-Plane Electrostatic Double-Layer Interactions. *Soft Matter* **2015**.

(35) Park, B. J.; Furst, E. M. Fluid-Interface Templating of Two-Dimensional Colloidal Crystals. *Soft Matter* **2010**, *6* (3), 485–488.

(36) Kaz, D. M.; McGorty, R.; Mani, M.; Brenner, M. P.; Manoharan, V. N. Physical Ageing of the Contact Line on Colloidal Particles at Liquid Interfaces. *Nat. Mater.* **2011**, *11* (2), 138–142.

(37) Park, B. J.; Pantina, J. P.; Furst, E. M.; Oettel, M.; Reynaert, S.; Vermant, J. Direct Measurements of the Effects of Salt and Surfactant on Interaction Forces between Colloidal Particles at Water-Oil Interfaces. *Langmuir* **2008**, *24* (5), 1686–1694.

(38) Pitzer, K. S.; Peiper, J. C.; Busey, R. H. Thermodynamic Properties of Aqueous Sodium Chloride Solutions. *J. Phys. Chem. Ref. Data* **1984**, *13* (1), 1–102.

(39) Rad, M. N.; Shokri, N. Nonlinear Effects of Salt Concentrations on Evaporation from Porous Media. *Geophys. Res. Lett.* **2012**, *39* (4), 1–5.

CHAPTER 5

Spacing of seeded and spontaneous streaks

5.1. Introduction

In chapter 3, we discussed how we can modify the flow profile in a thin film using the marangoni stress. Evan though convective deposition is very effective technique, it is plagued with naturally occurring instabilities called a streak. The streak is a region where particles accumulate due to a local flux inhomogeneity. Flow occurs near the streaks due to enhanced evaporation from accumulated particles in the orthogonal direction to the deposition and parallel direction to the substrate. Fig. 5.1 illustrates a) ideal convective assembly, b) formation of the streak, c) streak spoils uniform coating. The cause behind the streaking phenomenon is yet unknown. But researchers believe, it is caused by the temperature induced marangoni flow during evaporation[1,2]. Alex Weldon gave a lot of valuable insight and statistical analysis of streak formation in the convective assembly of particles[3]. If you are working with the evaporation driven assembly of micron size particles, you must have faced this non-intuitive and frustrating streaking phenomenon. We shall see why size of particles is important in section 5.2.

Even so researchers have found different ways of completely avoiding streaks, e.g. addition of nanoparticles[4,5] or vibration influenced convective assembly[6]. Unfortunately, these methods cannot be implemented for all the situations. Especially when scaling up the process, the vibration of the larger substrate is impractical. Here we have introduced a novel approach to go around this unpredictable phenomenon. We have not avoided the problem, but we have channelized these instabilities so that the coating in between remains unaffected. Fig. 5.2 gives insight about what we are up to:

a) desirable coating, b) random streaks spoiling entire coating area, c) seeded streaks to save in between coating area.

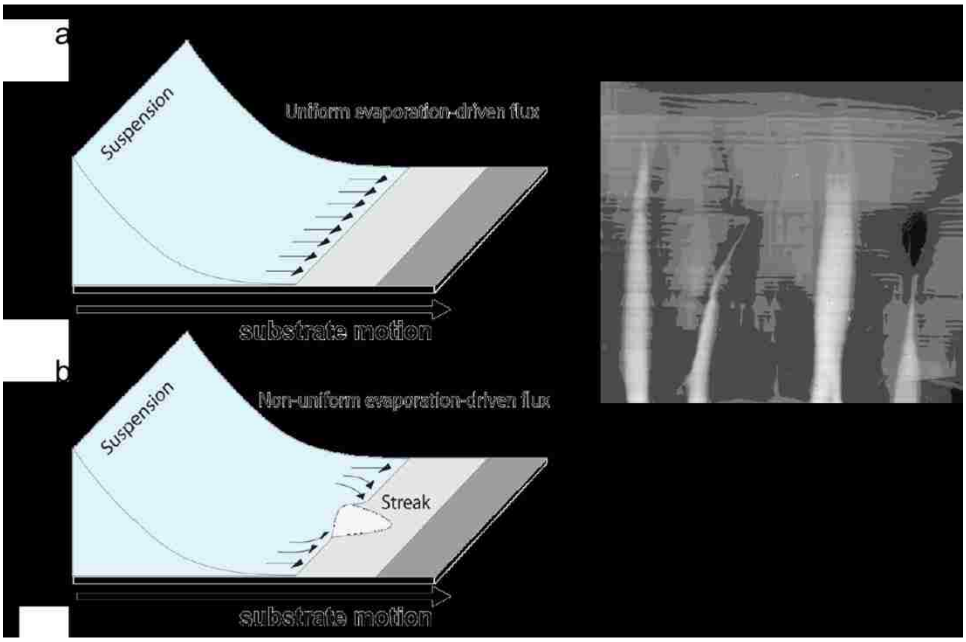

Figure 5.1 (a) Ideal conditions for convective deposition result in a continuously advancing meniscus where the particle flux is uniform. (b) Heterogeneity in the advancing contact line can result in a localized region of multilayer deposition that continues to grow because of the enhanced evaporative flux. (c) Typical sample displaying spontaneous streaks.

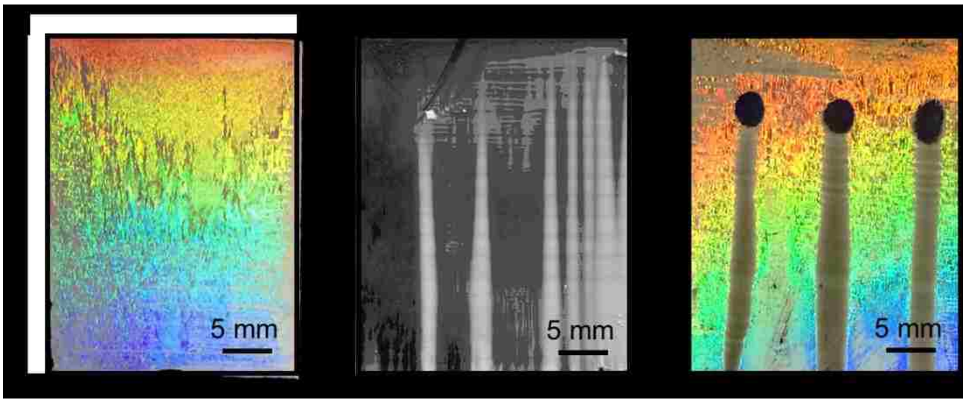

Figure 5.2 a) the desired sample without any streaks, b) random streaks spoils the uniformness, c) seeded streaks leaving behind uniform coating in between.

5.2. Streak formation mechanism

On the macroscopic scale, the onset of a streak could result from any phenomena that cause flow or height variations in the lateral direction. Likewise, streaks may result from Marangoni stresses[7,8] driven by local thermal or concentration gradients. In any sample, the edges of the thin film on a flat substrate almost always demonstrate the formation of a streak like structures because of the local curvature. On the microscopic scale, the assembly of streaks differs from a conventional convective deposition in that convective steering[9] driven by the Darcy flow through the multilayer streak draws particles not just in the direction of the coating but laterally across the substrate. The spontaneous formation of streaks is possibly initiated by contact line fluctuations or fingering[10,11] that enhance the localized evaporation rates at local curvatures, thus drawing particles into the localized region at a faster rate similar to the patterning of drying films[12]. Likewise, streaks can be initiated in regions where the contact line of the advancing meniscus pins to the substrate due to the local variation in surface energy. While generally seen as an inconsistent phenomenon that disrupts the formation of an otherwise homogeneous deposition of particles, one can imagine the generation of streaks with controlled morphologies to achieve fluid transport through pseudo unidirectional lanes of porous media.

Should the streak formation be avoided by higher osmotic pressure? The particle concentration near streaking instability is higher than the bulk concentration, this should be rectified by the osmotic gradient. But, the streaking phenomenon has generally been reported for a weaker Brownian particles (d >500nm). The Peclet number (Ud/D) for the one micron particles is much higher to promote any browning motion. The Peclet number varies as a square of particle diameter. Thus, for nanoparticles (d< 200nm) the osmotic pressure is enough to rectify any concentration gradient of particles. The crude calculation for the Peclet number can be done using kinematic diffusivity of particles ($D = K_B T/6\pi\eta a$).

$D^{1\mu m} \sim 4.75*10^{-13}$ and $D^{100nm} \sim 4.75*10^{-12}$. The range substrate velocities interesting for convective deposition is (10-200μm/s). Thus,

$Pe^{1mm} \sim (20\text{-}400)$ and $Pe^{100nm} \sim (0.2\text{-}4)$.

The colloidal structure formed in the case of convective deposition is irreversible[13–15] except under mechanical vibration of substrate, in which case the structure is believed to be quite dynamic[6].

This study examines streaks initiated at local surface defects, referred to as nucleated or seeded streaks, as well as the spontaneous formation of streaks between seeded streaks. The goal of this ongoing work is to understand better the natural phenomenon of streak formation and explore templated streak formation for possible applications.

5.3. Materials and methods

5.3.1. Suspension and experimental setup

The colloid suspension used in this work is prepared with monosized silica microspheres (Fuso Chemical Co, Japan) with density 2.2 g/cm^3 and an average diameter of 1.01 $\underline{+}$ 0.02 μm, which are dispersed in deionized water for a volume fraction of 20%. The suspension is dispersed using a sonic dismembrator (model 550, Fisher Scientific, Pittsburgh, PA) for 10 min. The experimental setup was described previously[6]. This suspension is deposited onto glass cover slides (40 x 24 x .25 mm^3, Fisher PA) using plain glass microslides (76 x 25 x 1 mm^3, Fisher PA) as the deposition blade via convective deposition. All glassware is cleaned by immersion in piranha solution (5:1 v/v sulfuric acid/hydrogen peroxide) for 30 min. And rinsed with deionized water until no residual acid remains. Once clean, the glassware is immersed in deionized water before use. The back and bottom edges of the glass deposition blade are treated to be hydrophobic to control the wetting region of the meniscus droplet by adding a thin coating of parafilm (Fisher PA). The contact angle on bare glass and on the hydrophobic surface is a measure to by 10^o and 105^o respectively, by imaging a 10 μL stationary droplet on the surface.

5.3.2. Defect preparation

The clean glass cover slides are prepared with defects a certain distance apart, 3 mm < D < 10 mm. Multiple slides are prepared for each distance. Formation of defects is performed using a marker (Sharpie fine point permanent) attached to a drill press depositing hydrophobic ink. A fixed setting is used to allow the consistent formation of defects with controlled width, d. The defects span from one end of the slide to the other forming a line parallel to the short edge of the slide. The number of defects formed ranges from 2 to 5 depending on the maximum amount of the 2 mm defects that can be fit across the 24 mm width for each given D. Control samples were prepared with defects of different widths, $1 < d < 6$ mm by incrementally setting the travel distance on the drill press to let the marker move further downward for each increment. With each increment, marker presses down more onto the glass cover slide and create defects with each desired width.

The apparatus is contained within a controlled environment with a constant 53% relative humidity and 24^{o}C temperature. The deposition blade is set to an angle of $\alpha = 45^{o}$. It is positioned approximately 10 µm above the glass coverslip substrate and 3 mm in front of the line of defects. 10 µL of the colloid silica suspension is injected into the wedge between the substrate and deposition blade. Then, the substrate is pulled at a deposition speed of $u_s = 62.5$ µm/s using a linear motor (Harvard Instruments Co. Ltd). Images of the deposited silica particle layers with the streaks that formed are taken with a standard flatbed image scanner. Image analysis is then used to identify the number of particle layers present in each part of the image, confirmed using a confocal microscope (VTeye, Visitech) and correlating reflectance using Beer's Law. This resulting data allows for the determination of the number of streaks formed as well as the width of these streaks for each of the samples.

5.4. Results and discussion

The formation of a streak during the convective deposition can be initiated by creating a defect such as a local inhomogeneity or seed in the transverse direction with respect to deposition. The defect can be on the substrate or within the receding thin liquid film. These include imparting a local thermal gradient or masking the region just above the thin film to alter the evaporation rate[16] or placing a defect on the substrate itself that spatially alters its height[17] or hydrophilicity[18]. In this study, streaks were initiated by placing a drop of ink on the substrate at various locations. The reproducibility of this technique was first noticed when studying possible ways to use lithography to obtain patterned particle depositions by masking certain regions of the substrate prior to deposition and then etching the mask, thereby removing particles from the surface[19]. The particle deposition conditions for the aforementioned trials as detailed in the Experimental part (section 5.3) were held constant, tuned to what theoretically would yield a monolayer of highly ordered microspheres from a suspension of 1-μm-diameter silica microspheres in water. It should be noted that the deposition conditions, such as evaporation flux, particle concentration and size, and deposition speed, which determine the number of layers of particles deposited may affect the formation of streaks. Slight polydispersity in the suspension will not affect the formation of streaks; however, it has been shown that streaks are suppressed in binary suspensions having a particle size ratio larger than 10:1[20]. In addition, translating the substrate in an oscillatory manner[21] has also been shown to reduce the formation of streaks significantly. The amount of ink deposited in each experimental trial depended on the pressure applied to the felt tip. The diameter of the spot of ink deposited was varied over $1\text{ mm} \leq d \leq 6\text{mm}$ in a reproducible manner. It was observed that, only, $d \geq 2\text{mm}$ consistently generated a single streak, whereas, defects having a diameter of $d \approx$

1 mm had only roughly a 50% chance of forming a streak. A streak is identified via image analysis as a local region having more than seven particle layers located 4 mm from the edge of the defect. Once identified as a streak, the full width at half-maximum (*FWHM*) of the intensity of the streak, *w*, was calculated to quantify the width of the streak originating from each defect. As shown in Fig. 5.3, considering the standard deviation given by the error bars, the width of each streak generated from a defect is independent of the defect size.

[redacted]

Figure 5.3 Resulting streak width, *w*, as a function of the diameter *d* of the defect or seeded inhomogeneity, leading to the formation of a streak. Error bars indicate the standard deviation. The streak properties are largely independent of the conditions tested.[a]

---

[a] Reprinted with permission from [Boettcher J., Joy M., Joshi K., Muangnapoh T., and Gilchrist J.F. *Langmuir* **2015** 31(40) 10935-10938]. Copyright © American Chemical Society.

On the basis of this observation, a defect diameter of $d \approx 2$mm is used to maximize the number of defects which can be patterned on the sample and with a defect spacing as small as $L = 3$ mm. Far from the initiation of the streak, different dynamics can occur, including streak migration, merging, splitting, and decay; however, these streaks are often long-lasting, and the dynamics of the streaks are defined by the initial streaks formed, persisting over a large distance. Using these criteria, rows of defects having a prescribed spacing were used as initial conditions near the beginning of the deposition. The resulting number of streaks per defect is shown in Fig 5.4. In these samples, the distance between defects, L, alters the probability of a streak originating from a defect and of the formation of a spontaneous streak. In all of the data presented, while the spacing was set at millimeter increments of 3mm $\leq L \leq$ 10 mm, the length will be scaled by the capillary length of water, $\lambda_c = (\gamma/\rho g)^{1/2} = 2.7$ mm. For defect spacing $L/\lambda_c < 2$, streaks start at a defect and propagate in the direction of deposition; however, occasionally a defect does not seed the streak or the streak dissipates before the region where it is analyzed. In these situations, a short streak, similar to a wake of particles, may be apparent over a very short distance downstream of the defect and then dissipates. The width of streaks around the missing streak is moderately wider, suggesting the particles are possibly redistributed into neighboring streaks. Unsurprisingly, as defects are separated further, spontaneous streaks begin to arise between those initiated at the defects. This onset occurs for $L/\lambda c > 2.5$ (Fig. 5.4). For the largest spacing tested, $L = 10$ mm, additional streaks were not seen in any of the coatings. It should be noted that the entire width of the coating is approximately 25 mm. Thus the spacing between the edges and the streaks formed from defects is now roughly the same width as the defects. As mentioned previously, the edge effect always produces a streak due to the lateral inhomogeneity of the evaporation profile. [b]

---

[b] Streak margins is defined as two streaks propagate to combine into one single streak. A reverse effect can be observed, which is stated as splitting. The streaks sometimes terminate in progress of coatings too. With enough defect spacing, a merging of streaks can be avoided. With enough defect size, a termination of streak can be avoided

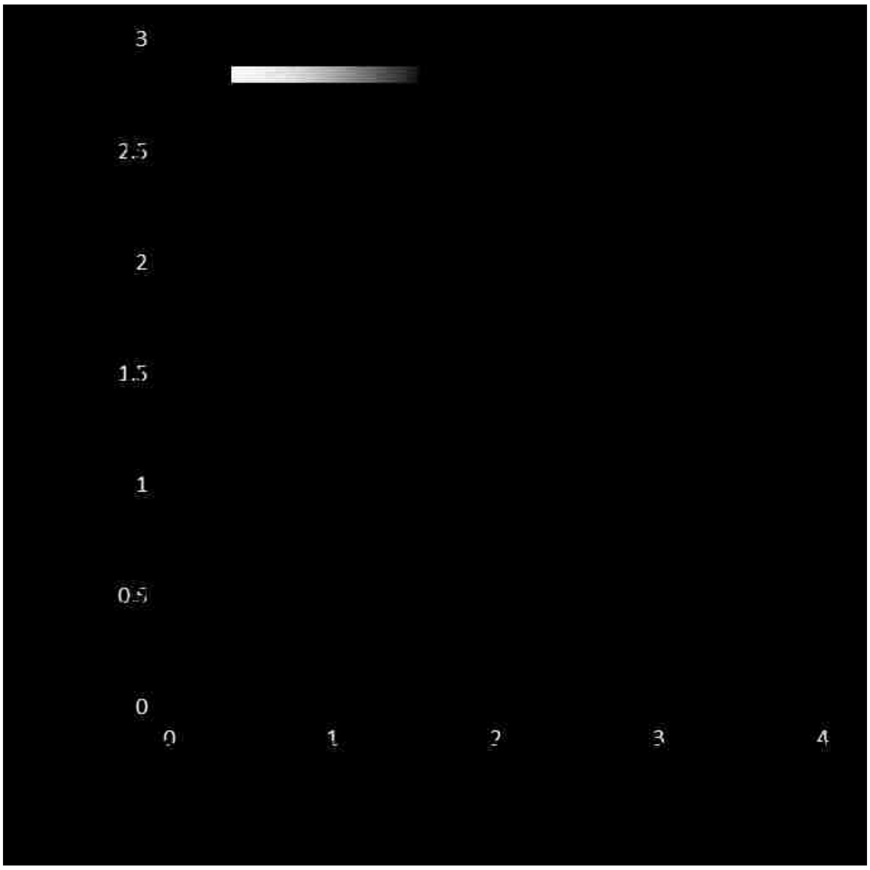

Figure 5.4 Number of streaks originated per initially seeded inhomogeneity as a function of the defect spacing. The intensity of each point corresponds to the probability of getting that many streaks for a particular defect spacing. With smaller spacing, occasionally defects form streaks that dissipate over a short distance while for larger streak spacing spontaneous streaks form between those originated from the local inhomogeneity.[c]

---

[c] Reprinted with permission from [Boettcher J., Joy M., Joshi K., Muangnapoh T., and Gilchrist J.F. *Langmuir* **2015** 31(40) 10935-10938]. Copyright © American Chemical Society.

The actual spacing between streaks, λ, is shown in Fig. 5.5. The imposed length scale, L, and the natural length scale, λc, should generally describe the spacing between streaks. The average spacing between streaks in patterned free substrates having no imposed defects is $\lambda/\lambda c = \lambda^* = 0.78$, as indicated by the dashed line and the gray bar indicating the standard deviation of this spacing. Since a large number of streaks are indeed produced from the defects, a strong 1:1 linear trend of streak spacing to defect spacing results for many neighboring streaks. In addition to seeded streaks, several streaks occur spontaneously in the fabricated samples, the nucleation of which does not follow a definite pattern. These spontaneous or unseeded streaks are observed to have a spacing greater than that formed on pattern free substrates. For the most part, unseeded streaks on patterned substrates form only when L is greater than twice this natural spacing. This trend holds for $2.5 < L/\lambda c < 3.5$ and breaks down for defect spacing where interference occurs from the edges of the samples. It is expected that in scaling up the width of these coatings, a general trend exists for spontaneous streaks having a spacing of no less than $\lambda < \lambda^*$ and the inhibition of steak formation occurring only roughly over an imposed defect spacing of $\lambda \approx 2\lambda^*$. This defines a maximum density of streaks that will form on a substrate that is patterned and also defines the maximum distance by which defects can be spaced while having confidence that spontaneous streaks will not form in the regions between the seeded streaks.

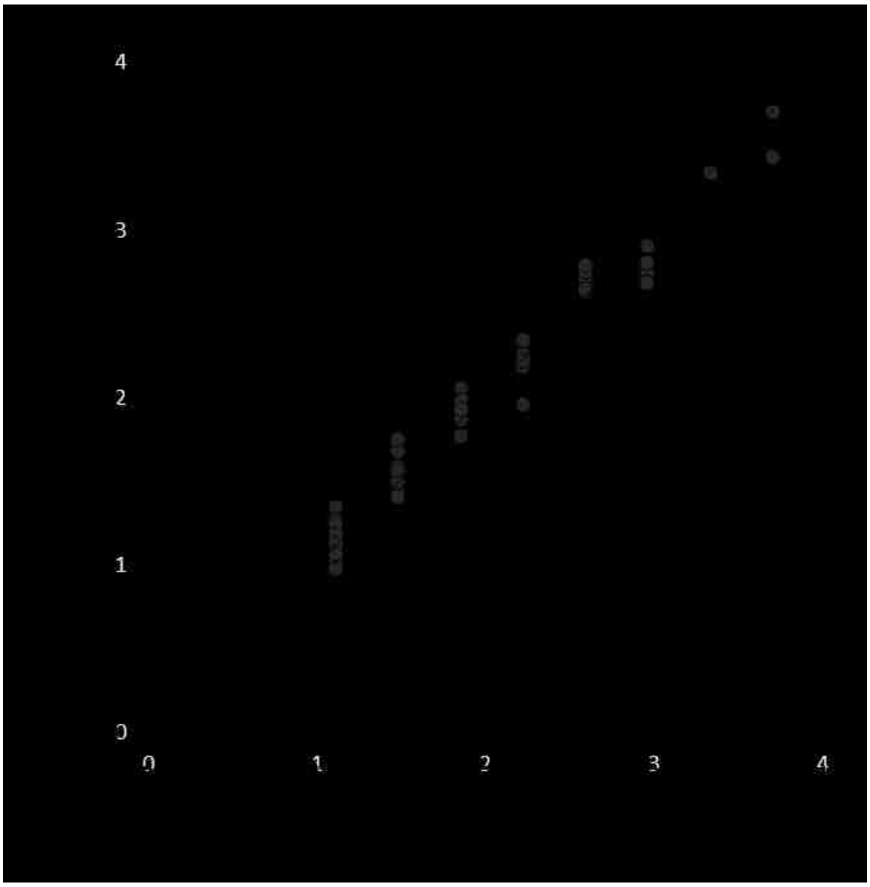

Figure 5.5 Peak-to-peak spacing of streaks as a function of defect spacing, calculated for seeded as well as spontaneous streaks. In samples without seeds, the spacing λ^* and its standard deviation for streaks that form spontaneously are shown by the dotted line and the width of the gray line, respectively. A linear trend was observed (slope = 1.02, R^2 = 0.97) for seeded streaks, as indicated by the solid line. For the spontaneously formed streaks, the spacing in those samples is lower than the trend in seeded streaks but on average is well above the natural spacing of streaks in unseeded samples.[d]

---

[d] Reprinted with permission from [Boettcher J., Joy M., Joshi K., Muangnapoh T., and Gilchrist J.F. *Langmuir* **2015** 31(40) 10935-10938]. Copyright © American Chemical Society.

5.5. Surfactant induced streaks

In chapter 3 we studied the effect of surfactant on thin film profile. At a higher concentration, surfactant induced marangoni flow improves the assembly. But adverse effect is observed below 0.1% w/w SDS concentration. In this region the marangoni flow is negligible as studied earlier. Following is the overall phase diagram obtained at different SDS concentration (Fig. 5.6).

We studied effect of surfactant on streaks formation. Fig. 5.7 shows the percentage of streaks in sample as function of surfactant at different substrate velocities. At very low concentration of SDS (0.0001%-0.001% w/w) there is not much effect in final assembly. The number of streaks and fractional coverage remains same as that of without surfactant. The adverse effect of addition of surfactant was observed in higher concentration range (0.01%-0.1% w/w), although as shown in chapter 3, above $\xi=0.1$, the substantial changes were observed in final assembly. The samples are practically streaks free and macroscopically very uniform.

The streaks decreases with increasing deposition speed, this phenomenon is well studied by Alex weldon[3], for all concentrations of SDS (Fig. 5.7) this general characteristic is observed.

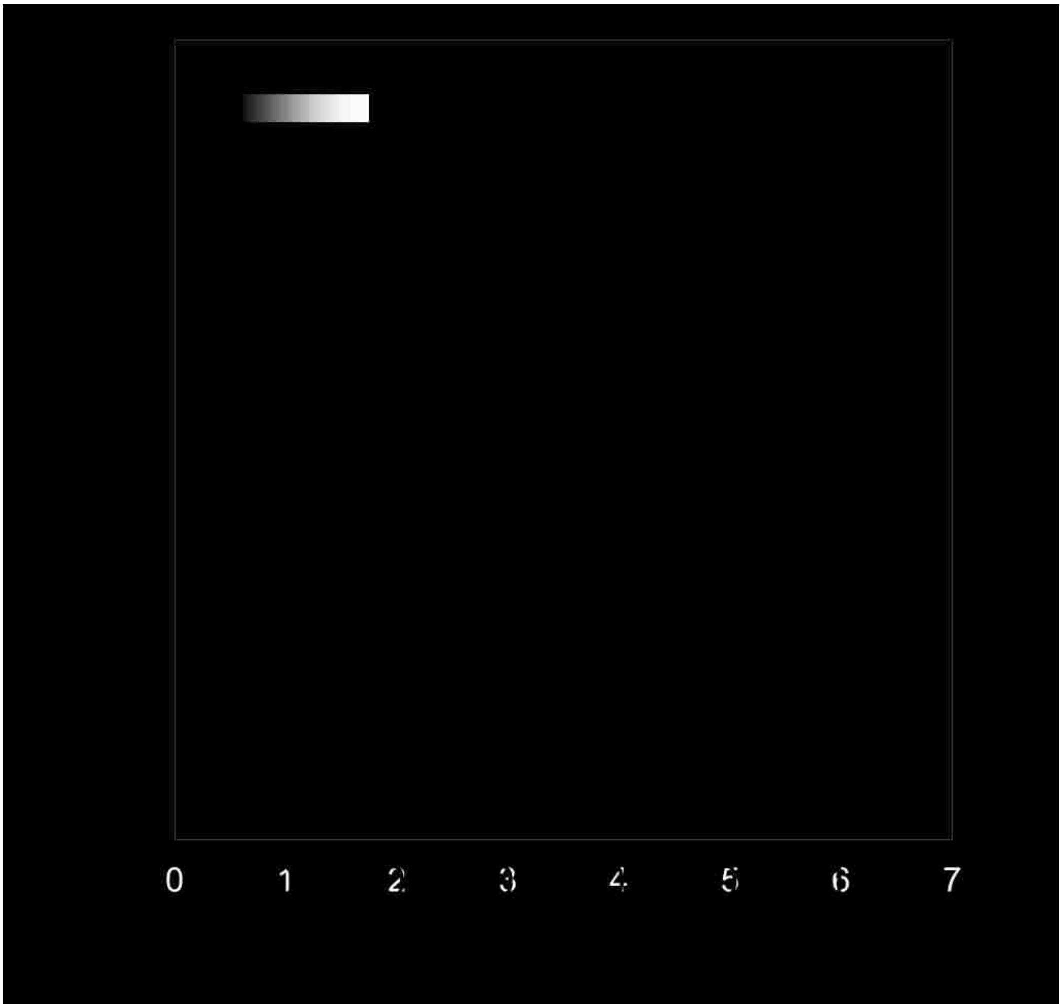

Figure 5.6. Phase diagram giving coating morphology as a function of substrate velocity and surfactant (SDS) concentration. Cross represent submonolayer dark triangles represent monlayer and circles represent multilayer. Straking in multilalayer can be approximated by gray scale, where straking increases with SDS concentration as well as decrease in substrate velocity. Marangoni effect dominates over CMC concentration.[e]

---

[e] The streak percentage is measured as given in chapter 3. The Streaks are defined as a coating region with 7+ particle layers. This corresponds to > 163 intensity.

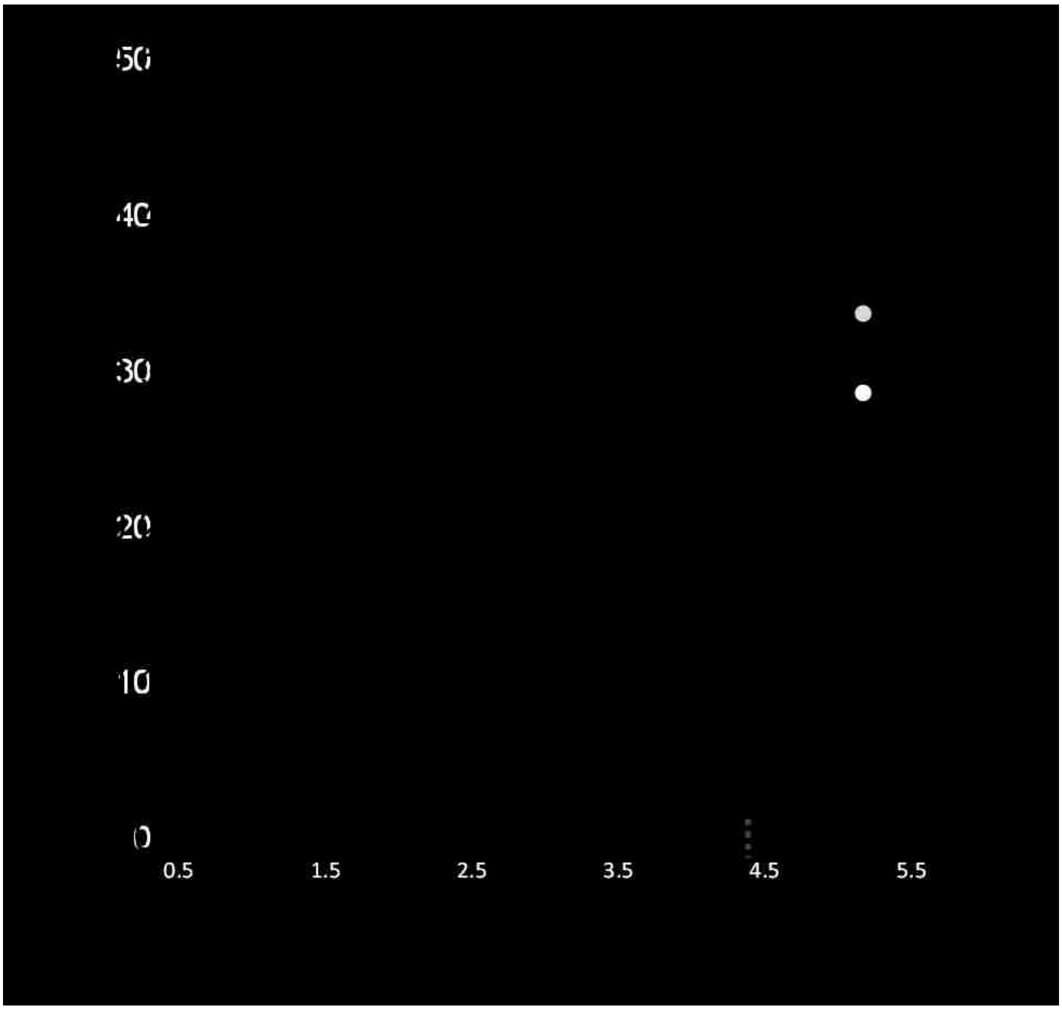

Figure 5.7 Graph showing fraction of samples covered with streak as a function of surfactant (SDS) concentration at various deposition speeds.
(●) 25μm/s, (●) 33μm/s, (○) 42μm/s, (○) 50μm/s.

With increase in SDS concentration (0.001%-0.1% w/w) more streaks are observed. There are two hypothesis which could explain these observations. The obvious fact is decrease in surface tension from the control bulk suspension, this effcet is neglesible at very low SDS concentrations (0.0001%). Decrease in surface tention can decrease the inherent Ray-lehigh Plateau instability wavelength[22]. Although the actual mechanism of streaks formation is not yet well known. Additionally, the streaks obsrved in samples are independent of surface tension. They occre at random locations and no clear trend with concentration. Generally instabilities have certain characteristic wavelength.The another hypothesis is the deposites of SDS on clean glass surface while assembly can serve as nucleate for streaks. Such deposites are rare in very small SDS concentrations thus not affecting streaks in generel, in first part we have showed how the streaks can spontaneouly grow on small hydrophobic surface impurities. Fig. 5.8 shows images obtained with confocal microscopy. SDS deosits were obsrved at birth of streaks, some of them are grown in bigger streaks, while others terminate in small distance.[f]

---

[f] The SDS deposits do not serve as nucleates at ξ=1, due to continuous depinning of the contact line caused by rigorous marangoni recirculation.

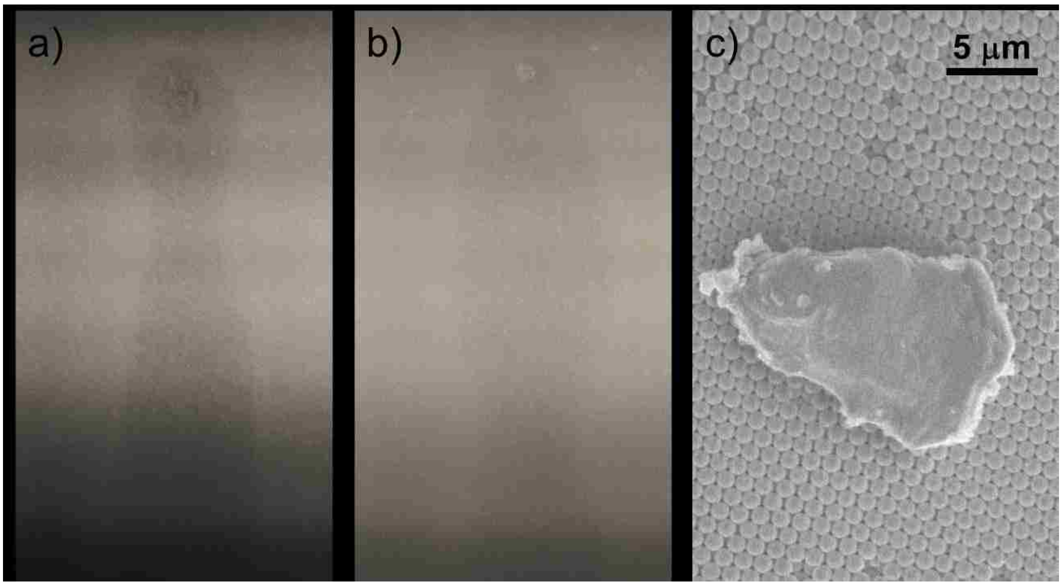

Figure 5.8 a, b) streaks nucleating from SDS deposits. **c)** SDS depoits observed under scanning electron microscope.

5.6. Conclusion

Although the mechanism for spontaneous streak formation remains unknown, this work shows how seeding defects can be used to direct the location of defect-free regions. Seeded streaks impart lateral flows that may suppress the instabilities that cause spontaneous streaks. This suggests that imparting flow in the direction transverse to deposition may alter how spontaneous streaks are initiated. Likewise, while the length scales involved may not seem significant since they are still confined to that on the order of the capillary length scale, relatively low-cost coatings atop microelectronic devices such as LEDs and other high-value optical components can be designed in such a way that optimum coatings will occur over a critical region without the formation of streaks in unwanted areas. This approach can be used to design the spacing of on-chip components to ensure maximum coating reproducibility. Streaks occurring over masked regions may even be easily removed using lithography, allowing recycling of the particles that formed unwanted streaks. Likewise, potential applications that find utility in streaks as porous media can be designed with known location and spacing.

References

(1) Darhuber, A. a.; Troian, S. M. Marangoni Driven Structures in Thin Film Flows. *Phys. Fluids* **2003**, *15* (9), S9.

(2) Xu, X.; Luo, J. Marangoni Flow in an Evaporating Water Droplet. *Appl. Phys. Lett.* **2007**, *91* (12), 2005–2008.

(3) Weldon, A. L. Investigations into Convective Deposition from Fundamental and Application-Driven Perspectives Investigations into Convective Deposition from Fundamental and Application-Driven Perspectives by, Lehigh University.

(4) Kumnorkaew, P.; Weldon, A. L.; Gilchrist, J. F. Matching Constituent Fluxes for Convective Deposition of Binary Suspensions. *Langmuir* **2010**, *26* (4), 2401–2405.

(5) Gilchrist, J. F.; Chan, A. T.; Weeks, E. R.; Lewis, J. a. Phase Behavior and 3D Structure of Strongly Attractive Microsphere-Nanoparticle Mixtures. *Langmuir* **2005**, *21* (24), 11040–11047.

(6) Muangnapoh, T.; Weldon, A. L.; Gilchrist, J. F. Enhanced Colloidal Monolayer Assembly via Vibration-Assisted Convective Deposition. *Appl. Phys. Lett.* **2013**, *103* (18), 2011–2015.

(7) Darhuber, A. A.; Troian, S. M. Marangoni Driven Structures in Thin Film Flows. *Phys. Fluids* **2003**, *15* (9), S9.

(8) Xu, X.; Luo, J. Marangoni Flow in an Evaporating Water Droplet. *Appl. Phys. Lett.* **2007**, *91* (12).

(9) Brewer, D. D.; Allen, J.; Miller, M. R.; Santos, J. M. De; Kumar, S.; Norris, D. J.; Tsapatsis, M.; Scriven, L. E. Mechanistic Principles of Colloidal Crystal Growth by Evaporation-Induced Convective Steering. *Langmuir* **2008**, *24* (23), 13683–13693.

(10) Cazabat, a. M.; Heslot, F.; Troian, S. M.; Carles, P. Fingering Instability of Thin Spreading Films Driven by Temperature Gradients. *Nature* **1990**, *346* (6287),

824–826.

(11) Troian, S. M.; Herbolzheimer, E.; Safran, S. a; Joanny, J. F. Fingering Instabilities of Driven Spreading Films. *Europhys. Lett.* **2007**, *10* (1), 25–30.

(12) Harris, D. J.; Hu, H.; Conrad, J. C.; Lewis, J. a. Patterning Colloidal Films via Evaporative Lithography. *Phys. Rev. Lett.* **2007**, *98* (14), 1–4.

(13) Routh, F.; Russel, W. B. Horizontal Drying Fronts during Solvent Evaporation from Latex Films. *Aiche J.* **1998**, *44* (9), 2088–2098.

(14) Born, P.; Munoz, A.; Cavelius, C.; Kraus, T. Crystallization Mechanisms in Convective Particle Assembly. *Langmuir* **2012**, *28* (22), 8300–8308.

(15) Fleck, N. A.; McMeeking, R. M.; Kraus, T. Convective Assembly of a Particle Monolayer. *Langmuir* **2015**, *31* (51), 13655–13663.

(16) Ozin, G. a.; Yang, S. M. The Race for the Photonic Chip: Colloidal Crystal Assembly in Silicon Wafers. *Adv. Funtional Mater.* **2001**, *11* (2), 95–104.

(17) Vlasov, Y. a; Bo, X. Z.; Sturm, J. C.; Norris, D. J. On-Chip Natural Assembly of Silicon Photonic Bandgap Crystals. *Nature* **2001**, *414* (6861), 289–293.

(18) Dimitrov, A. S.; Nagayama, K. Continuous Convective Assembling of Fine Particles into Two-Dimensional Arrays on Solid Surfaces. *Langmuir* **1996**, *12* (5), 1303–1311.

(19) Prevo, B. G.; Velev, O. D. Controlled, Rapid Deposition of Structured Coatings from Micro- and Nanoparticle Suspensions. *Langmuir* **2004**, *20* (6), 2099–2107.

(20) Kumnorkaew, P.; Gilchrist, J. F. Effect of Nanoparticle Concentration on the Convective Deposition of Binary Suspensions. *Langmuir* **2009**, *25* (11), 6070–6075.

(21) Kumnorkaew, P.; Ee, Y. K.; Tansu, N.; Gilchrist, J. F. Investigation of the Deposition of Microsphere Monolayers for Fabrication of Microlens Arrays. *Langmuir* **2008**, *24* (21), 12150–12157.

(22) Johnson, M.; Kamm, R. D.; Ho, L. W.; Shapiro, A.; Pedley, T. J. The Nonlinear Growth of Surface-Tension-Driven Instabilities of a Thin Annular Film. *J. Fluid Mech.* **1991**, *233*, 141–156.

CHAPTER 6

Correlation of particle crystallinity in ALB deposition

6.1. Introduction

The colloidal particle assembly is making a great impact in a field of modern technology such as photonics[1–6], lithography[4,7,8], ceramics[7], sensors[9–13], solar cells[14], membranes[15–19], cell capture devices[20]. There are different established small scale methods to fabricate the colloidal crystals such as spin coating[21,22], gravity settling[23], and convective deposition[24–26], Langmuir-Blodgett deposition[27,28]. The main challenge all these methods face, is limited scalability and cost control.

Automated Langmuir-Blodgett deposition, a continuous version of traditional Langmuir-Blodgett deposition that uses a flowing liquid sub-phase, was first introduced by researchers at the University of Toronto[29]. This process enables roll-to-roll assembled particle deposition, (Fig. 6.1) where the particle assembly is formed at an air-liquid interface which is pushed towards moving the web, or substrate, with the help of an underlying recirculation of liquid (Fig. 6.1). Web velocities are of the order of 1-10mm/s, and particles deposited on the web is characterized by the Landau-Levich deposition. Both sub-processes of ALB with regard to particle assembly and particle deposition have been separately studied rigorously by many researchers[30–38].

ALB apparatus is designed for achieving faster as well as large area coatings. Previous work gives preliminary data obtained by ALB with regard to using mass balances to understand the coating rate limitations and formation of various macroscopic coating morphologies.[39]. What is desired from nanomanufacturing processes is the ability to tune the process conditions to alter the microstructure. The primary goal of this research is to provide an adequate knowledge about ALB parameters with regard to the deposited microstructure. We first present the microstructure quality obtained by changing basic operating parameters, including web speed and suspension concentration and delivery rate. An ideal process can independently tune the rate of deposition and the microstructure quality. In practice, this is essentially impossible. However, through exploration of altering the suspension properties, in this case specifically by the addition of nanoparticles to the solution analogous to previous studies, some enhancement of microsphere crystallinity can be obtained.

As discussed above, the overall process consists of particle assembly on the liquid interface and particle removal by a moving web. The suspension is injected onto the Langmuir trough using the syringe attached to a linear motor. The tip of the syringe is mounted gently onto the interface. This helps in maintaining a constant volumetric flow rate ($\dot{V}$) of the suspension. The Langmuir trough is filled with a carrier liquid (water in this case). A particular recirculation rate (R ml/min) is maintained to push particles towards the web. The recirculation is achieved by pumping the water as shown in Fig. 6.1. The recirculation rates are small to avoid the turbulent flow. Suspension spreads on the water quickly due to the marangoni effect. Ethanol evaporates quickly trapping particles at the interface. Particles interact with each other on and form the close-packed structure. The recirculation guides the assembly towards the drain, where it is picked up by moving the substrate.

The interactions between particles and particle-substrate affect the coating structure in most cases. Previous work shows the assembly of many different types of particles[35,40–43] and carrier liquids[31,43] and the role of these interactions in the quality of interfacial particle assembly. Also, the substrate interactions can play a crucial role in second part of process[44]. Here we are focusing on an ideal yet prototypical system of coating silica microspheres (~1μm) suspended in ethanol as was used previously[39]. Water is the carrier liquid in all experiments. Although an improvement in microstructure can be made by changing particle properties such as surface chemistry or modifying solvent and carrier liquid properties, this goal is broader than the scope of this article to first measure and demonstrate the crystallinity of the deposited particle layer.

The relationship between web velocity and particle inlet can be derived by simple mass balance[39]. The particle balance for a monolayer on a continuously rolling web at the velocity, U_W *(mm/s*) and a suspension delivery rate ($\dot{V}$ *mm^3/s*) (equation 1).

$$\frac{\theta U_W W}{\pi a^2} = \frac{\phi_\mu \dot{V}}{\left(4\pi a^3 \big/ 3\right)} \tag{1}$$

Where U_W is web velocity, a = 432±10nm is particle radius, θ is fractional particle coverage, θ = area covered by particles/ coating area. The maximum value of θ for the hexagonal structure can be ~ 0.9. W is the width of the web, $\dot{V}$ is the suspension flow rate, ϕ_μ is the volume fraction of microspheres in the solution. There is always some particle loss to the underlying carrier fluid while particles are being deposited. This is accounted with a fitting parameter β, so (1) can be written as following.

$$U_W = \left(\frac{3}{4aW}\right)\frac{\beta\phi_\mu \dot{V}}{\theta} \tag{2a}$$

This equation depends upon both particle volume fraction as well as suspension flow rate. These parameters can be combined and (2a) can also be written in terms of particle mass flow rate, M (*mg/min*). $M = \rho_p \phi_\mu \dot{V}$

$$U_W = \left(\frac{3}{4aW}\right)\frac{\beta M}{\theta\rho_p} \tag{2b}$$

U_W corresponds to ideal monolayer condition, which is sensitive to mass flow rate. Slower substrate velocities, $U<U_W$, result in a multilayer coating, and discontinuous or only partial substrate coverage is observed when $U > U_W$ (Fig. 6.2).

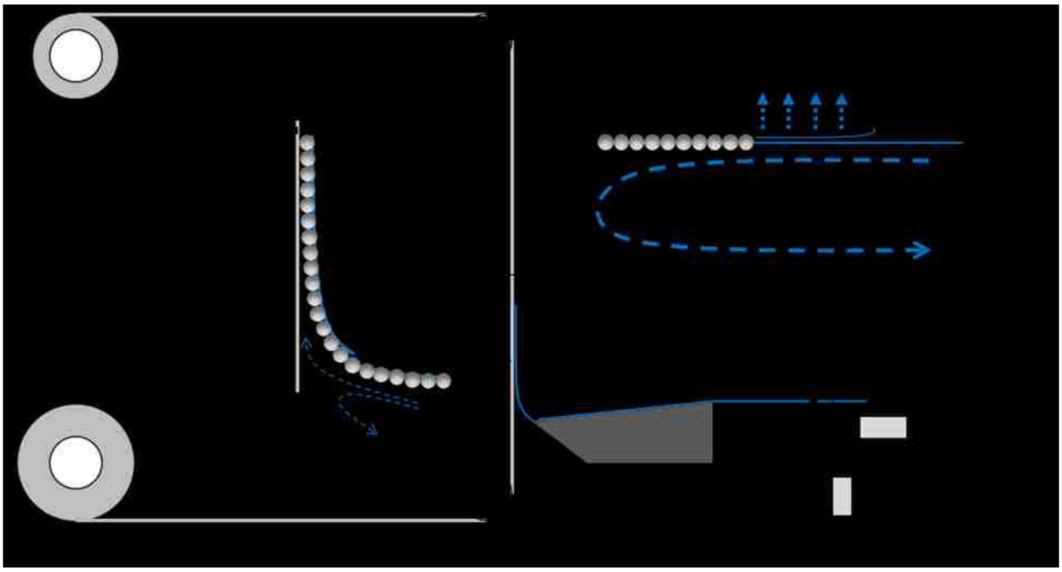

Figure 6.1 general set up for ALB coating, on the right we have Langmuir trough where the (EtOH+SiO_2) suspension is injected which spreads on water and particles configure an assembly on Air-Water Interface. Due to marangoni spreading and recirculation, the suspension spreads and move towards the web, as ethanol evaporates particles get trapped at Air-Water Interface. Particles attract each other as a result of capillary forces which leads to particle assembly, which is transferred onto moving substrate. On the left, the substrate is rolling continuously (substrate velocities are the order of mm/s), which makes Landau-Levich type coatings where coating thickness is governed by the balance between capillary and viscous forces.

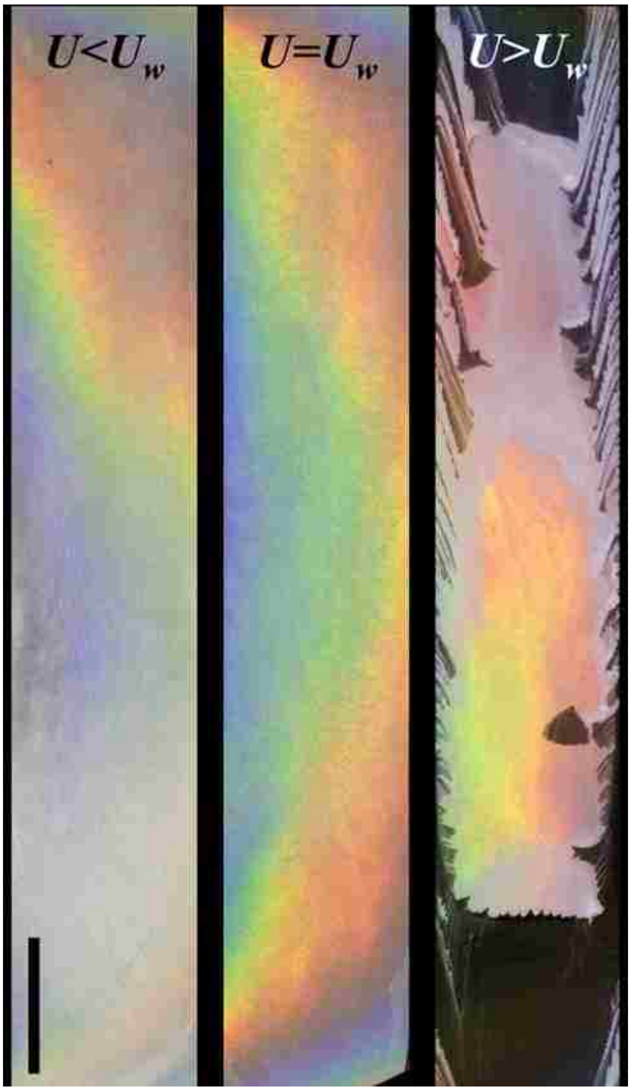

Figure 6.2 light scattering from different sample morphologies obtained with increasing substrate velocity, from left to right multilayer, monolayer and discontinuous. Scale bar corresponds to 5cm.

6.2. Materials and methods

6.2.1. *Suspension preparation*

The colloid suspension used in this study is prepared by dispersing the silica microsphere (SiO_2, Fiber Optic Center Inc. MA, USA) in pure ethanol (Decon, PA USA, 200 proof) with the volume fraction varying from 0.03 to 0.15. The SiO_2 microsphere are of density 1.8g/cm3, the average diameter of 865±20 nm. In order to get a well-dispersed SiO_2 suspension 15 min ultrasonic (Fisher Scientific FS20D) treatment was employed.

SiO_2 nano particles are prepared by the Stöber process[45], with an average diameter~100nm. There was some dispersity in the size (±10 nm). The nanoparticles were made fluorescent using a dye (rhodamine B).

Then, the SiO_2 suspension was loaded to a syringe for the consequent injection procedure. In all the experiments, distilled water (Crystal Spring Waters Co.) is used as the carrier fluid. The SiO_2 particles were dispersed in ethanol before adding to the syringe.

6.2.2. *Particles at the air-water interface*

Particles at the liquid-air interface are stable with a high Gibbs free energy. Slight hydrophobic particle can be highly stable at the air-water interface. The detachment Gibbs free energy from an interface to a particular phase is given by the Koretsky and Kruglyakov equation[30,46]

$$\Delta G_d = \pi a^2 \gamma_{aw} \left(1 - |\cos\theta|\right)^2 \tag{3}$$

Here, a: is the particle radius, γ_{aw}: is the air-water surface tension, $\cos\theta$: is the contact angle with air/water phase. This detachment energy is several order magnitude the thermal energy (K_bT) and is enough to stabilize even 100nm silica particles[46,47] with minimal contact angle (θ<10^o).

The Interactions between particles at liquid interface are very complicated[32,34,42,48]. For a large particle (>>1μm), interactions are dominated by the weight of particle. A large particle deforms the liquid meniscus, which results in an attractive interactions[49]. In case of smaller size particle, the interface deformation occurs due to the presence of surface charge on particles[34,42]. For a charge free particle solvated ions and dipole interactions can result in repulsion[41,49].

In the following work we have used the ethanol suspension to spread particles on the water surface. Solvents like methanol and ethanol are highly studied to carry out such Langmuir-Blodgett (LB) monolayers[43,50,51]. Silica particles in ethanol carry a negative charge with a zeta potential~20mV[51]. Thus particles experience the capillary attraction due to the deformed interface by the imbalance electric field[42,49] as shown in the Fig. 6.3.

The previous work show that the hydrophobic particles form a better monolayer on the water interface[43]. Also for a close packed structure the surface charge plays an important role[42]. The surface potential is directly related to attractive force. Also the extreme hydrophobicity will increase the deformation thus exposing more surface. Previous work is done on a very small scale, approximately mm^2 area. The main interest here although, is to focus on the fast and large scale particle assembly.

6.2.3. Film deposition

A common PVC (Graphics Plastics, OH USA) substrate was used for the coating purposes. The substrate roll was mounted as shown in Fig 6.1. With the help plastic rolls the substrate is guided and continuously rolled using a motor. The produced particle assembly on the water interface is moved towards the web by recirculating the underneath liquid as shown in Fig. 6.1. The particle assembly is then carried out using the moving web by Landau-Levich type deposition as shown in the Fig. 6.1. External heater is used to dry out the deposited particle region before it gets rolled. Only the middle part of the substrate is getting coated (Substrate width is~15 cm and coating width 10cm) to avoid any edge effects.

6.2.4. Characterization of microstructure

The deposited monolayers of microspheres are observed directly using the confocal laser scanning microscopy after rewetting the layer with an aqueous solution of 8 mM Rhodamine B. The image analysis is done using IDL, POV and ImageJ to calculate the ρ and Ψ_6. Where ρ is the particle coverage and Ψ_6 is the local bond order. For more details look our previous work[44].

The nanoparticles were observed under the Scanning Electron Microscope. Additionally nanoparticles distribution was mapped using the confocal microscope without using a dye. Since only nanoparticles are florescent they can be mapped without using external dye.

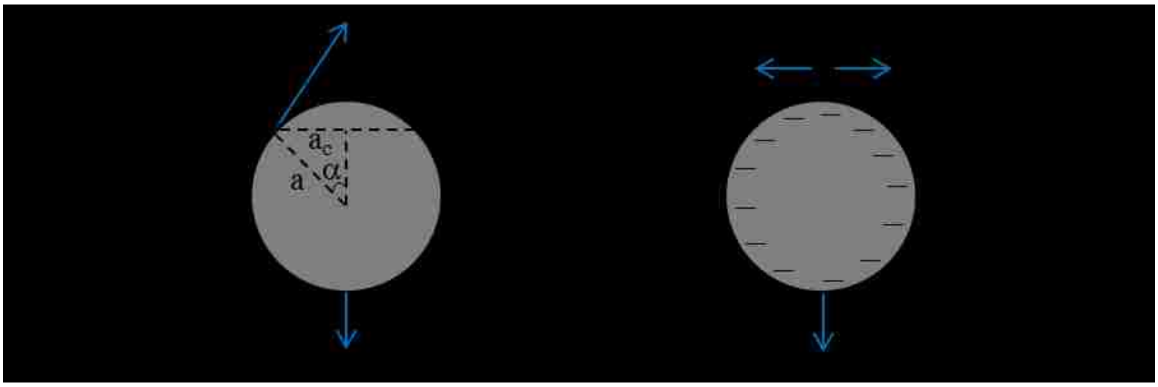

Figure 6.3 interactions between two negatively charged silica spheres at the air-water interface. The imbalance between electric field F_{ED} deforms the interface, which results in the capillary attraction (F_{EC}) and electric repulsion (F_{ER}).

6.3. Results and Discussion

6.3.1. *Effect of mass flow rate (M) on quality of monolayer*

From the Eq. (2) we know that web velocity is proportional to the mass flow rate, $U_W \sim \phi_\mu V$ or rather $U_W \sim M$. Here we have systematically analyzed the quality of the crystal structure obtained at different mass flow rate as shown in Fig 6.4. Fig 6.4a shows that a linear relationship between the U_W and M is valid at lower mass flow rates, but deviates at higher values of M. The fitting parameter ε corresponds to a fraction of particles successfully ended in the interfacial crystal structure. It decreases with increasing suspension input M. One simple reason could be the spreading of suspension on the interface happens because of the marangoni flow[46]. At constant ethanol evaporation, the increasing mass flow rate can lead to suppression of the marangoni flow. This would result in decreasing the value of ε. To find the ideal monolayer condition, experiments were done at different web velocities keeping constant suspension input (V). Same procedure is applied for the different volume fraction (ϕ_μ) suspensions. Samples obtained only from ideal web velocity were analyzed to determine the local bond order Ψ_6 and the particle coverage ρ. As shown in Fig 6.4b and 6.4c respectively. The Ψ_6 and ρ values decrease with increasing mass flow rate M. The significant increase in the Ψ_6 is an indication of improvement in the crystal structure. With a better packing more particles can be included under same area of coating, which also improves the ρ slightly.

The ALB consists of two simultaneous processes. Formation of particle assembly on the liquid air interface and transferring the assembly on top of the substrate. The final structure is mainly depend on first step, i.e. quality of assembly on the air-water interface. Thus, the final structure shows an improvement with prolonged time for assembly i.e. better structure was obtained with less number of particles coming together per unit time (Ψ_6 vs M).

For the higher web velocities, (generally $U_W > 10$mm/s) the liquid film thickness is balanced with gravity and viscous forces. The film thickness is more than the particle diameter. Thus Particles stay trapped at the air-water interface and not on the substrate. Here particles move with the interface velocity, which is less than the web velocity[39]. In this article all the experiments have done at web velocity sufficiently lower than 10mm/s.

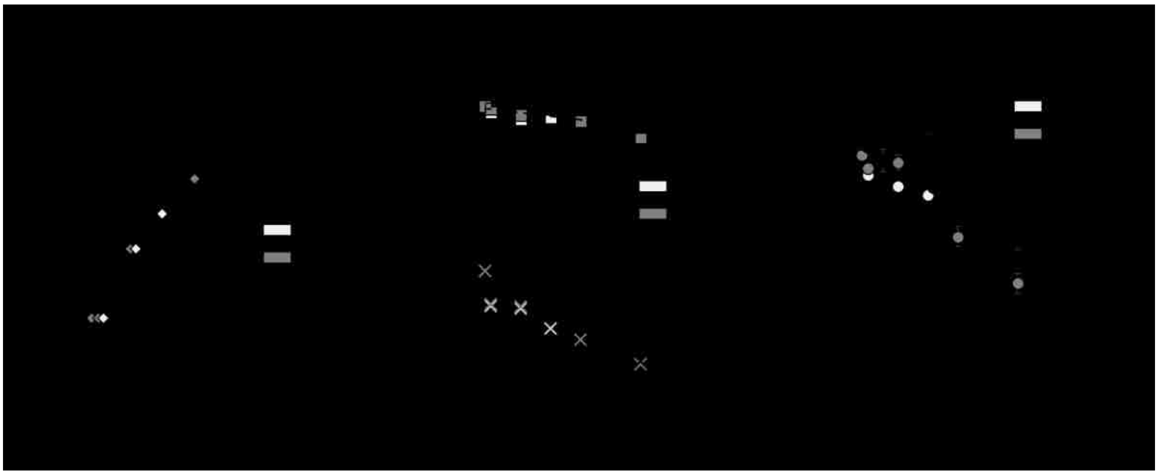

Figure 6.4 Colors represent volume fraction ϕ_μ of suspension, light gray: 0.05, gray: 0.1, black: 0.15, a) U_W as a function of M. Diamonds show the monolayer web velocity for corresponding mass flow rate. b) Crosses represent ρ value and squares represent ρ values for corresponding M, c) Circles represent Ψ_6 at different M.

These results show very critical trade-off between the coatings speed and coating quality. The rate of Particle deposition affects the coating quality. We were able to obtain high quality particle assembly at the web velocity U_W 1-3mm/s. But for a fact, even these velocities are much higher compared to the other particle assembly methods such as the convective deposition (10μm/s-100μm/s) or gravitational settling (100nm/s-1000nm/s). With a sufficiently large substrate width one could produce high quality coatings over several meter^2 in area within few minutes.

Fig. 6.5 shows representing images for microstructure obtained at different web velocity. The Ψ_6 in this particular image is approximately equal to the average Ψ_6 calculated over scanning ~10^6 particles. It is very clear from the microstructure that there is significant trade off in the quality as we make coating faster. All the images are for 15% ϕ_μ with increasing web velocity U_W. The grain size for lower velocities is much larger. Even though, lower velocities are order of magnitude faster than other particle assembly processes. This proves that we can potentially fabricate high quality crystals via ALB.

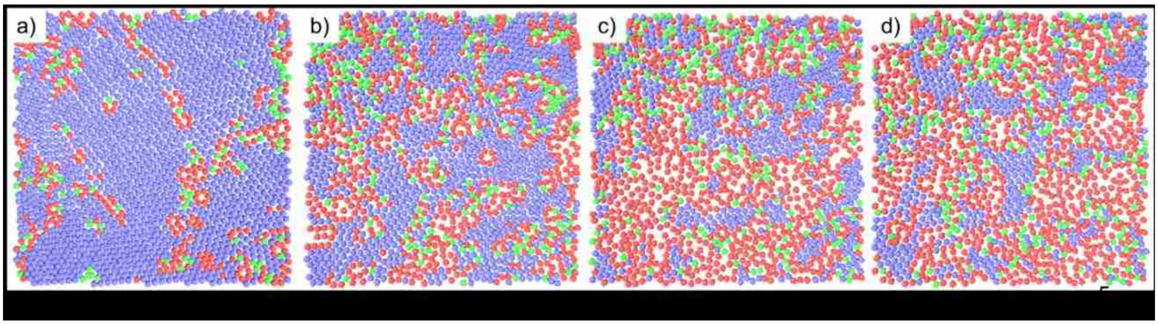

Figure 6.5 Single frames representing average microstructure as result of different web velocity. Blue circles represent particles with six neighbors and Ψ_6>0.7, green circles represent particles with six neighbors and Ψ_6<0.7, red circles represent particles without six neighbors. a) ϕ_μ=0.15, U_W=3 mm/s, b) ϕ_μ=0.15, U_W=4 mm/s, c) ϕ_μ=0.15, U_W=7 mm/s, d) ϕ_μ=0.15, U_W=8 mm/s.[a]

---

[a] Color images of microstructures are prepared in POV software using the actual coordinates of particles. Color code allows to discriminate particles with different surrounding structures.

6.3.2. Effect of recirculation

The liquid underneath the particle assembly is continuously recycled to give a directional velocity to the particle assembly. The Particle assembly moves in the direction of recirculation as shown in Fig. 6.1. Even if recirculation is small, recirculation velocity contributes to particle flux. Fig. 6.6 shows that the recirculation rate (R) does not affect the monolayer velocity as well as quality of coating significantly. Although, we have observed the critical recirculation rate, below which, uniform monolayer is hardly possible. We have observed the patches of discontinues multilayer below this critical recirculation rate.

This proves that the recirculation helps in maneuvering the assembly from the trough to the web without actually changing macrostructure. Interfacial velocity due to recirculation does not change surface pressure significantly. We believe, that a certain rate of the recirculation is only necessary to form a steady recirculation loop around the trough. Producing accurate flow profile inside the trough will require mathematical simulation because of the complex geometry of the trough. We have done experiments with changing a slope on trough and a position of suspension inlet, both trials show negligible change in the final structure and monolayer velocity.

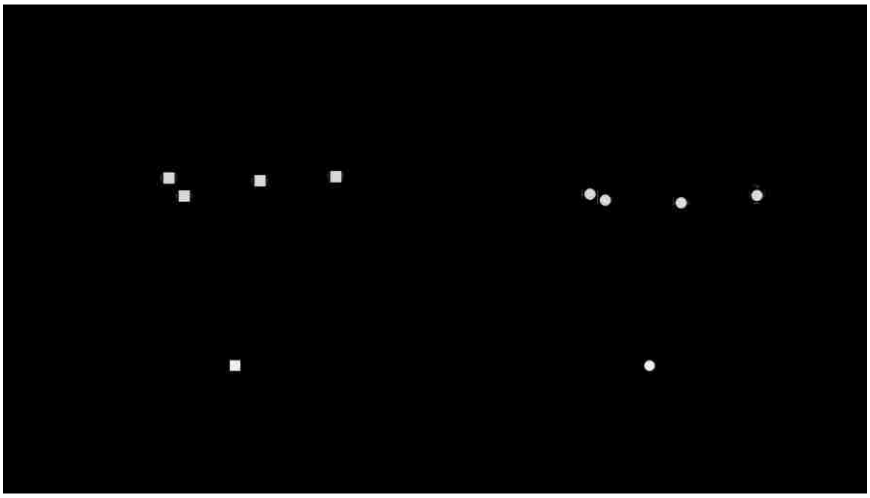

Figure 6.6 a) U_W as function of recirculation rate *R*. b) ρ as function of *R*, c) Ψ_6 as function of *R*. All experiments were done at ϕ_μ=0.05. The dotted line shows the critical recirculation rate below which monolayer is not observed. **Note**: The recirculation rate is controlled by flow meter. The small error bars in X axis are due to little fluctuations in flow.

6.3.3. Effect of addition of nanoparticles

Nanoparticles were added to the silica water suspension to make binary suspension of microspheres and nanospheres. Binary suspension has proven to be effective way of increasing the crystal quality[52]. Fig. 6.7 shows the increase in the crystal quality (Ψ_6) with the addition of nanoparticles. The Ψ_6 is analyzed with an increasing ratio of nanoparticles to micron size particles. This ratio is defined as r (Fig. 6.7).

All above experiments are done at the constant web velocity U_W =2mm/s with the different value of ϕ_μ. In the first part we showed that only lower web velocities can produce better coatings, although using the binary suspension with the proper particle ratio (r) we were able to improve the quality of coatings over control suspension. In Fig. 6.7 all the experiments are done with lower web velocity (2mm/s). Since the Ψ_6 is already good, there is not much increase in Ψ_6 with the addition of nanoparticles. Fig. 6.8 shows even small increase in the Ψ_6 can affect the grain size considerably. Fig. 6.8 represents microstructure at different values of r at ϕ_μ=0.03.

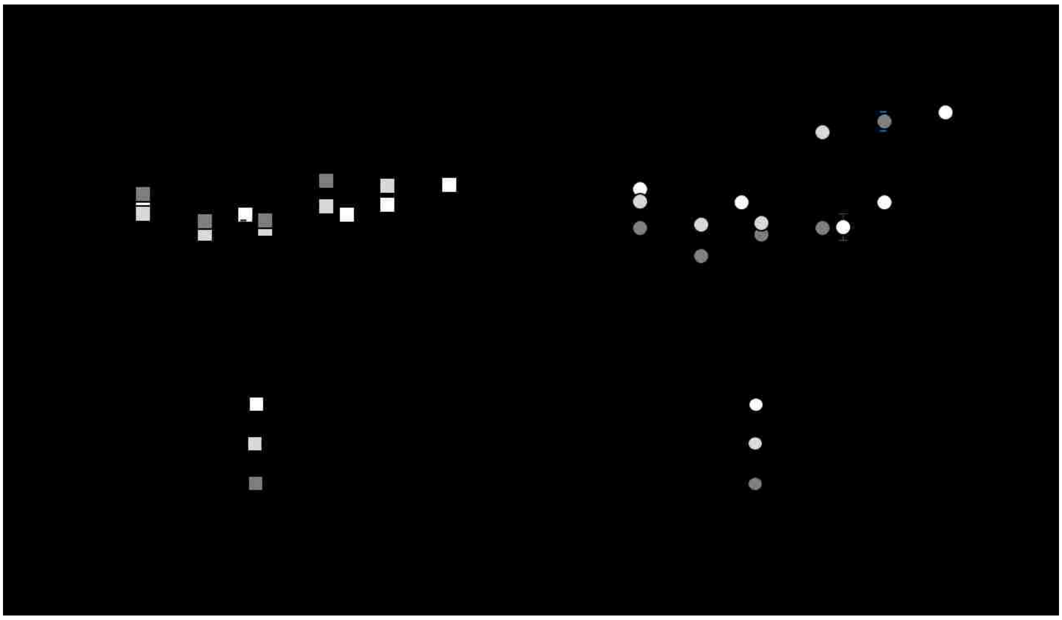

Figure 6.7 colors represent volume fraction of microspheres in suspension white, light gray, gray corresponds to ϕ_{μ}=0.03, 0.05, 0.1 respectively. a) θ vs r, b) Ψ_6 vs r.

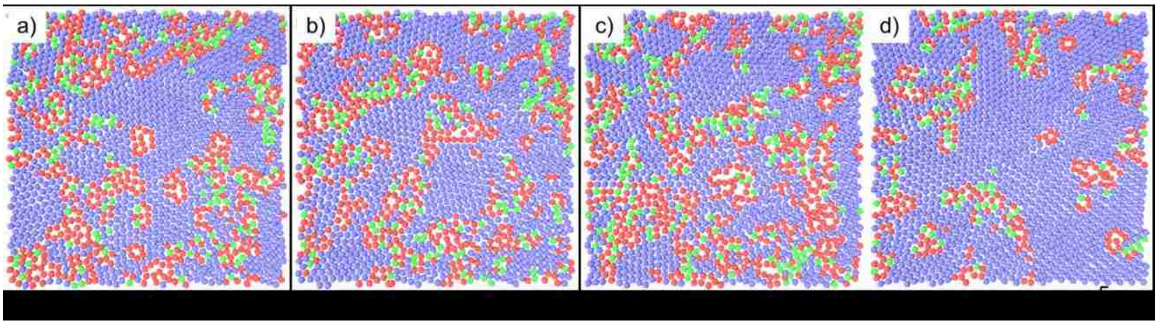

Figure 6.8 Single frame representing average microstructure as result of different nanoparticle concentration. Blue circles represent particles with six neighbors and Ψ_6>0.7, green circles represent particles with six neighbors and Ψ_6<0.7, red circles represent particles without six neighbors. ϕ_{μ}=0.03, U_W=2 mm/s a) r=0, b) r=108, c) r=216, d) r=324.

Additional thing to be noticed from Fig. 6.7 is that with an increasing value of r, the Ψ_6 stays same or rather decreases little, but it shoots up at certain r value. Also this critical value of r changes with ϕ_μ. Above experiments are done with the same web velocity at different volume fraction suspensions, so only ϕ_μ is variable.

In order to further understand the effect of nanoparticles, we did experiments with same ϕ_μ and different U_W. The effect is significant as the web velocity increases. As shown in Fig. 6.9 and Fig. 6.10. The Ψ_6 increases significantly for U_W=4mm/s and also U_W=6mm/s.

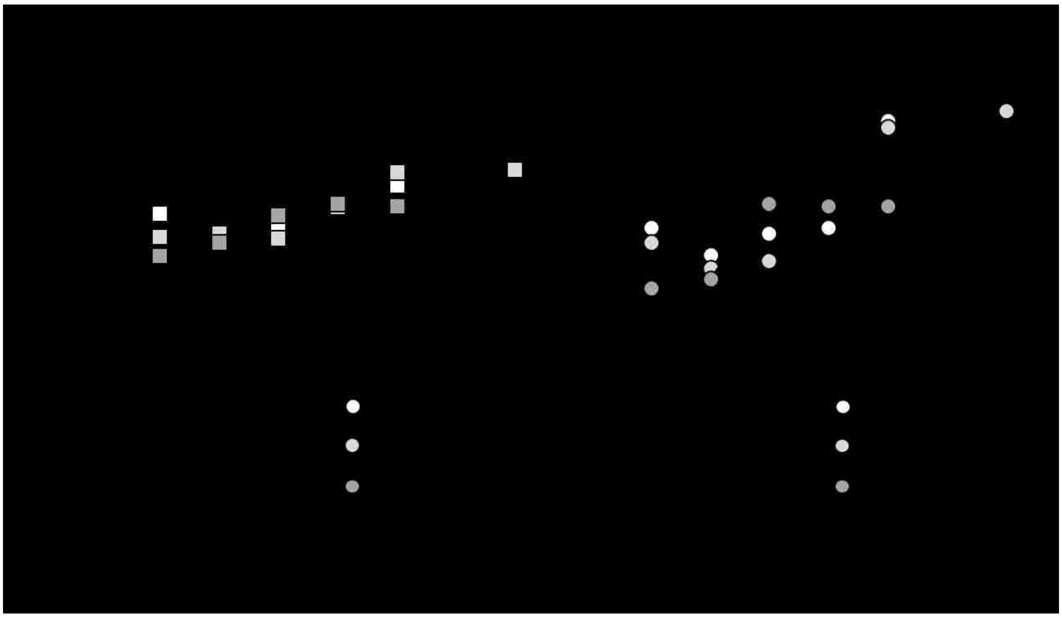

Figure 6.9 All the experiments were done at ϕ_μ=0.05. Colors represent different web velocities white, light gray, and gray corresponds to 2mm/s, 4mm/s, and 6mm/s respectively. a) ρ vs r, b) Ψ_6 vs r.

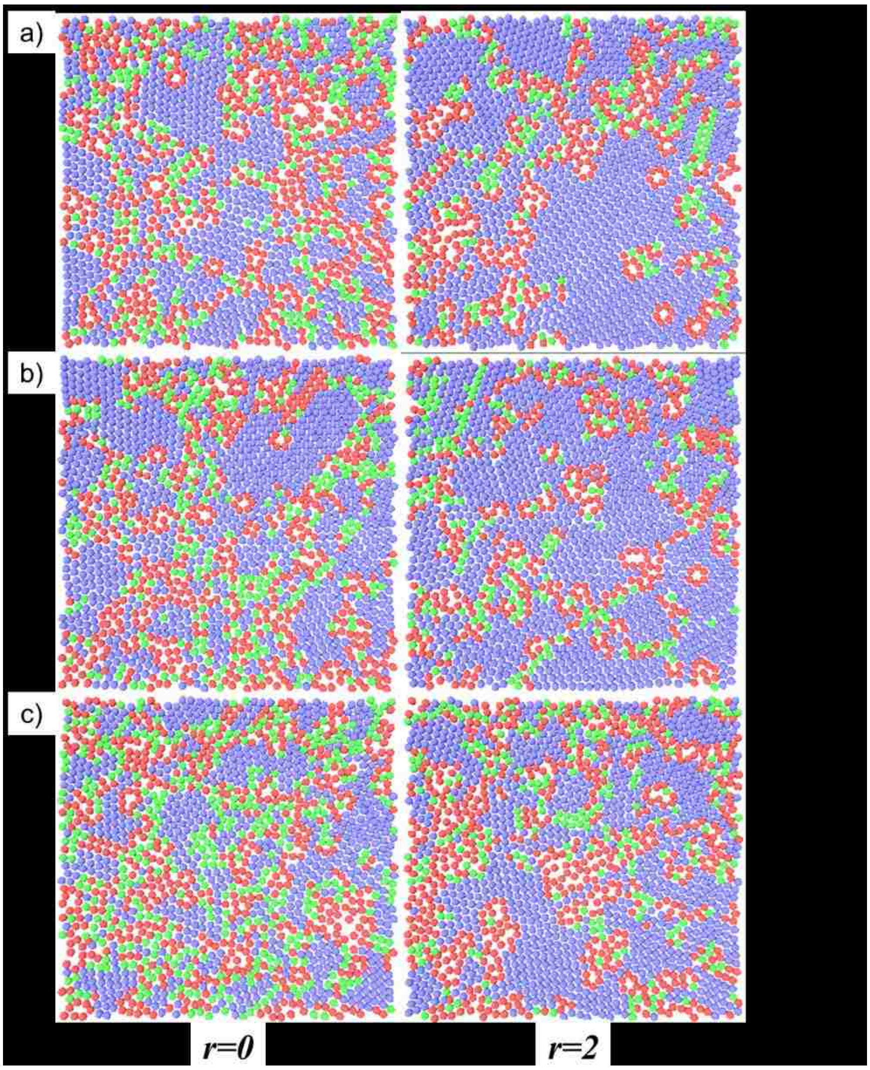

Figure 6.10 Single frames representing average microstructure as result of different nanoparticle concentration. Blue circles represent particles with six neighbors and Ψ_6>0.7, green circles represent particles with six neighbors and Ψ_6<0.7, red circles represent particles without six neighbors. ϕ_μ=0.05, a) U_W=2 mm/s r=0 (Ψ_6=0.70) and r=259 (Ψ_6=0.78), b) U_W=4 mm/s r=0 (Ψ_6=0.69) and r=259 (Ψ_6=0.78), c) U_W=6 mm/s r=0 (Ψ_6=0.66) and r=259 (Ψ_6=0.72). The gradient shows Ψ_6 increases with decreasing web velocity but increases after certain value of r.

6.3.4. Role of nanoparticles

Even though the presence of nanoparticle improves the structure quality, the mechanism is not very clear. Only a small fraction of nanoparticles were observed in final colloidal crystal as shown in Fig. 6.11b. One possibility is nanoparticles are not stable on the interface and they submerge into trough while particle assembly. Second possibility is they dragged together during drying process (Fig. 6.11c). Since they are loosely connected, drying stresses can break them apart.

Also, only the particular ratio of ϕ_ν/ϕ_μ produce higher quality crystal structure. And the high quality hexagonal packing is observed in areas of nanoparticles binding microparticles (Fig. 6.11b). These two facts lean towards second hypothesis. Although we do not have enough experimental evidence to conclude any of the hypothesis. Bidisperse suspension shows similar enhancement in monolayer quality in the case of convective deposition[53]. In the case of convective particle assembly the substrate velocities are much slower, which makes diffusion of nanoparticles a self-healing force in order to achieve uniform distribution. However, Peclet number are much higher in the case of ALB deposition, even for the nanoparticles.

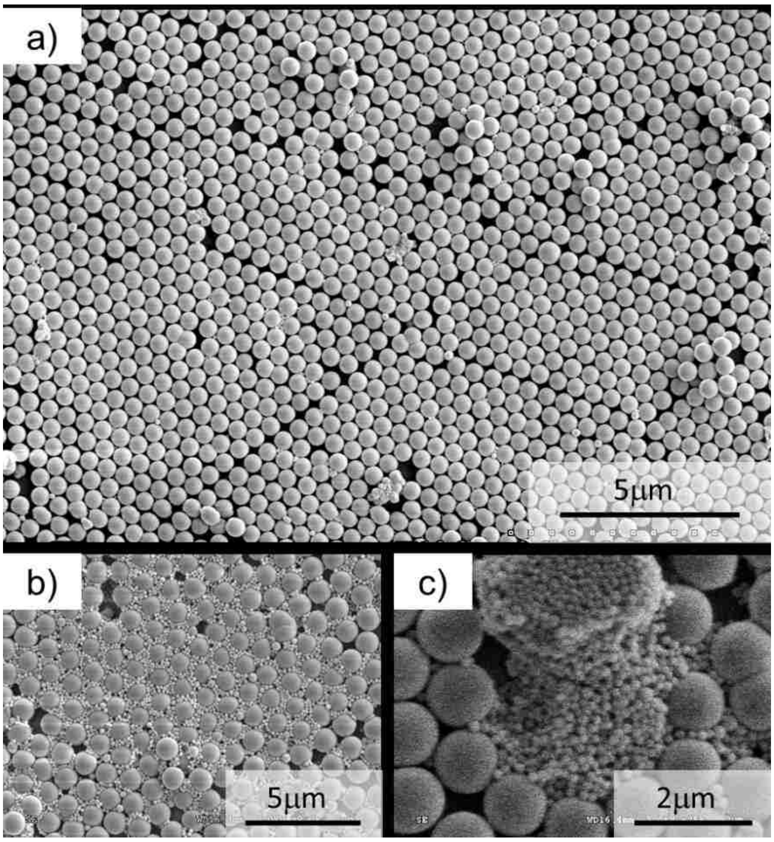

Figure 6.11 Scanning electron microscope images of bidisperse silica particles assembly a) High quality crystal structure without any nanoparticle. Major fraction of colloidal crystal is observed without nanoparticles, b) small fraction of colloidal crystals where nanoparticles are completely covering micro particles, c) few depositions of nanoparticles, perhaps in drying phase.

6.4. Conclusion

The quantification of microstructure gave valuable insight about the ALB. High quality colloidal assembly can be obtained between (1-3) mm/s coating speed over large substrate area. We were able to show critical trade of in the quality and mass flow rate. This demonstrates time for assembly is crucial. Additionally, using well proportion of bidisperse silica suspension one could improve microstructure to certain extent. How the presence of nanoparticles helps is not well understood. Perhaps nanoparticles help in binding micron size particles together to gain better crystal structure. Although in final structure only fraction of nanoparticles were found, some surrounding micro-spheres and some in form of large deposits.

In future studies effects of interactions can be studied. Different types of particles or solvent will have great impact on formation of crystal on interface. Additionally, substrate properties can affect formation of liquid film.

References

(1) Im, S. H.; Lim, Y. T.; Suh, D. J.; Park, O. O. Three-Dimensional Self-Assembly of Colloids at a Water-Air Interface: A Novel Technique for the Fabrication of Photonic Bandgap Crystals. *Adv. Mater.* **2002**, *14* (19), 1367–1369.

(2) Kumnorkaew, P.; Ee, Y. K.; Tansu, N.; Gilchrist, J. F. Investigation of the Deposition of Microsphere Monolayers for Fabrication of Microlens Arrays. *Langmuir* **2008**, *24* (21), 12150–12157.

(3) Tessier, P. M.; Velev, O. D.; Kalambur, a. T.; Lenhoff, a. M.; Rabolt, J. F.; Kaler, E. W. Structured Metallic Films for Optical and Spectroscopic Applications via Colloidal Crystal Templating. *Adv. Mater.* **2001**, *13* (6), 396–400.

(4) Haes, A. J.; Haynes, C. L.; Van Duyne, R. P. Nanosphere Lithography: Self-Assembled Photonic and Magnetic Materials. *MRS Proc.* **2000**, *636*, 1–6.

(5) Vlasov, Y. a; Bo, X. Z.; Sturm, J. C.; Norris, D. J. On-Chip Natural Assembly of Silicon Photonic Bandgap Crystals. *Nature* **2001**, *414* (6861), 289–293.

(6) Johnson, N. P.; Jin, C.; Li, Z. Y.; McLachlan, M. A.; McComb, D. W.; De La Rue, R. M. Optical Properties of Tetragonal Photonic Crystal Synthesized via Template-Assisted Self-Assembly. *J. Appl. Phys.* **2006**, *99* (11).

(7) Harris, D. J.; Hu, H.; Conrad, J. C.; Lewis, J. a. Patterning Colloidal Films via Evaporative Lithography. *Phys. Rev. Lett.* **2007**, *98* (14), 1–4.

(8) Haynes, C. L.; McFarland, A. D.; Zhao, L.; Van Duyne, R. P.; Schatz, G. C.; Gunnarsson, L.; Prikulis, J.; Kasemo, B.; Käll, M. Nanoparticle Optics: The Importance of Radiative Dipole Coupling in Two-Dimensional Nanoparticle Arrays †. *J. Phys. Chem. B* **2003**, *107* (30), 7337–7342.

(9) Biancaniello, P. L.; Crocker, J. C. Line Optical Tweezers Instrument for Measuring Nanoscale Interactions and Kinetics. *Rev. Sci. Instrum.* **2006**, *77* (11), 1–10.

(10) Hayward, R. C.; Saville, D. a; Aksay, I. a. Electrophoretic Assembly of Colloidal Crystals with Optically Tunable Micropatterns. *Nature* **2000**, *404* (6773), 56–59.

(11) Koyama, K.; Yamaguchi, N.; Miyasaka, T. Antibody-Mediated Bacteriorhodopsin Orientation for Molecular Device Architectures. *Science (New York, N.Y.)*, 1994, *265*, 762–765.

(12) Velev, O. D.; Kaler, E. W. In Situ Assembly of Colloidal Particles into Miniaturized Biosensors. *Langmuir* **1999**, *15* (11), 3693–3698.

(13) Yi, D. K.; Kim, M. J.; Turner, L.; Breuer, K. S.; Kim, D. Y. Colloid Lithography-Induced Polydimethylsiloxane Microstructures and Their Application to Cell Patterning. *Biotechnol. Lett.* **2006**, *28* (3), 169–173.

(14) Guldin, S.; Hüttner, S.; Kolle, M.; Welland, M. E.; Müller-Buschbaum, P.; Friend, R. H.; Steiner, U.; Tétreault, N. Dye-Sensitized Solar Cell Based on a Three-Dimensional Photonic Crystal. *Nano Lett.* **2010**, *10* (7), 2303–2309.

(15) Weldon, A. L.; Kumnorkaew, P.; Wang, B.; Cheng, X.; Gilchrist, J. F. Fabrication of Macroporous Polymeric Membranes through Binary Convective Deposition. *ACS Appl. Mater. Interfaces* **2012**, *4* (9), 4532–4540.

(16) Boudreau, L. C.; Kuck, J. a.; Tsapatsis, M. Deposition of Oriented Zeolite A Films: In Situ and Secondary Growth. *Journal of Membrane Science*, 1999, *152*, 41–59.

(17) Bohaty, A. K.; Abelow, A. E.; Zharov, I. Nanoporous Silica Colloidal Membranes Suspended in Glass. *J. Porous Mater.* **2010**, *18* (3), 297–304.

(18) Yuan, Z.; Burckel, D. B.; Atanassov, P.; Fan, H. Convective Self-Assembly to Deposit Supported Ultra-Thin Mesoporous Silica Films. *J. Mater. Chem.* **2006**, *16* (48), 4637.

(19) Velev, O. D.; Lenhoff, A. M. Colloidal Crystals as Templates for Porous Materials T T. *Synthesis (Stuttg).* **2000**, *5*, 56–63.

(20) Wang, B.; L. Weldon, A.; Kumnorkaew, P.; Xu, B.; Gilchrist, J. F.; Cheng, X.

Effect of Surface Nanotopography on Immunoaffinity Cell Capture in Microfluidic Devices. *Langmuir* **2011**, *27* (17), 11229–11237.

(21) Wang, D. Y.; Mohwald, H. Rapid Fabrication of Binary Colloidal Crystals by Stepwise Spin-Coating. *Adv. Mater.* **2004**, *16* (3), 244–247.

(22) Toolan, D. T. W.; Fujii, S.; Ebbens, S. J.; Nakamura, Y.; Howse, J. R. On the Mechanisms of Colloidal Self-Assembly during Spin-Coating. *Soft Matter* **2014**, *10* (44), 8804–8812.

(23) Ye, R.; Ye, Y. H.; Zhou, Z.; Xu, H. Gravity-Assisted Convective Assembly of Centimeter-Sized Uniform Two-Dimensional Colloidal Crystals. *Langmuir* **2013**, *29* (6), 1796–1801.

(24) Denkov, N.; Velev, O.; Kralchevski, P.; Ivanov, I.; Yoshimura, H.; Nagayama, K. Mechanism of Formation of Two-Dimensional Crystals from Latex Particles on Substrates. *Langmuir* **1992**, *8* (12), 3183–3190.

(25) Dimitrov, A. S.; Nagayama, K. Continuous Convective Assembling of Fine Particles into Two-Dimensional Arrays on Solid Surfaces. *Langmuir* **1996**, *12* (5), 1303–1311.

(26) Dimitrov, A. S.; Nagayama, K. Steady-State Unidirectional Convective Assembling of Fine Particles into Two-Dimensional Arrays. *Chem. Phys. Lett.* **1995**, *243* (5–6), 462–468.

(27) Kumar, V.; Bahadur, N.; Sachdev, D.; Gupta, S.; Reddy, G. B.; Pasricha, R. Restructural Confirmation and Photocatalytic Applications of Graphene Oxide-Gold Composites Synthesized by Langmuir-Blodgett Method. *Carbon N. Y.* **2014**, *80* (1), 290–304.

(28) Zheng, Q.; Zhang, B.; Lin, X.; Shen, X.; Yousefi, N.; Huang, Z.-D.; Li, Z.; Kim, J.-K. Highly Transparent and Conducting Ultralarge Graphene Oxide/single-Walled Carbon Nanotube Hybrid Films Produced by Langmuir–Blodgett Assembly. *J. Mater. Chem.* **2012**, 25072–25082.

(29) Juan Schneider. Method and Apparatus for Thin Film/layer Fabrication and

Deposition, 2010.

(30) Davies, G. B.; Krüger, T.; Coveney, P. V.; Harting, J. Detachment Energies of Spheroidal Particles from Fluid-Fluid Interfaces. *J. Chem. Phys.* **2014**, *141* (15), 1–9.

(31) Moncho-Jordá, A.; Martínez-López, F.; Hidalgo-Alvarez, R. The Effect of the Salt Concentration and Counterion Valence on the Aggregation of Latex Particles at the Air/water Interface. *J. Colloid Interface Sci.* **2002**, *249* (2), 405–411.

(32) Kozina, A.; Ramos, S.; Díaz-Leyva, P.; Castillo, R. C. Out-of-Equilibrium Assembly of Colloidal Particles at Air/Water Interface Tuned by Their Chemical Modification. **2016**.

(33) Kaz, D. M.; McGorty, R.; Mani, M.; Brenner, M. P.; Manoharan, V. N. Physical Ageing of the Contact Line on Colloidal Particles at Liquid Interfaces. *Nat. Mater.* **2011**, *11* (2), 138–142.

(34) Booth, S. G.; Dryfe, R. A. W. Assembly of Nanoscale Objects at the Liquid/Liquid Interface. *J. Phys. Chem. C* **2015**, *119* (41), 23295–23309.

(35) Bardosova, M.; Dillon, F. C.; Pemble, M. E.; Povey, I. M.; Tredgold, R. H. Langmuir-Blodgett Assembly of Colloidal Photonic Crystals Using Silica Particles Prepared without the Use of Surfactant Molecules. *J. Colloid Interface Sci.* **2009**, *333* (2), 816–819.

(36) Mayer, H. C.; Krechetnikov, R. Landau-Levich Flow Visualization: Revealing the Flow Topology Responsible for the Film Thickening Phenomena. *Phys. Fluids* **2012**, *24* (5), 1–33.

(37) Brewer, D. D.; Allen, J.; Miller, M. R.; Santos, J. M. De; Kumar, S.; Norris, D. J.; Tsapatsis, M.; Scriven, L. E. Mechanistic Principles of Colloidal Crystal Growth by Evaporation-Induced Convective Steering. *Langmuir* **2008**, *24* (23), 13683–13693.

(38) Diao, J. J.; Hutchison, J. B.; Luo, G.; Reeves, M. E. Theoretical Analysis of

Vertical Colloidal Deposition. *J. Chem. Phys.* **2005**, *122* (18), 184710.

(39) Li, X.; Gilchrist, J. F. Large-Area Nanoparticle Films by Continuous Automated Langmuir-Blodgett Assembly and Deposition. *Langmuir* **2016**, *32* (5), 1220–1226.

(40) Bardosova, M.; Pemble, M. E.; Povey, I. M.; Tredgold, R. H. The Langmuir-Blodgett Approach to Making Colloidal Photonic Crystals from Silica Spheres (Advanced Materials (2010) 22 (3104) DOI:10.1002/adma.200903708). *Adv. Mater.* **2010**, *22* (45), 5081.

(41) Crystals, C. Two-Dimensional Interfacial Colloidal Crystals. *Phys. Rev. Lett.* **1980**, *45* (7).

(42) Kralchevsky, P. A.; Danov, K. D. Interactions between Particles at a Fluid Interface. *Nanosci. Colloid. Interfacial Asp.* **2010**, 397–435.

(43) Szekeres, M.; Kamalin, O.; Grobet, P. G.; Schoonheydt, R. A.; Wostyn, K.; Clays, K.; Persoons, A.; Dekany, I. Two-Dimensional Ordering of Stober Silica Particles at the Air/water Interface. *Colloids Surfaces A Physicochem. Eng. Asp.* **2003**, *227* (1–3), 77–83.

(44) Joshi, K.; Muangnapoh, T.; Stever, M. D.; Gilchrist, J. F. Effect of Ionic Strength and Surface Charge on Convective Deposition. *Langmuir* **2015**, *31* (45), 12348–12353.

(45) Werner Stöber, A. F. Controlled Groth of Monodisperse Silica Spheres in the Micron Size Range. *J. Colloid Interface Sci.* **1968**, *26* (1), 62–69.

(46) Benard Binks, T. H. *Collidal Particles at Liquid Interfaces.pdf*; Cambridge University Press, 2006.

(47) Safouane, M.; Langevin, D.; Binks, B. P. Effect of Particle Hydrophobicity on the Properties of Silica Particle Layers at the Air-Water Interface. *Langmuir* **2007**, *23* (23), 11546–11553.

(48) Detrich, Adam; Deak Andras; Erzsebet, Hild; Kovacs, A. L.; Horvolgyi, Z.

Langmuir and Langmuir-Blodgett Films of Bidisperse Silica Nanoparticles. *Langmuir* **2010**, *26* (4), 2694–2699.

(49) Mcgorty, R.; Fung, J.; Kaz, D.; Manoharan, V. N. Colloidal Self-Assembly at an Interface. *Mater. Today* **2010**, *13* (6), 34–42.

(50) Kondo, M.; Shinozaki, K.; Bergstrom, L.; Mizutani, N. Preparation of Colloidal Monolayers of Alkoxylated Silica Particles at the Air-Liquid Interface. *Langmuir* **1995**, *11* (2), 394–397.

(51) Ren, J.; Song, S.; Lopez-Valdivieso, a.; Shen, J.; Lu, S. Dispersion of Silica Fines in Water-Ethanol Suspensions. *J. Colloid Interface Sci.* **2001**, *238* (2), 279–284.

(52) Kumnorkaew, P.; Weldon, A. L.; Gilchrist, J. F. Matching Constituent Fluxes for Convective Deposition of Binary Suspensions. *Langmuir* **2010**, *26* (4), 2401–2405.

(53) Kumnorkaew, P.; Gilchrist, J. F. Effect of Nanoparticle Concentration on the Convective Deposition of Binary Suspensions. *Langmuir* **2009**, *25* (11), 6070–6075.

Symbols

U_W	Web Velocity (mm/s)
V	Flow rate of suspension (ml/min)
a	Particle radius (μm)
ρ	Particle coverage
W	Web width (mm)
ϕ_μ	Volume fraction of microspheres
ϕ_ν	Volume fraction of microspheres
ε	Fraction of particle deposition
M	Particle mass flow rate (mg/min)
ρ_p	Particle density (mg/ml)
Ψ_6	Local bond order
r	Ratio of nanoparticles to micron particles
ΔG_d	Detachment free energy of particle at air water interface
γ_{aw}	surface tension of air-water interface

CHAPTER 7

Summary and future directions

7.1. Work summary

Convective particle assembly is a useful method for producing crystalline networks of colloidal particles. This process is very intuitive and working with a stable suspension does not require a great deal of understanding. Although a better understanding of process parameters is required in a general case. This study mainly provides a consistent and extensive representation of "Nagayama" equation. Which was a mere mass balance description of the process.

The phase transition is a unique property of an evaporation driven colloidal assembly. This helps us in the isolation of the system into two parts, which would help in defining the physics more effectively. The time scale is a key to make the necessary assumptions. Using the Darcy flow model we were able to formulate an analytical flow behavior in the colloidal porous network. This provided an analytical expression for the parameter ℓ, which was not well posed. The description of ℓ is well validated with the experiments. We were able to improve the scaling of coating thickness vs. substrate velocity. We showed that $h \equiv 1/u^2$ which was traditionally believed to be $h \equiv 1/u$. Also, this study helps in understanding a degree of submonolayer as a function of substrate velocity, which would be important in designing perforated networks of colloidal assembly. Similar length scale shows up in nanoparticle films. Since the nanoparticle assembly is weak under evaporation stresses, it breaks into the cracks. We showed that this well-known phenomenon can be effectively used in a case of convective deposition to fabricate uniform linear cracks. The crack spacing obtained using the convective deposition can be tuned to operating conditions. This opens up a new avenue for fabricating lithography level structures at much cheaper cost.

We also studied the effect of marangoni flow in the colloidal film. A typical case of an excess surfactant or a binary mixture of solvent gives rise to the marangoni flow. Marangoni flow direction plays a crucial part in flow behavior. We showed that using a proper concentration of SDS surfactant one can broaden the monolayer velocity range to a great extent. This makes process flexible if the desired outcome is a monolayer.

Interactions of colloidal particles is an ignored topic in the convective assembly. This research talks about how the particle interactions with the substrate as well as interface play a crucial role in governing a microstructure of the assembly. Before selecting the set of particles, substrate, and solvent understanding of the stability criteria is essential. The interaction effect is a non-trivial one and unique for a different set of parameters, but we made an attempt to describe one of the paths to follow. This study also reflects on many suspension rheology areas where the particle volume fraction is made higher using an excessive salt.

Instability-driven streak formation in microsphere suspension depositions has plagued the field of rapid convective deposition since its inception. While significant process enhancements have been made to suppress these defects, there is very little convention understanding as to how and why streaks occur. This work demonstrates that streak formation cannot be ignored easily, but can be isolated using surface treatment. Using hydrophobic patches on a substrate allows isolation of streaks to a particular area, leaving the in-between area with the high-quality crystal structure. This technique reflects on one of the major issues regarding the large scale coating. Knowing the undesired area prior to coating increase an efficiency of the process.

This study also enlightens the relatively new technique of continuous colloidal assembly via. Automated Langmuir-Blodgett method. We demonstrated the limitation of microstructure one could obtain with ALB. Knowledge about a trade-off between speed and quality is essential to start large area coatings. A small improvement in the microstructure is possible using the binary suspension with a proper ratio.

8.2. Future directions

In every physical process, as you dig dipper into it, you discover new questions. Similarly, this research displays more fundamental questions. Today we have powerful image processing software's as well as sensors to produce require data. Following ideas are scrambled with the progress of thesis, but they guide well-defined direction for future work.

Convective deposition is still further from the reach of producing monolayers of nanoparticles (d< 200nm). One of the main reasons is the stability of solvent onto a substrate. Also, how the nanoparticles behave in thin films. This research works well for weakly Brownian particles (d >500nm), but as you decrease the particle size diffusion is a dominant phenomenon. Even though convective deposition occurs in low substrate limits (10-100 μm/s), the Peclet number is sufficiently higher in the case of weakly Brownian particles, which makes it much easier. For nanoparticles, one has to consider a noise term. Today a good amount of theory is available in a case of noise in a droplet, which needs to be reorganized for smaller particle case. Also, surfactant and proper choice of the solvent-substrate pair would help in stabilizing the thin film. This improvement will take a convective deposition as a potential method for producing quantum dots and molecular membranes.

Additionally, the convective deposition is considered to be an irreversible process, i.e. the crystal formation is a one-way stream. Recent research of imposing a vibration on this process has opened up a new area for research. Sufficient energy input can make crystal structure formation a dynamic process. There is time scale in which the structure is reversible. These colloidal particles respond to stress and form interesting structures, such as square packing. Rigorous model for understanding particles behavior in oscillating shear will improve the convective deposition technique to a new level. Today’s microscopes are capable of operating at such high frame rates to capture the particle motion in the vibrating field.

Also, the convective deposition has been tested only on hard solid substrates, it would be great to try out the convective assembly onto a porous or an elastic substrate. Additionally, convective deposition is tested only with spherical particles. Using cylindrical particles would be challenging, especially for an evaporation driven process. Also, nowadays Janus particles are made using the convective deposition method, but no one has studied the assembly of Janus particles via convective deposition.

Crack formation in nano films is definitely an alternative for designing a simple microfabrication devices. Developing a method to smoothly connect cracks of different spacing as well as making a closed networks of cracks which could be used in micro reactors. Also, cracks have potential in many semiconductor devices, where two length scales are required. In situ observation of this process would give a better understanding of crack initialization and propagation.

ALB process, on the other hand, needs more engineering approach. This field of producing continuous particle assembly is still in very early stage. There is a lot that needs to be done to increase the efficiency of the process. Playing with basic parameters such as the type of particle and solvent would not be the bad start. The process of rolling the substrate needs to be improved for efficiently carrying the particle assembly on the interface. Computer simulations of the flow inside the trough would be helpful to design a more effective geometry for the trough.

APPENDIX A

Confocal imaging and details of image analysis

Quick introduction of confocal

I have used a Visitech confocal attached to the Olympus microscope. Most of the imaging has been done using a 100x magnification objective. It is an oil lens. We have installed a 480nm bluish green laser with a 510filter. Rhodamine B is one of the ideal flurochromes. It excites around 500nm and emission is around 625, which is much higher, and emits out from a 520nm filter. Thus imaging with filter-on allows to capture the emission florescence from the dye, while blocking the lesser light source.

Particle imaging

The florescent particles were synthesized using the insertion of dye (Rhodamine B). The particle synthesis is done using a Strober method in two steps. The core is synthesized using a dye insertion and then a shell is built. This process keeps the surface properties intact. Also dye does not leak in solvent during deposition too. In a case of imaging the non-florescent particles, the sample is rewetted using an 8mM solution of Rhodamine B in DMSO. The refractive index of DMSO is ideal for imaging on an oil lens. Most of the experiments were done on a silica substrate and using the silica particles. This allows very high imaging quality, due to refraction index matching of lens, substrate, particles, and DMSO.

Rewetting of sample does not alter the microstructure for silica particles. Silica-silica bond is very strong. Solvent flows through porous structure. This provides bright background for imaging (A.1a). In the case of florescent particles the particles are bright and background is black (A.1c). For polystyrene particles, on the other hand, the bond with substrate is little weaker. Thus for analyzing polystyrene particles we heat coatings to 60^{o}C for 2 mins. This allows enough adhesion that avoids peeling of particles from the substrate without disturbing any particle arrangement.

Image analysis

Crystal properties can be quantified using different parameters, e.g. Voronoi area, g(r), Ψ_6. Since we are working with monolayers or RHCP multilayers, Ψ_6 is suitable. It's a number and can provide enough information about (hexagonal) crystal structure. We also calculate ρ, which represents particle coverage. Together they (Ψ_6 and ρ) provide great amount of information about the quality and coverage of coating.

The image analysis is done using the IDL software. The scanned images are obtained as a Tiff stack. For any sample, the scanning is done using taking images by moving sample with the help of linear motor. The frame rate of imaging and the speed of linear motor is well adjusted to avoid any overlap in images and get more area covered. Each sample was scanned at 3-4 different locations for determining the morphology. Around 10^6 particles are scanned for each sample.

Following procedure is done on all images to obtain the results. First after reading an image it was converted to 8 bit with and black background and white particles. Then the noise is subtracted to make all the features smooth. Particles were discriminated by background and noise by size and brightness. And finally the coordinates of all points were analyzed. The locations of all particles allow calculation of Ψ_6 and ρ.

ρ is particle coverage defined as fraction of the area covered by particles. The maximum value of ρ can be 0.9012.

$$\rho = \sum_{i=1}^{N} \frac{\pi a_i^{\,2}}{A} \tag{1}$$

Here N is the total number of particles, and A is the coating area.

Ψ_6 is also called local bond order, it is defined as follows (Fig. A.2).

$$\Psi_6(i) = \frac{1}{N}\sum_{j=1}^{N}\left(\exp 6i\theta(rij)\right) \tag{2}$$

$\Psi_6\,(i)$ is local bond order of i^{th} particle. Here, N is number of nearest neighbor with respect to particle (*i*). A nearest neighbor of reference particle is defined as a particle in the vicinity of diameter distance. θ is the angle between reference particle and corresponding nearest neighbor (*j*). For a perfect hexagonal crystal the Ψ_6 is equal to 1. Due to defects and a small polydispersity Ψ_6 decreases.

The good crystalline sample can have disconnected coating and thus lower ρ. On the other hand almost fully particle covered coating (high ρ) could be less crystalline. Thus we need both parameters to define morphology of crystal structure (Fig. A.3).

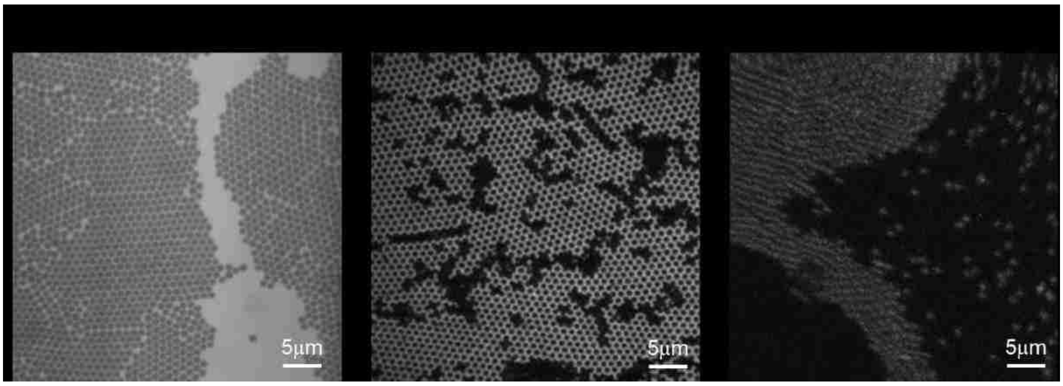

Figure A.1 confocal image taken for 1μm silica microspheres. a) The bright background is due to rewetting sample using DMSO and Rhodamine B. b) the background is dark but 1 μm particles are surrounded by 100nm fluorescent silica spheres, which give bright features, c) image of florescent silica particles obtained without rewetting of a sample. The background is black.

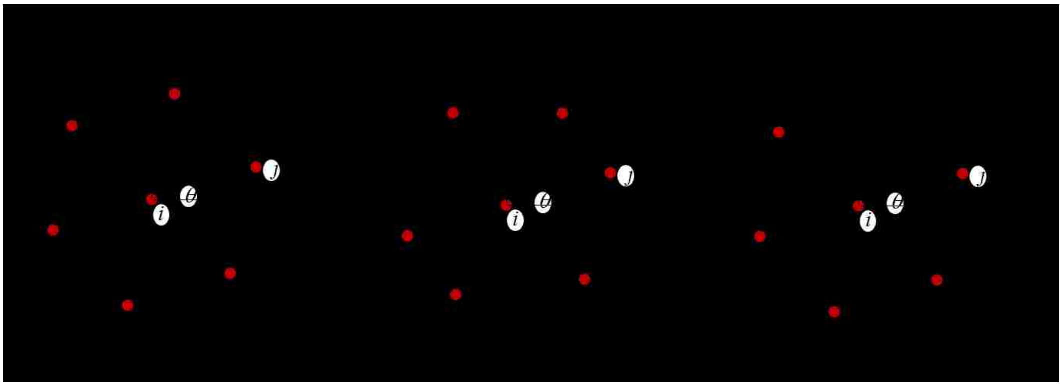

Figure A.2 illustrates calculation of Ψ_6. a) Perfect crystal with 6 nearest neighbors, =1, b) particle with 6 nearest neighbors, but $\Psi_6<1$. c) Particle with missing 6 nearest neighbors, $\Psi_6<1$.

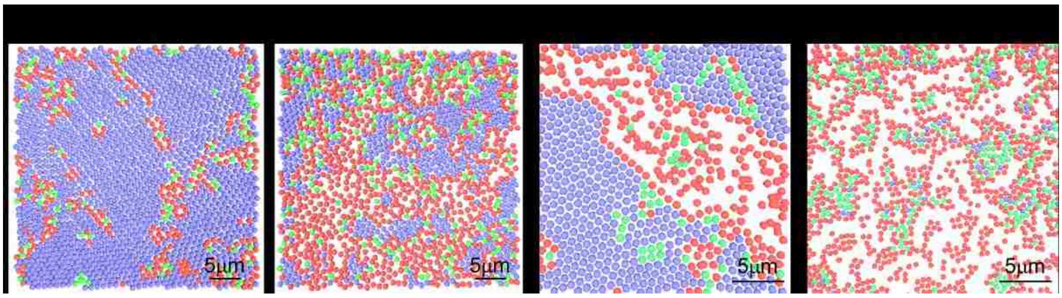

Figure A.3 a) High ρ, and high Ψ_6, b) High ρ, and low Ψ_6, c) low ρ, and high Ψ_6, d) low ρ, and low Ψ_6.

APPENDIX B

Details of convective deposition apparatus

Experimental box

Convective deposition is the evaporative driven assembly, which requires constant temperature and humidity conditions. A small change in outside conditions can affect the final structure significantly. This is why the experimental box (Fig. B.1a) is maintained at a constant relative humidity and temperature. A humidity is controlled by balancing the dry air flow and stream output from humidifier. Humidifier is connected to a flow control value (Willhi Co. Ltd), which triggers with humidity meter. The humidity is maintained at 20% for most of experiments or as specified. The overall temperature is controlled around 72^{o}F. For some specific experiments the stage temperature is controlled using the temperature controller. The dimension of box is large to avoid any strong air currents, which might enhance the evaporation flux.

Experimental setup

The experimental setup consists of a linear motor (Harvard Instruments Co. Ltd.), which is connected to a stage. The blade is placed with a certain angle to the substrate. For most of the experiments the blade angle is maintained at 45^{o}. In chapter 3, the blade angle is changed as specified. The blade is connected to the steel plate, which is bend in required angle to give the stability. Also, the blade is clamped tightly to a lab jack, which allows vertical motion of blade, however, damps other vibrations. The bottom of blade is taped by paraffin, which makes it hydrophobic. The lab jacks are fixed to bottom table by screws and weight to avoid any vibrations. (Fig. B.1b) The cleaned substrate is fixed to a stage using a piece of scotch tape prior to any experiment so that the substrate is not misplaced. This ensures smooth and linear motion of the substrate. The substrate cleaning and other treatments are mentioned in specific chapters. To avoid any scratches and spoiling, substrates handled using soft tweezers with a great care. The cleaned substrates are always stored in DI water and only removed just prior to experiment. Also, the substrate are freshly prepared and used within couple of days to avoid growth of algae or any other contamination.

Particles used

Over a period I have used Silica and Polystyrene particles with a variety of sizes (d).

- Raw particles: 1000nm SiO2, 500nm SiO_2.
- Prepared particles: 1000nm-100nm-80nm Florescent SiO_2. Prepared using Stöber[1] process, with the addition of Rhodamine B dye. The 1000nm particles are produced using a core and shell method, which maintains the surface properties. 1000nm florescent particles have been used to validate some analysis by doing in situ experiments with a confocal microscopy. 100nm florescent particles have been used in ALB microstructure improvement. Whereas 80nm SiO_2 particles were used in cracking analysis.
- Purchased suspension: 1000nm PS, 500nm PS, and 100nm PS.

Suspension preparation

For purchased as well as raw particles, the suspension is made from scratch. The purchased particles usually contains an excess of stabilizing agent, which affect the coating. The cleaning of SiO_2 particle is done by washing three times with ethanol, this process reduces the polydispersity by removing the smaller particles. This is followed by 3-5 times water cleaning to make sure all the ethanol has been removed. The cleaning a done using a high speed centrifuge (Thermo scientific). The speed and time is calculated from sedimentation velocity. For purchased product the polydispersity is high, thus only water washing is done to take out excess stabilizer. The suspension is diluted to ideal volume fraction and stored in small centrifuge tubes. Fresh suspension is used for every experiment. Suspension is tip sonicated (Fisher Scientific, sonic dismembrator) 10s prior to every experiment to maintain the consistency.

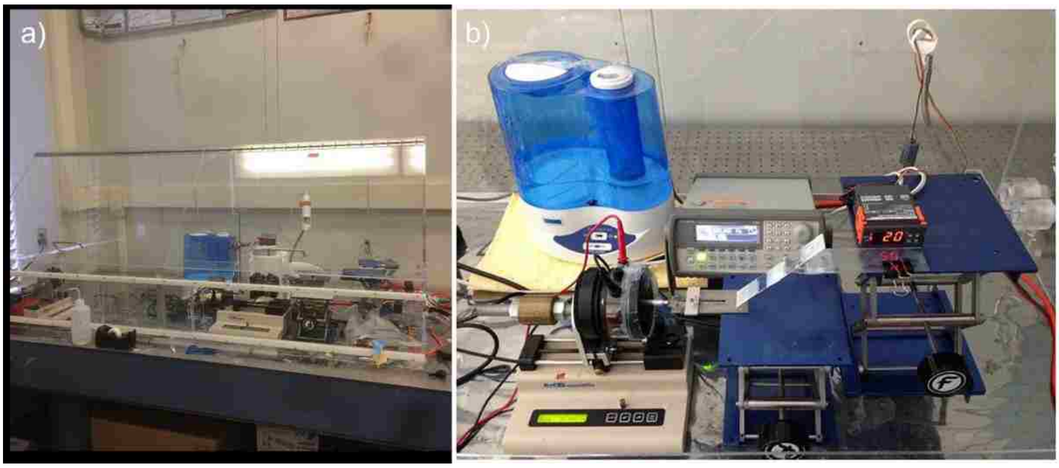

Figure B.1 a) humidity controlled box with volume ~ 500lr. b) Experimental setup consists of linear motor attached to a stage. Lubricant is spread on a lab jack to provide smooth motion of substrate. Lab jacks are fixed on table to avoid vibration.

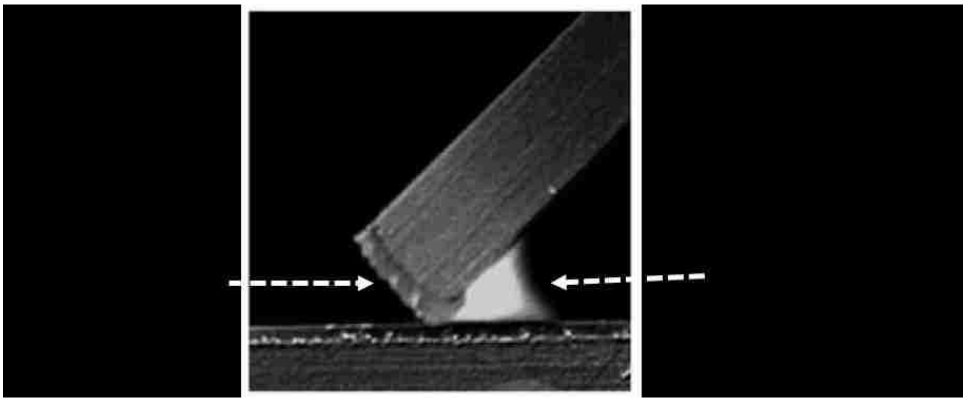

Figure B.2 hydrophobic blade treatment helps confining meniscus in its shape, without leaking from the bottom.

APPENDIX C

Crystal transition and flow in thin film

C.1. Summary

Crystal formation mechanism is quite unexplored area in evaporation driven assembly. Convective deposition is different from traditional dip coating[1–4] or Landau Levich[5–7] type coating methods. The main difference is in the time scale for evaporation and thin film equilibrium, which allows better crystallinity. The crystal formation in the convective deposition is generally an irreversible process. Capillary bonds between bigger colloidal particles (d >500nm) are much stronger that the flow drag. Thus a tiny polydispersity in particles results in smaller grain size. External energy in the form of mechanical vibration has shown some positive improvements[8] for making the process dynamic and increasing the grain size. The impact of vibration is sensitive to a particular range of amplitudes and frequency. However, why vibration works is still a mystery.

C.2. Landau-Levich vs convective deposition

Dip coating is a very established method for the coating of thin films of different solvents, where a thin film is formed by slowly removing the substrate from the bath of liquid or suspension. Landau-Levich gave the first mathematical relationship for coating thickness as a function of Ca and l_c. The capillary number (Ca) is the balance between the viscous drag and surface tension, which is defined as $Ca=\mu U/\gamma$. Capillary length on the other hand, is a balance between surface tension and gravity, which is defined as $q^{-1}= l_c = (\gamma/\rho g)^{1/2}$. The relationship is valid for small Reynold's number flow. The equilibrium height of film is given by Eq. (1)

$$h_\infty = 0.945\, l_c Ca^{2/3} \quad (1)$$

Here, 'h_∞' is the equilibrium film thickness, 'l_c' is the capillary length, and 'Ca' is the capillary number. In the above equation, the static meniscus at the substrate and liquid interface is a balanced between the surface tension and gravity. On the other hand, the dynamic meniscus is a balance between the Laplace pressure and viscous forces. Assuming the lubrication approximation, we can obtain Eq. 1. Deryagin and Titievskaya[5] gave the first direct experimental evidence for the utility of the Landau-Levich equation. The convective deposition shares a similar geometry as that of dip coating, with the primary difference being that flow is driven in the opposite direction due to fluid evaporation (Fig. C.1). There is a competition between the thin film approaching equilibrium and the thin film evaporation. When a substrate velocity is larger, of the order of mm/s, the liquid film approaches equilibrium faster, which is followed by a solvent evaporation. Thus particles follow flow steam-lines and get deposited quite randomly in evaporation step. On the other hand in case of a slower substrate velocities (1-300 μm/s), the evaporation is fast enough to increase local particle volume fraction. Particles get deposited before the liquid film approaches equilibrium. This results in the phase separation and formation of the high-quality colloidal crystals. Maël Le Berre et. al. gave an experimental validation of this transition between a mode of coatings. They showed for a particular liquid, the coating thickness is determined by the evaporation rate for lower substrate velocities and by the viscous drag (Eq. 1) at a higher substrate velocities. Thus the coating thickness first decreases (Nagayama Eq.) and then increases (Landau-Levich Eq.) as a function of substrate velocity[6]. The transition velocity depends on the evaporation rate. Fig. C.2 shows a difference between the particle structures obtained by a convective deposition and a dip coating. Fig. C.2 (a-c) is a typical high-order crystal structure obtained by the convective deposition. Particle assembly is tuned with the evaporation. Fig. C.2 (d-f) typical settling of particles in the faster Landau-Levich mode of deposition, however the evaporation process is disconnected from the convection, and assembly occurs from a flux in the vertical direction.

Typically in a case of evaporation-driven flows, variation in the thin film thickness allows particles volume fraction gradient. This helps in the formation of high-order crystal structures. If a substrate velocity is higher, evaporative driven convection is not enough to tolerate such volume fraction gradient within the thin film. The time scale for assembly and time scale for flow compete with each other to produce one particular type of the coating structure.

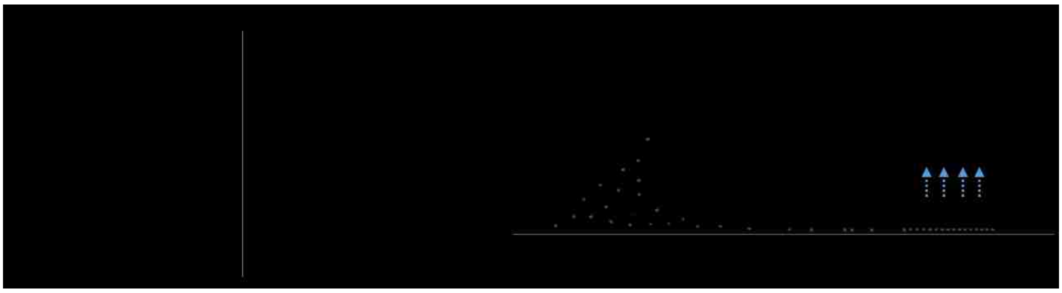

Figure C.1 a) the schematic showing dip coating where the substrate is withdrawn from the bulk, the substrate velocity is of the order of 0.5-10 mm/s b) Experimental setup for convective deposition, where a meniscus is pulled relative to the substrate to induce deposition and the local ordering of particles. Relative substrate velocity is on the order of 1-300 μm/s.

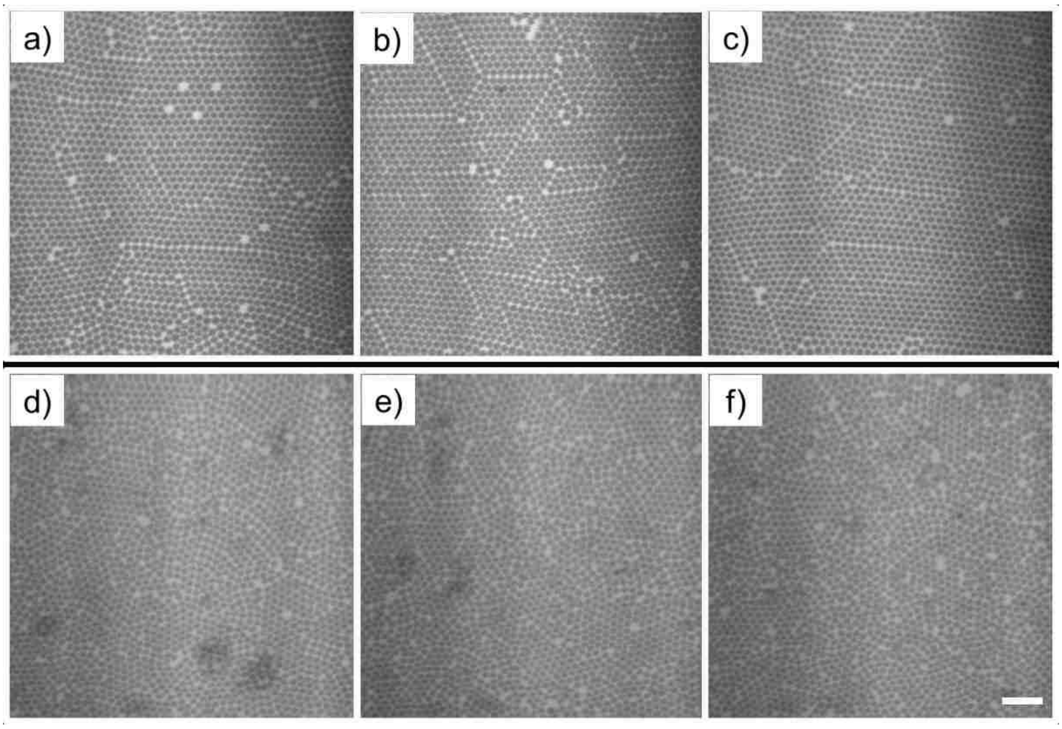

Figure C.2 a)-c) conventional high-order crystal structure obtained via evaporation driven convective assembly. d)-f) less crystal structure in case of Landau-Levich type deposition, substrate velocities are of the order of mm/s. Scale bar represents 5μm in all figures.

2.3. Flow regimes of convective assembly

It is evident from above that convective deposition indeed is different from Landau-Levich thin film profile. For a better understanding of thin film profile, one can separate the different flow regimes. This approach has been used previously[9,10]. Fig.C.3 illustrates different flow regions, which could be studied separately. In Regime I, particles follow streamlines, the small vector represents the streamline direction and magnitude of the velocity. The streamlines are illustrated from the previous studies[5] considering recirculation in bulk meniscus. Regime II, particles get dragged by convective steering[11,12] in a case of multilayer depositions and by capillary forces in a case of monolayer depositions. Volume fraction changes from ϕ_0 to ϕ_m in a small distance. Where ϕ_0 is the suspension volume fraction and ϕ_m is the final volume fraction of the closed pack structure. For *RHCP* packing, ϕ_m ~0.74. Regime III, a close-packed structure of particles, the solvent flows through this porous medium and eventually evaporates (chapters 2).

Some important dimensionless numbers are given in footnotes[ab].

---

[a] Reynolds Number (Re) = $\rho u_s d/\eta$. Peclet number (Pe) = du_s/D. Stokes number (St) = $(\rho_p d/\rho l)$*Re. Froude Number (Fr) = $u_s/(gd)^{0.5}$. Capillary number (Ca) = $u_s\mu/\gamma$ Sedimentation number (N_G) = $d^2\Delta\rho g/\mu u_s$.

[b] For 1μm particle usual range for these numbers is, Re: $(10^{-5}$-$10^{-4})$, Pe: (10-100), Ca: $(10^{-7}$-$10^{-6})$. Fr: $(\sim 10^{-9})$, N_G: (1-10).

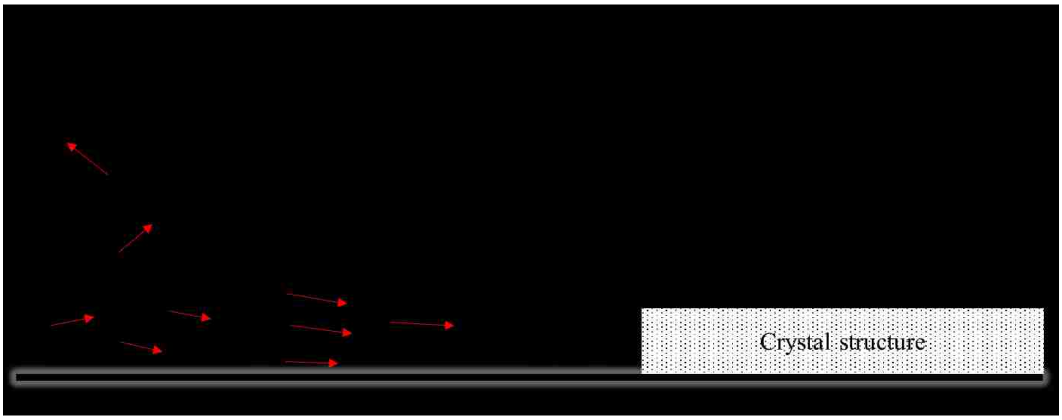

Figure C.3 Flow regimes in the thin film progression via convective assembly. I) particles follow the streamlines. The suspension behaves as a single phase. II) Particles get dragged by convective steering and capillary forces, the volume fraction changes from ϕ_0 to ϕ_m. III) A close-packed structure of particles, which translate with a substrate velocity. The solvent penetrates through and eventually evaporates.

C.3.1. Regime I

The flow visualization can be done using lubrication theory (Fig. C.4).

$$\frac{\partial p}{\partial x} = \mu \frac{\partial^2 u}{\partial z^2} \tag{2}$$

When $\gamma(\sigma)=$ constant, $\frac{\partial u}{\partial z} = 0$ at $(z=h)$ and $u = u_s$ at $(z=0)$.

This gives,

$$u = u_s + \frac{1}{\mu}\frac{\partial p}{\partial x}\left(\frac{z^2}{2} - zh\right) \tag{3}$$

We can write the average velocity as.

$$\bar{u} = u_s - \frac{h^2}{3\mu}\frac{\partial p}{\partial x} \tag{4}$$

In the case of thin film flows gravity is negligible and thus pressure can be expressed in terms of curvature pressure. $p = \gamma\left(\partial^3 h / \partial x^3\right) + \rho g h + \Pi$

Laplace pressure + gravity + Π (disjoining pressure + osmotic pressure).

The gravity term can be neglected in the dynamic meniscus. As we decrease the film thickness or particle size, Π term starts contributing significantly. But for the following studies, Laplace pressure is the only dominant term.

For the dynamic film, we can write the following.

$$\dot{h} = -\partial_x\left(h.\bar{u}\right) \tag{5}$$

Putting values of p_x in above equation, we get,

$$\dot{h} = h_x\left(u_s\right) - \frac{\gamma}{3\mu}\left(3h^2 h_x h_{xxx} + h^3 h_{xxxx}\right) \tag{6}$$

This type of equation can be solved using the perturbation analysis. Without the presence of substrate velocity an exact answer can be obtained[13] by the change of variables, $h(x, t)=t^{-\alpha}h(\eta)$ and $\eta=xt^{-\alpha}$. In the following studies, we do not consider the presence of noise. Most of the following studies have been performed on a weakly Brownian particles, but as at very low thin film thickness, the noise contribution cannot be neglected. The spreading of nano-drops is profoundly affected by the presence of noise[14]. Usually, for the particle size less than 200 nm, the thermal fluctuations are quite dominant. In such a case one needs to use Langevin Equations of motion[15]. $u_t = \frac{\gamma u}{m} + \frac{\xi(t)}{m}$. Here γ is the friction coefficient and ξ is the stochastic noise.

The Eq. (6) becomes highly nonlinear in the presence of surface tension gradient. Researchers have attempted introducing different ways of surface tension gradient in above equation[5,16–18]. Like the conductive, concentration, or temperature induced surface tension gradient. In a case of surface tension gradient, the boundary conditions are as follows.

At z=h, $\mu(\partial u / \partial z) = (\partial \gamma / \partial x)$, and at z=0, $u = u_s$.

$$u = u_s + \frac{1}{\mu} p_x \left(\frac{z^2}{2} - zh \right) + \frac{1}{\mu} z \gamma_x \tag{7}$$

$$\bar{u} = u_s - \frac{h^2}{3\mu}(p_x) + \frac{h}{2\mu}(\gamma_x) \tag{8}$$

$p_x = \gamma h_{xxx} + \gamma_x h_{xx}$

The sign of $(\partial \gamma / \partial x)$ determines the flow behavior. The positive gradient amplifies the velocity and agitates the flow. On the other hand, negative gradient counters the substrate velocity and calms the flow.

The eq. (6) modifies as follows.

$$\dot{h} = -\nabla \left[u_s h - \frac{h^3 h_{xxx}}{3\mu} \gamma + \frac{h^2}{2\mu} \gamma_x - \frac{h^3 h_{xx}}{3\mu} \gamma_x \right] \tag{9}$$

In chapter 3, we have considered the case of both positive and negative surface energy gradient. In Eq. 6 and 9 the flow due to pinning of contact line is not considered, which indeed the dominant flow in a convective deposition. Thus the streamlines in the flow 'regime I' are different from what one would expect from just Navier Stokes equation. But this approach helps in predicting the broader picture in a case of marangoni flow.

Even though we cannot solve equation 9 accurately, we can extract the flow behavior in an extreme cases of surface energy gradient.

Dimensional analysis

The equilibrium coating thickness defined by the Eq. 6 and 9 is much smaller (defined by Eq. 1) than the final coating thickness. This flow behavior is terminated because the thin film profile is governed by a completely different set of equations after particle phase separation. Thus foe dimensional analysis we will consider coating thickness '*H*' (N*d) instead of the equilibrium thickness predicted by Eq. 1.

Let's define following dimensionless parameters.

$$\bar{h} = {h}/{H}\,,\ \bar{x} = {x}/{L}\,,\ \bar{\gamma} = {\gamma}/{\gamma_o}\,, \bar{t} = {t}/{T}$$

L is the characteristic length scale in accordance with a flattening of the bulk meniscus. Which could be defined as L~$l_c Ca^{1/3}$. γ_o Is the surface tension of pure solvent. Equation 9 becomes.

$$\frac{L\bar{h}_{\bar{t}}}{Tu_s} = -\bar{\nabla}\left[\bar{h} - \left(\frac{H^4}{L^3}\right)\frac{\bar{h}^3\bar{h}_{\bar{x}\bar{x}\bar{x}}}{3Ca}\bar{\gamma} + \left(\frac{H^2}{L}\right)\frac{\bar{h}^2}{2Ca}\bar{\gamma}_{\bar{x}} - \left(\frac{H^4}{L^3}\right)\frac{\bar{h}_{\bar{x}\bar{x}}}{3Ca}\bar{\gamma}_{\bar{x}}\right] \tag{10}$$

H/L << 1. Thus we can neglect the higher order terms of H. The equation then simplifies to.

$$\frac{L\bar{h}_{\bar{t}}}{Tu_s} = -\bar{\nabla}\left[\bar{h} + \left(\frac{H^2}{L}\right)\frac{\bar{h}^2}{2Ca}\bar{\gamma}_{\bar{x}}\right] \tag{11}$$

This equation is easy to visualize. When the marangoni flow is dominant, the term with γ_x contributes more. Positive γ_x leads to flow in the direction of substrate velocity, and negative γ_x calms the flow. Also, the film thickness increases in the case of negative γ_x, which increase the recirculation. This has been reported previously[19,20]. A common approach to solving Eq.uation 9 has been replacing γ_x by surfactant concentration Γ_x or by marangoni number (Ma)[18,19,21,22]. We will not explicitly solve Eq. (9), but this helps visualizing results in chapter 3.

C.3.2. Regime II

In this regime, the particle volume fraction changes. Evaporation in the thin film results in a formation of a stable crystal structure. In the convective assembly, these three regimes attain a pseudo equilibrium state. The point where a stable crystal structure exhibits, known as the crystal front. In chapter 2, as discussed how a solvent flows through the crystal structure and eventually evaporates, giving the final desired product, the dry particle assembly. The presence of stable crystal structure and evaporation give rise to capillary force and drag force. The particle concentration near the crystal front is more than that of in the bulk suspension. Thus this region separates a bulk meniscus and final colloidal crystal. The length scale is defined as ℓ_{II}. Variation in concentration causes the osmotic pressure, which counters the force field.

A similar length scale shows up in different problems like the sedimentation[23,24], drying of drops[25,26], particle assembly assisted with an electric field[27] or a magnetic field, etc. Our job here is to get an estimate of this length scale as a function of particle diameter and/or substrate velocity for the case of the convective deposition. Also, to get the estimate for work done by the flow to maintain that concentration gradient. This will help in understanding the mystery behind vibration assisted convective deposition. For many years researchers have used the vibration as a tool for enhancing the crystal assembly[8] or for modifying the orientation of crystal structure[28].

Model development

Fig. C.5 illustrates the increase in volume fraction in regime II. On the left, suspension exhibiting single phase flow profile as discussed in regime I, with the volume fraction ϕ_0. And consider an average entering velocity in regime II be u_0. On the right, particles are part of the stable crystal structure with the volume fraction $\phi_m \sim 0.74$, and particle velocity is equivalent to the substrate velocity u_s. $U(x)$, $u(x)$ are the average particle and solvent velocities in the thin film. We can adopt 1-D colloidal transport model.

In steady state

$$\frac{\partial(\phi U)}{\partial x} = 0 \tag{12}$$

From the boundary condition at the crystal front, $\phi * U = \phi_0 * u_0$ = constant.

The particle velocity is balanced by an external force field and osmotic pressure.

$$U = u + \frac{k(\phi)}{6\pi\mu a}\left(F - \nabla\hat{\mu}\right) \tag{13}$$

Here, $k(\phi)$ is the mobility, a is the particle radius, F is a force field, μ is viscosity, and $\hat{\mu}$ is chemical potential. For colloidal particles $\nabla\hat{\mu} \approx \nabla\phi$.

Here there are several forces (F) involved.

Drag force $F = 6\pi\mu a U$

Gravitational force $F = V_p \Delta\rho g$, V_P is the particle volume ($4/3\pi a^3$).

Electric force $F \approx \varepsilon\varepsilon_0 \zeta E a$, E is the constant electric field, ζ is the zeta potential.

Capillary force $F \approx \gamma a^2 K_1(q)$, q is the inverse of capillary length, and K_1 is modified Bessel function of the first kind.

Gravitational force shows up in a sedimentation problem[24], while the electric force in electro-kinetic particle assembly. Ferrar et al. showed a dynamic crystallization in steady electric field[27], crystal structure exists as long as an electric field is present. Velev et al. showed an electric field assisted convective deposition could improve the crystal grain size by oscillating the thin film length[29]. In convective deposition geometry, only drag and capillary forces are important. Several research groups have attempted to model this regime of convective deposition[9,10]. Born et al.[10] used a subtle approach to approximate the film thickness as a quadratic function, which fixes the velocity of the particle. One can thus calculate the work done on a particle by drag force. Also, they correlated the solvent flux due to evaporation with the temperature and humidity using first order scaling of the Clausius−Clapeyron relation. Using this they arrived at the work done by the flow on the particle is as follows.

$h = a'(T) + b'x + c'x^2$. Thus $U = \left(a(T) + bx + cx^2\right)^{-1}$.

a(T) comes from Clausius−Clapeyron relation. The work done on particle is,

$$\frac{\Phi}{KT} = \frac{\int U.dx}{D} = \tilde{P}e \qquad (14)$$

Φ is the work done on particles, D is kinematic diffusivity, and $\tilde{P}e$ is the characteristic Péclet number. The model predicts for $\tilde{P}e > 1.5$, one should observe a hexagonal crystal structure, i.e. If work done (Φ) is more than the particle's thermal agitation, particles will form the closed pack hexagonal crystal. The $\tilde{P}e$ can be controlled by temperature (T), which controls the velocity at x=0, a(T). This is given by Clausius-Clapeyron equation a(T) ~ exp(-k/T). But they have experimentally observed the hexagonal crystal structure even for lower values of $\widetilde{Pe}$, which must be a result of the capillary forces. For a multilayers formation the system can be best represented by the convective steering[11,12], but the capillary force plays an important role in the formation of monolayer assembly. In both monolayer and multilayer, the change is volume fraction occurs almost as a shock[10]. In the case of the monolayer, this transition is sharper due to the capillary forces. This result of sharp increase in volume fraction is important for the justification of assumption in Chapter 2. A force field can be related to a gradient of the volume fraction (ϕ) (Eq. 13). The typical length scale ℓ_{II} of regime II is ~ 10-20μm, which varies with substrate velocity as well as particle diameter.

For the particle flow, the chemical potential in Eq. (13) can be replaced by osmosis. This allows writing the chemical potential in terms of particle volume fraction. Also, the diffusivity and mobility are a strong function of particle volume fraction. The mobility goes down as the volume fraction reaches to a maximum volume fraction. We can write an effective diffusivity as follows[18,24,26],

$$D = D_0 k(\phi) \frac{\partial(\phi z(\phi))}{\partial \phi} \frac{\partial \phi}{\partial x} \tag{15}$$

Where[30] $K(\phi)=(1-\phi)^{6.55}$, $z(\phi)=1.85/(0.74-\phi)$ for large ϕ. And $D_0=KT/6\Pi\eta a$.

We generally work with the high Péclet number flow conditions, which results in the irreversible formation of hexagonal packing. Joy et al. showed[28] that, using a mechanical vibration, the effective temperature of particles can be increased. This allows them to rearrange. Rearrangement gives both the better crystal structure as well as square packing. Square packing could be the result of micro-rheology, which provokes rearrangement of particles to minimize a shear stress. Muangnapoh et al[8] showed a better crystal structure can be obtained for the monolayer in a particular range of amplitudes (10-100 μm) and frequencies (20-50 Hz). This range gives an idea about the length scale (A) and the time scale ($1/\omega$) in regime II. In the case of bidisperse silica particle suspension, aiming for the monolayer, the vibration helps only in particular combinations of amplitude and frequencies. The mechanism behind the vibration assisted coating is unknown. This analysis might provide some insights on this topic. Understanding the relationship between vibration parameters and ℓ_{II} gives a new degree of freedom to this process. In a shorter time scale, the crystal formation can be made a dynamic process. Muangnopoh[31] plotted the map of different coating morphologies observed in the case of bidisperse silica (1μm) and Ps (100nm) suspension as a function of amplitude and frequencies (Fig C.6). According to this set of experiments, we observed three different morphologies, viz. a) an enhanced monolayer, where monolayer quality is improved over controlled coatings (Fig. C.7a). b) A pseudo phase consists of a combination of the sub-mono-multi layer due to the overlap of coatings (Fig. C.7 b) and c) the phase separation, which consists of different deposits of microspheres and nanospheres (Fig. C.7c). It is clear that enhancement in monolayer quality is only achieved in a certain range of amplitude and frequency. Over amplitude (higher A) can dump one layer on top of the other, which results in mixed morphologies. Additionally, smaller amplitudes with high frequency can tear apart the thin film. Closer microspheres become the part of growing crystal due to high capillary forces, while the nanoparticles oscillate back and forth. This results in flushing of nanoparticles beyond critical local volume fraction. We think this happens decrease in particle mobility with increasing nanoparticles.

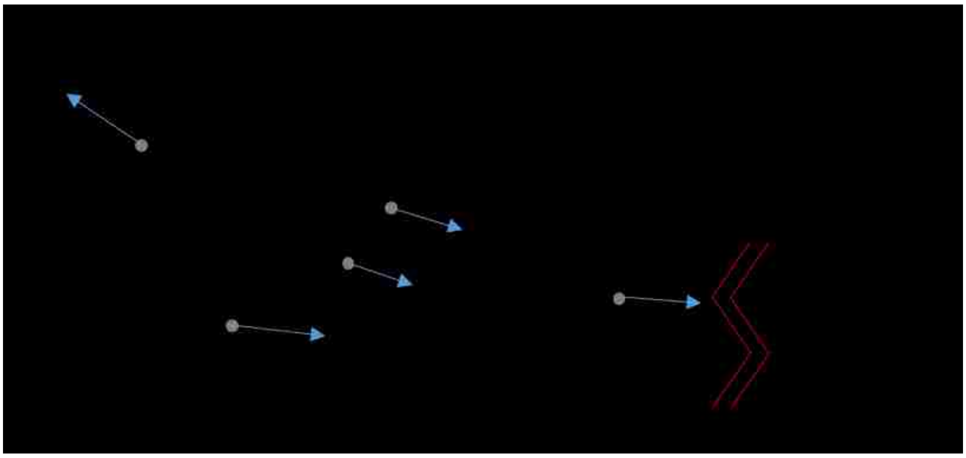

Figure C.4 thin film developed with a substrate velocity. Before crystal front/phase separation the flow behavior is governed by lubrication forces. $\gamma(\sigma)$ is surface tension as a function of surface (σ). Particle flows as a tracer in liquid. No concentration gradient and external force on particles.

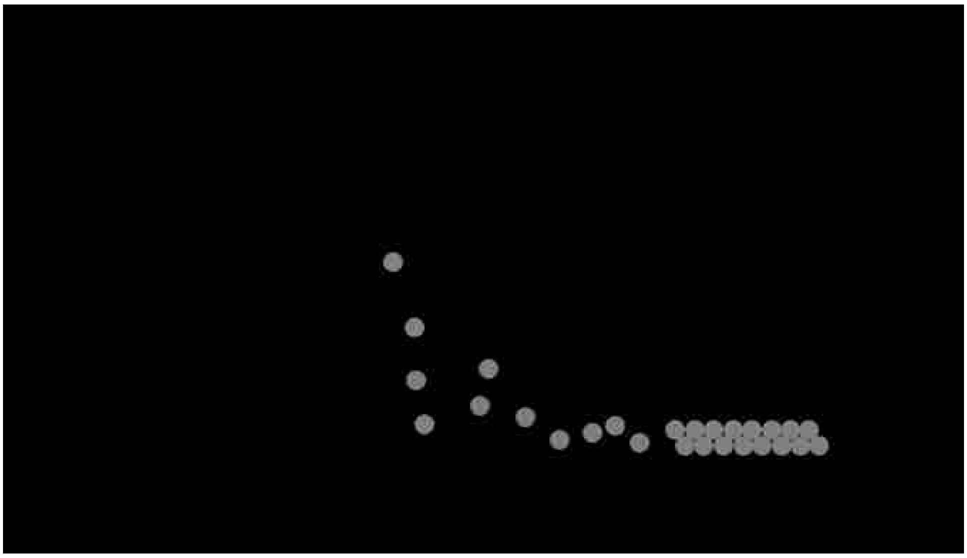

Figure C.5 in the presence of force field, particles maintain volume fraction gradient. Osmotic pressure balances the force. The phase separation occurs over a small length ℓ_{II}. The crystal structure is being formed, because of the evaporation.

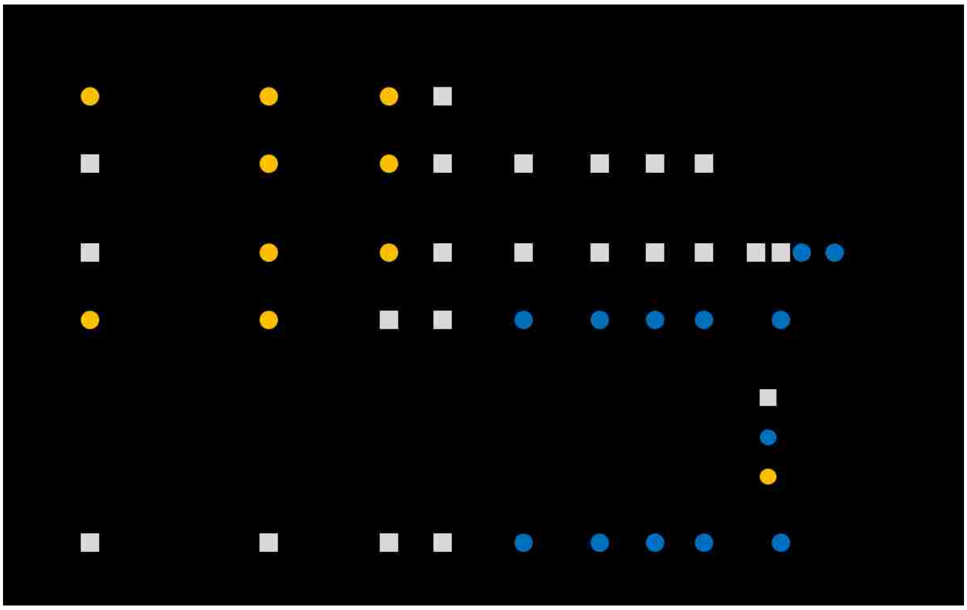

Figure C.6 Overall phase diagram of vibration-assisted deposition, which summarizes the effect of the amplitude (A_0) and the frequency of vibration (ω). Gray squares represent enhanced monolayer range. Blue circles represent pseudo phase, and orange circles represent phase separation. [c]

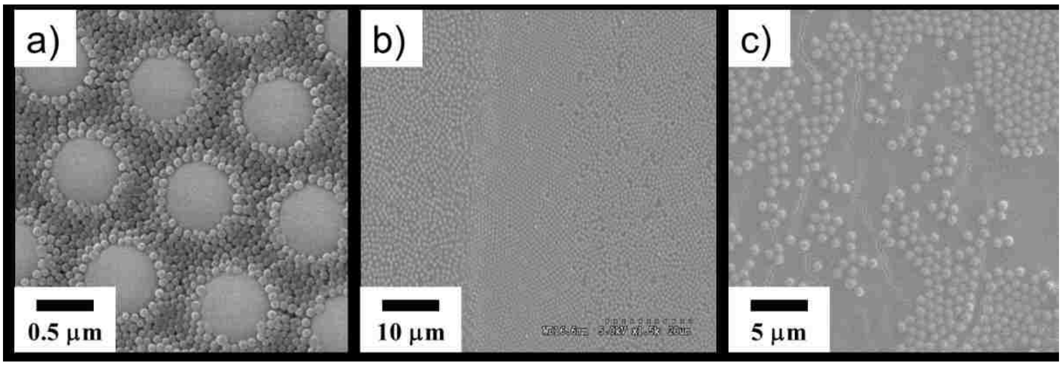

Figure C.7 a) Enhanced monolayer, microspheres are surrounded by nanoparticles particles. b) Pseudo phase at a higher amplitude (A) and lower frequencies (ω), where different morphologies have formed by dumping one layer on top of the other. c) Phase separation at lower A and higher ω, nanoparticles are separately deposited destroying the crystal structure.

---

[c] This data have been adopted from Dr. Muangnapoh thesis. 2015 © Lehigh University.

Conclusions

The convective deposition is fundamentally different from the Landau-Levich type deposition. The fundamental difference in terms of evaporation and substrate motion time scale. The phase separation of particles is a unique feature of convective deposition, which allows separating different flow regime that is governed by separate set of equations (flow conditions). We understood that the transition between any two flow regimes is sharp enough to isolate and study them separately. Research shows that there usually exists three regimes. In the first regime, the flow is similar to the Landau-Levich flow, where particles follow the streamline, and the suspension exhibits single phase behavior. In the second regime, the particles densify in a short length scale. This process is irreversible for the higher Péclet number. Although, mechanical vibration can allow the structure to rearrange and improve. We have discussed different scenarios and tools of solving them. Understanding the length scale of regime II allows the interpretation of previous results obtained with mechanical vibration. In situ experiment using confocal microscopy or particle scattering methods should be the next step to experimentally measure the volume fraction of particles. Also, mechanical vibration can be effectively used for bidisperse silica suspensions with different particle size ratio to obtain various crystal structure and porosity.

References

(1) Boudreau, L. C.; Kuck, J. a.; Tsapatsis, M. Deposition of Oriented Zeolite A Films: In Situ and Secondary Growth. *Journal of Membrane Science*, 1999, *152*, 41–59.

(2) Kumar, V.; Bahadur, N.; Sachdev, D.; Gupta, S.; Reddy, G. B.; Pasricha, R. Restructural Confirmation and Photocatalytic Applications of Graphene Oxide-Gold Composites Synthesized by Langmuir-Blodgett Method. *Carbon N. Y.* **2014**, *80* (1), 290–304.

(3) Ozin, G. a.; Yang, S. M. The Race for the Photonic Chip: Colloidal Crystal Assembly in Silicon Wafers. *Adv. Funtional Mater.* **2001**, *11* (2), 95–104.

(4) Diao, J. J.; Hutchison, J. B.; Luo, G.; Reeves, M. E. Theoretical Analysis of Vertical Colloidal Deposition. *J. Chem. Phys.* **2005**, *122* (18), 184710.

(5) Mayer, H. C.; Krechetnikov, R. Landau-Levich Flow Visualization: Revealing the Flow Topology Responsible for the Film Thickening Phenomena. *Phys. Fluids* **2012**, *24* (5), 1–33.

(6) Le Berre, M.; Chen, Y.; Baigl, D. From Convective Assembly to Landau - Levich Deposition of Multilayered Phospholipid Films of Controlled Thickness. *Langmuir* **2009**, *25* (5), 2554–2557.

(7) Juan Schneider. Method and Apparatus for Thin Film/layer Fabrication and Deposition, 2010.

(8) Muangnapoh, T.; Weldon, A. L.; Gilchrist, J. F. Enhanced Colloidal Monolayer Assembly via Vibration-Assisted Convective Deposition. *Appl. Phys. Lett.* **2013**, *103* (18).

(9) Fleck, N. A.; McMeeking, R. M.; Kraus, T. Convective Assembly of a Particle Monolayer. *Langmuir* **2015**, *31* (51), 13655–13663.

(10) Born, P.; Munoz, A.; Cavelius, C.; Kraus, T. Crystallization Mechanisms in Convective Particle Assembly. *Langmuir* **2012**, *28* (22), 8300–8308.

(11) Gasperino, D.; Meng, L.; Norris, D. J.; Derby, J. J. The Role of Fluid Flow and Convective Steering during the Assembly of Colloidal Crystals. *J. Cryst. Growth* **2008**, *310* (1), 131–139.

(12) Brewer, D. D.; Allen, J.; Miller, M. R.; Santos, J. M. De; Kumar, S.; Norris, D. J.; Tsapatsis, M.; Scriven, L. E. Mechanistic Principles of Colloidal Crystal Growth by Evaporation-Induced Convective Steering. *Langmuir* **2008**, *24* (23), 13683–13693.

(13) Bertozzi, a L.; Pugh, M. The Lubrication Approximation for Thin Viscous Films : *Thin Film.* **1994**, No. April, 1–35.

(14) Davidovitch, B.; Moro, E.; Stone, H. a. Spreading of Viscous Fluid Drops on a Solid Substrate Assisted by Thermal Fluctuations. *Phys. Rev. Lett.* **2005**, *95* (24), 8–11.

(15) Lemons, D. S.; Gythiel, A. Paul Langevin ' S 1908 Paper "' On the Theory of Brownian Motion '" & On the Theory of Brownian Motion, A Note from M . P . Langevin, Presented by M . Mascart . *Am. J. Phys.* **1997**, *65* (11), 1079–1081.

(16) Hu, H.; Larson, R. G. Analysis of the Effects of Marangoni Stresses on the Microflow in an Evaporating Sessile Droplet. *Langmuir* **2005**, *21* (9), 3972–3980.

(17) Ristenpart, W. D.; Kim, P. G.; Domingues, C.; Wan, J.; Stone, H. a. Influence of Substrate Conductivity on Circulation Reversal in Evaporating Drops. *Phys. Rev. Lett.* **2007**, *99* (23), 1–4.

(18) Yiantsios, S. G.; Higgins, B. G. Marangoni Flows during Drying of Colloidal Films. *Phys. Fluids* **2006**, *18* (8).

(19) Hu, H.; Larson, R. G. Marangoni Effect Reverses Coffee-Ring Depositions. *J. Phys. Chem. B* **2006**, *110* (14), 7090–7094.

(20) Danov, K. D.; Danov, K. D. Effect of Surfactants on Drop Stability and Thin Film Drainage. *Fluid Mech. Surfactant Polym. Solut.* **2004**, No. 463, 1–38.

(21) Yuan, Z.; Burckel, D. B.; Atanassov, P.; Fan, H. Convective Self-Assembly to Deposit Supported Ultra-Thin Mesoporous Silica Films. *J. Mater. Chem.* **2006**, *16* (48), 4637.

(22) Majumder, M.; Rendall, C. S.; Eukel, J. A.; Wang, J. Y. L.; Behabtu, N.; Pint, C. L.; Liu, T. Y.; Orbaek, A. W.; Mirri, F.; Nam, J.; et al. Overcoming The "coffee-Stain" effect by Compositional Marangoni-Flow-Assisted Drop-Drying. *J. Phys. Chem. B* **2012**, *116* (22), 6536–6542.

(23) Newman, H. D.; Yethiraj, A. Clusters in Sedimentation Equilibrium for an Experimental Hard-Sphere-plus-Dipolar Brownian Colloidal System. *Sci. Rep.* **2015**, *5* (July), 13572.

(24) Piazza, R. Settled and Unsettled Issues in Particle Settling. *Rep. Prog. Phys. Reports Prog. Phys. Rep. Prog. Phys* **2014**, *77* (77), 56602–56626.

(25) Singh, K. B.; Tirumkudulu, M. S. Cracking in Drying Colloidal Films. *Phys. Rev. Lett.* **2007**, *98* (21), 218302.

(26) Routh, F.; Russel, W. B. Horizontal Drying Fronts during Solvent Evaporation from Latex Films. *Aiche J.* **1998**, *44* (9), 2088–2098.

(27) Ferrar, J. A.; Solomon, M. J. Kinetics of Colloidal Deposition, Assembly, and Crystallization in Steady Electric Fields. *Soft Matter* **2015**, *11* (18), 3599–3611.

(28) Joy, M.; Muangnapoh, T.; Snyder, M. a; Gilchrist, J. F. Flow-Induced Alignment of (100) Fcc Thin Film Colloidal Crystals. *Soft Matter* **2015**, *11* (36), 7092–7100.

(29) Kleinert, J.; Kim, S.; Velev, O. D. Electric-Field-Assisted Convective Assembly of Colloidal Crystal Coatings. *Langmuir* **2010**, *26* (12), 10380–10385.

(30) W. B. Russel, D. A. Saville, W. R. S. *Colloidal Dispersions.pdf*; Cambridge University Press, 1989.

(31) Muangnapoh, T. Convective Assembly of Colloidal Monolayers : Mechanical and Chemical Approaches. **2015**, No. May.

VITA

Kedar Joshi was born in Satara on May 4th, 1991 to Prasad Joshi and Madhura Joshi. Satara is a small town in the Maharashtra state of India. He was raised in a well-educated family, which has been a constant source of motivation throughout his career. Since he was raised as a single child, he had a strong bond with his parents. Because of his father's gifted skills in teaching, he developed a deep interest in mathematics in his early age. While in high school, he pursued his interest in math and won prizes in many competitive exams. He attended science college after finishing his secondary education from 2006-2008. It was where he got exposed and attracted to physics and chemistry. The interest in only core mathematics fades away, as he was witnessing growing technology and science.

In 2008, he started his undergraduate in a prestigious chemical engineering college, "Institute Of Chemical Technology," Mumbai. He won different team as well as individual prizes like 'Acta Chemica,' 'Industry Problem' in various technical events. As his interest in chemical engineering grew up throughout his progress, he decided to pursue a doctorate degree. He worked his way to graduate level studies in the USA. In 2012 he joined "Lehigh University" in Pennsylvania and started working with Prof. James F Gilchrist on nanoparticle assembly. He collaborated with his fellow lab mates Alex Weldon, Tanyakorn Muangnopoh, Tharanga Perera, Midhun Joy, and Naval Singh throughout the following years. He oriented his research considering his passion in both the surface science and fluid mechanics. He worked out the relationship between different types of complex interactions happening during nanoparticle assembly. Additionally, he worked on various flow regimes in a thin film. His research helps in understanding fundamental physics behind the complex particle assembly. Besides his research, Kedar trained three undergrad students and served as a teaching assistant for four semesters. Kedar worked on seven journal articles and gave ten talks in his headway through a doctorate degree.

Outside of his academic life, Kedar nourished his hobbies throughout life. He loves playing different sports. In his childhood, he got particularly interested in cricket. He took a professional level cricket training and played at the district level in his high school. As he went to undergraduate, he started enjoying tennis. Tennis took a big part in keeping him fit and healthy throughout his academic life in Lehigh. Kedar has been a member of Lewis Tennis Center Lehigh since 2012. But, he has an altogether different attachment with a game of chess. He felt in love with 64 squares since his childhood. Kedar represented as the chess captain in his high school and undergraduate school. In Lehigh, he joined Lehigh Valley Chess Club to fulfill his chess hunger. In between studies, playing some online chess games kept him sharp in thinking. Kedar is a member of both the ‘World Chess Federation’ and ‘US Chess Federation.'

Apparently, Kedar likes to keep his balance between studies-sports, work-enjoyment, experiments-friends.

Peer reviewed publications

6. **K. Joshi,** J.F. Gilchrist, “Role of surface energy gradient in capillary forces driven self-assembly of colloidal spheres”, *for submission to JCIS.*
5. **K. Joshi,** Z. Zeng, X. Li, J.F. Gilchrist, “Correlation of particle crystallinity with concentration and deposition speed in ALB deposition”, *for submission to Langmuir*.
4. **K. Joshi,** J.F. Gilchrist, “Estimation of drying length during particle assembly by convective deposition”, **2017** *Journal of Colloid and Interface Science* **2017**, doi: http://dx.doi.org/10.1016/j.jcis.2017.01.083.
3. A. Weldon, **K. Joshi,** A. Routh, J.F. Gilchrist, “Uniform cracks growing by convective assembly of nanoparticles”, *Journal of Colloid and Interface Science* **2017**, 487, 80-87.
2. **K. Joshi,** T. Muangnapoh, M. Stever, J.F. Gilchrist, “Effect of ionic strength and surface charge on convective deposition”, *Langmuir* **2015**, 31, 12348−12353.

1. J. Boettcher, M. Joy, **K. Joshi,** T. Muangnapoh, J.F. Gilchrist, “Spacing of seeded and spontaneous streaks during convective deposition" *Langmuir* **2015**, 31, 10935−10938.

Research conferences oral presentation

9. **K. Joshi,** J. Gilchrist, “Drying, cracking, and marangoni flow in the convective deposition”, *Lehigh chemical department symposium* **2017**.
8. **K. Joshi,** J. Gilchrist, “Surfactant induced marangoni flow in capillary forces driven self-assembly of colloidal spheres”, *90th Colloids Surface Science Symposium* **2016**.
7. Weldon, **K. Joshi,** A. Routh, J. Gilchrist, “Uniform cracks growing by convective assembly of nanoparticles”, *90th Colloids Surface Science Symposium* **2016**.
6. **K. Joshi,** J. Gilchrist “Estimation of the drying length during particle assembly by convective deposition”, *Emulsion Polymer Institute ARM* **2016**.
5. **K. Joshi,** C. Tzou, M. Stever, P. Kumnorkaew, J. Gilchrist “Marangoni flow during convective particle assembly”, *68th Annual Meeting of the APS Division of Fluid Dynamics, Gallery of fluid motion,* **2015**.
4. **K. Joshi,** T. Muangnapoh, M. Stever, J. Gilchrist “Effect of ionic strength and surface charge on capillary-driven colloidal self-assembly and deposition”, *89th Colloids Surface Science Symposium* **2015**.
3. **K. Joshi,** T. Muangnapoh, M. Stever, J. Gilchrist “Effect of ionic strength and surface charge on capillary-driven colloidal self-assembly and deposition”, *13th annual TIGER-HEN-HAWK Rheology Symposium* **2015**.
2. **K. Joshi,** T. Muangnapoh, M. Stever, J. Gilchrist “Effect of ionic strength and surface charge on convective assembly”, *Emulsion Polymer Institute ARM* **2015**.
1. A. Weldon, **K. Joshi,** J. Gilchrist; “Instability driven macroscale defects in evaporation-driven particle assembly” *88th Colloids Surface Science Symposium* **2014**.